Università degli Studi di Padova
Dipartimento di Fisica ed Astronomia "Galileo Galilei"

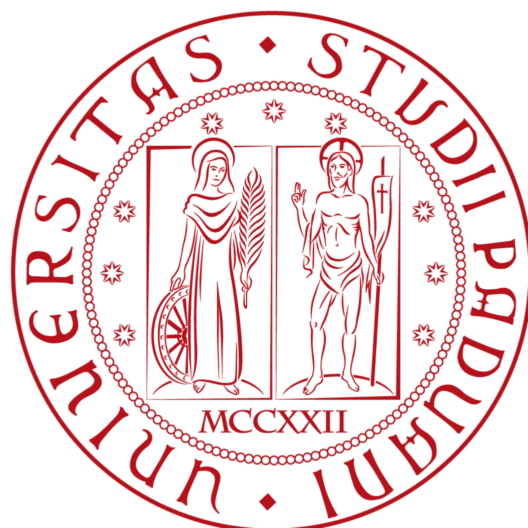

Tesi di laurea magistrale in Fisica

Transient Kelvin-Probe Measurements on Organic Semiconductor Devices

Laureanda: Valeria Milotti

Relatore interno: Prof. Marco Bazzan

Relatore esterno: Privat Dozent Dr. Christian Melzer

Controrelatore: Prof. Enrico Napolitani

Anno Accademico 2016-2017
Sessione di laurea: settembre 2017

Contents

Abstract **v**

1 Introduction **1**

2 Physical Background **3**

2.1 Organic Semiconductors . . . 3
2.1.1 Solid State Structure . . . 3
2.1.2 Energy Levels . . . 7
2.1.3 Transport Properties in Organic Semiconductors . . . 9
2.1.4 Doping in Organic Semiconductors . . . 11
2.1.5 Trapping in Organic Semiconductors . . . 12
2.2 MIS Capacitors and Field-Effect Transistors . . . 13
2.2.1 Metal-Insulator-Semiconductor (MIS) Capacitor . . . 13
2.2.2 Inorganic Field-Effect Transistors . . . 14
2.2.3 Organic Field-Effect Transistors (OFETs) . . . 15
2.3 The Kelvin Probe . . . 17
2.3.1 Kelvin Probe Force Microscopy . . . 20
2.3.2 Applications of KPFM to OFETs . . . 21

3 Experimental Setup **25**

3.1 Layout of the samples . . . 25
3.2 Materials . . . 27
3.2.1 Regioregular Poly(3-hexylthiophene-2,5-diyl) . . . 27
3.2.2 Parylene C . . . 29
3.2.3 Injecting Electrodes . . . 29
3.2.4 Glass and Si/SiO_2 Substrates . . . 30
3.3 Sample preparation . . . 30
3.4 Measuring Setup . . . 33
3.4.1 Kelvin Probe Setup . . . 33
3.4.2 FET probe station . . . 36
3.4.3 Sample Connection . . . 37
3.5 Device Characterization . . . 39
3.5.1 Areal capacitance of the devices . . . 39
3.5.2 Characterisation of the Kelvin probe setup . . . 40

3.5.3 Characterisation of the MIS capacitors 40
3.5.4 Characterisation of the Transistors 42

4 Analysis of Experimental Results 45
4.1 Analysis of MIS capacitors 45
4.1.1 Transit-Time Effects in an Organic Thin Film 47
4.1.2 Theoretical Description of the Charging of a MIS capacitor under a Periodic Bias 50
4.1.3 Harmonic Function 50
4.1.4 Chainsaw Tooth Function 51
4.2 Analysis 52
4.2.1 Fitting the Data 54
4.2.2 Chaisaw fit results 55
4.2.3 Mobility calculation 58
4.3 FET Probe Station Data 64
4.3.1 Extraction of μ from Transistor Transfer Characteristics . . 64
4.4 Comparison Between Ag and Au Electrodes 66
4.5 Summary of Results 68

5 Conclusions 71

A Electronic Processes Involved in Charging and Discharging of a Transistor 73
A.1 Description of a FET with the Telegrapher's equations. 73
A.1.1 Differential equations for OFETs 74
A.2 Response of an OFET to an External Bias 75
A.2.1 Contributions of Doping Charges 77
A.2.2 Response Function of the device 78

B Explicit Calculations of the Surface Potential Response to External Biases 81
B.1 Harmonic bias 81
B.2 Chainsaw Tooth Function, or Triangular Wave 82

Acknowledgements 87

Bibliography 89

Abstract

Il lavoro riportato in questa tesi è stato svolto al Centre for Advanced Materials della Ruprecht-Karls-Universität Heidelberg, sotto la supervisione interna del Prof. Marco Bazzan, e la supervisione esterna del Priv. Doz. Christian Melzer (Ruprecht-Karls-Universitt Heidelberg, Faculty of Physics and Astronomy, Centre for Advanced Materials).

La tesi si è focalizzata sullo studio del trasporto laterale di portatori di carica all'interno dello strato organico di un condensatore MIS (metallo-isolante-semiconduttore) di dimensioni macroscopiche basato sul semiconduttore polimerico poly(3-hexylthiophene) (P3HT).

I campioni sotto analisi sono stati fabbricati dalla candidata su substrati tagliati ad hoc impiegando come tecniche di deposizione lo spin-coating, il CVD e il VTE. Applicando un bias esterno periodico a bassa frequenza ai campioni, è stato possibile monitorare con la sonda Kelvin l'onda di portatori di carica iniettati ed estratti dallo strato organico, esaminando il potenziale del dispositivo a varie distanze dal contatto iniettante le cariche. È stato così possibile osservare che le cariche iniettate penetrano lateralmente nel film organico su distanze dell'ordine dei centimetri.

Partendo dalle misure eseguite con la sonda Kelvin, è stato possibile sviluppare un modello per i MIS, che ha permesso di trovare la funzione di risposta dei dispositivi. Combinando quest'ultima con l'espressione per il bias applicato, è stato creato un modello che descrive la risposta del dispositivo. Il modello è stato poi utilizzato per eseguire il fit dei dati sperimentali, permettendo di trovare una stima per il tempo di volo dei portatori di carica, dalla quale è stato possibile ricavare una stima della mobilità per il trasporto laterale del P3HT in buon accordo con la letteratura. Come prodotto secondario, l'analisi ha anche permesso di fornire una stima della concentrazione di drogante all'interno del semiconduttore organico.

Parallelamente, la stessa procedura di costruzione dei campioni è stata impiegata per creare campioni di OFET, le cui caratteristiche di output e di trasferimento sono state misurate con una apposita stazione di misura. L'analisi del secondo tipo di misure ha permesso di arrivare ad una stima indipendente per la mobilità del P3HT utilizzato per i condensatori MIS, che ha confermato le stime ottenute con l'analisi descritta in precedenza.

Confrontando le stime ottenute con la letteratura e ulteriori stime indipendenti estratte dalle misure eseguite su OFET di riferimento, è stato possibile determinare

che il nuovo metodo sviluppato in questa tesi è un'alternativa affidabile e non invasiva per trovare la mobilità per il trasporto laterale all'interno di un semiconduttore organico con correnti applicate piccole.

Chapter 1

Introduction

Organic semiconductors are a relatively newly studied group of materials that have already found some applications in modern electronics. The development of stable low-cost organic devices remains a challenge, but the rewards that such technology seems to offer are well worth the effort, as is testified by the increasing number of commercialised organic-based products.

The production of electronic devices based on organic compounds offers a number of advantages over traditional inorganic electronics, primarily because of the reduced fabrication costs due to easier processing, and secondly because of the vast realm of opportunities such devices seem to offer.

The field offers prospects such as the possibility to build devices on mechanically bendable substrates, to solve organic semiconductors in an appropriate solution which may then be printed (InkJet technology)[1], or in the biodegradability of some organic devices[2]. Organic devices, moreover, are usually lighter in weight than their inorganic counterparts.

It is possible to modify the chemical structure of organic compounds without drastically changing the characteristics of the embedding devices.

The obstacles that must be overcome when developing organic-based technologies are due to the nature of the compounds. Organic semiconductors undergo degradation under ambient condition, which leads to a life-span of the devices which ranges between a few hours to a couple of years. Moreover, the intrinsic disorder of organic compounds leads to low charge carrier mobilities, and thus to a slow response from the embedding devices. Such devices must be used in applications where a fast response is not necessary, or efforts must be undergone in order to increase it.

The extensive research to which organic semiconductors have been subjected in the past 30 years has led to a much better, even if still incomplete, understanding of the influence of the molecular structure over charge carrier mobility, which in turn has allowed the production of compounds whose carrier mobility rivals with, and sometimes surpasses, that of amorphous silicon.

As a consequence, technological devices based on organic compounds are gaining commercial feasibility every day.

The objective of this work is to determine the properties lateral transport properties for charges inside the organic film due to an external electric field, using as model material the organic semiconductor poly(3-hexylthiophene-2,5-diyl), which is a well known and characterised material in literature. From our measurements we were able to develop a new method to estimate the charge carrier mobility for lateral transport in MIS-capacitors.

Two kinds of devices were constructed, which provided two different methods to determine lateral transport properties and thus the charge carrier mobilities.

The first and more important kind of device consists in metal-insulator-organic semiconductor capacitors, where the charge carrier are injected into the organic semiconducting layer by a metal contact. While these devices are subjected to a periodic voltage bias, which causes charges to be periodically injected and extracted, the surface potential of the organic film is measured using a Kelvin probe, in order to track lateral transport inside the organic layer. This method was developed in order to allow to measure the charge carrier mobility in the *off*-state of the capacitor, by following the potential evolution given by the entering and exiting of charges into and from the organic layer. Thus we show that charges penetrate for centimetres inside the organic layer due to the electric fields that arise and we develop a low-budget method to extract their mobility at very low currents.

The other kind of devices consists in organic thin-layer field-effect transistors, built at the same time as the capacitors, which allow the carrier mobility to be extracted from the I-V transistor characteristics in the linear regime of the *on*-state of the device.

By changing the metal used to build the injecting electrode, we examined also the influence of the contact properties on the response of the device.

Comparing the data with literature and independent estimates extracted from reference OFETS, we found that this method is a reliable alternative to find the mobility inside an organic semiconductor.

Chapter 2

Physical Background

2.1 Organic Semiconductors

Organic compounds are, by definition, molecules that contain carbon atoms in their structure. The term organic semiconductor refers to a class of materials that have the following characteristics:

- their chemical composition is based on carbon and hydrogen, with the occasional presence of other atoms, such as sulfur, oxygen, and nitrogen;
- their electrical properties are those usually shown by an inorganic semiconductor, that are absorption and emission spectra in the visible light range and conductivity intermediate between insulators and metals.

The molecular structure of organic semiconductors can be easily modified by chemical synthesis, enhancing a desired characteristic of the molecules or taking away an undesired one. For example, it is possible to increase the solubility of an organic compound by attaching alkyl side chains to the core molecule.

In analogy with inorganic semiconductors, electronic components based on organic compounds are organic field-effect transistors (OFETs), organic light-emitting diodes (OLEDs) and organic solar cells. Displays based on OLEDS are already widely commercially available, while research is being poured into the improvement of the performance of OFETs, which would be instrumental in the construction of organic electronic devices.

Despite the similarities in behaviour between inorganic and organic semiconductors, these two types of materials are radically different in what pertains the solid state structure, of which an example is the anisotropy in charge transport shown by the latter.

2.1.1 Solid State Structure

Organic compounds are based on carbon, which is a special element because of the unusual abundance of its compounds. This is due to many factors: carbon

is a small atom, which reduces the steric hindrance in its molecules, allowing the creation of many different compounds; its electronegativity allows it to bound with virtually every other element; it belongs to group IV and it can hybridise in many different ways, thus it can form up to four bonds, which leads to chemical versatility and the possibility of creating polymeric chains. Because of these favourable characteristics, organic chemistry comprises a huge number of compounds, both natural and synthesised.

The molecular structures of organic semiconductors has a huge influence on the characteristics of the compound. Based on it, the following three different categories of materials can be identified.

Molecular crystals. Historically, these were the first kind of organic semiconductors to be studied.

Like any crystal, they are constituted by a base which repeats itself on the points of a lattice. Typical bases are made of one or more large, planar, non-polar, electrically neutral molecules, such as polyacenes. Because of this, unlike what happens in inorganic crystals, the bases are bonded to each other not by ionic or covalent bonding, but by the much weaker Van der Waals bonding, which leads to tightly packed structures. Since the onset of Van der Waals forces depends on the polarisability of the molecules involved, melting points of molecular crystals such as polyacenes (fig. 2.1b) rise with their increase in molecular size[3].

Because of their ordered structure, materials belonging to this category detain the highest reported carrier mobility, which make them ideal candidates for the construction of OFETs, even though the preparation and purification steps involved in their production can be difficult[4].

Amorphous molecular films. Amorphous films are based on molecules that do not crystallise into an ordered structure, which can be deposited via spin-coating or evaporation, depending, respectively, on the solubility or the thermal stability of the compound.

Polymer films. A polymer is constituted by a chain of hundreds of covalently bound monomers. These chains aggregate to create a single one-dimensional structure. They are usually processed from solution, which allows to use them in low cost processing such as spin-coating and ink-jet deposition.

Annealing polymers after deposition can allow the creation of pseudo-crystals, that means areas of the film where the polymer molecules are stacked in an ordered fashion. Compounds that self-assemble in this way are called semicrystalline. One such compound is poly(3-hexylthiophene-2,5-diyl), the polymer this work is based on, which will be described in paragraph 3.2.1.

One important characteristic that determines the behaviour of a polymer is *regioregularity*: a polymer is regioregular when the covalent bond between

one monomer with the next is present always between the same two atoms relative to the position of the side chains. The resulting molecule has side chains of adjacent monomers pointing in the alternating direction with respect to the backbone of the molecule, which leads to more ordered morphologies in the semiconducting film with better intrachain ordering and reduced twisting, which in turn lead to improved charge carrier mobilities. For example, measurements of mobility for P3HT executed in organic field-effect transistors (OFETs) were reported to be as high as $\sim 0.01\text{cm}^2\text{V}^{-1}\text{s}^{-1}$ for organic films with high regioregularity and high crystallinity, and $\sim 10^{-4}\text{cm}^2\text{V}^{-1}\text{s}^{-1}$ for organic films with low regioregularity[5].

An organic semiconductor can be tailored relatively easily to the requirements of the desired objective device or of a specific fabrication process. For example, a very common practice is to add or substitute organic side chains to the molecules or polymers in order to increase the solubility of the compound into common organic solvents.

Another kind of modification that can be imposed on an organic molecule is the substitution of one or more carbon atoms with a heteroatom, like sulfur, nitrogen, or oxygen. Such a substitution can change the characteristics of the resulting molecule in favourable ways, which can lead to better light absorption (suited for organic solar cells), light emission (suited for OLEDs), hole transport or electron transport. It is almost impossible, though, to create a molecule with energy levels suited to efficiently express all these characteristics: what is usually done is to create molecules that execute efficiently only one of these tasks. When working with a polymer, the latter two characteristics can be introduced in the same macromolecule by aggregating monomers with different properties.

Processing of Organic Semiconductors

There are many ways to process an organic semiconductor to obtain a semiconducting film. The method must be selected depending on the chemical characteristics of each compound, which may be unusable in some kinds of processing, and on the desired characteristics of the final product. Since not every compound is suited to every method of processing, it is possible to base a classification of organic molecules upon this.

Mostly, the processing methods are divided into two categories.

Wet processing The organic semiconductor is dissolved in a volatile organic solvent, which is supposed to evaporate after or during processing. If the right technique is used, wet processing leads to films that can be extremely thin and that have homogeneous thickness. This kind of processing is very common because it is low budget and easy to achieve, but the resulting films mostly have high anisotropy and are not mechanically relaxed, although it is possible to obtain crystalline films with some techniques. Moreover, the use of a solution may lead to traces of solvent in the final product.

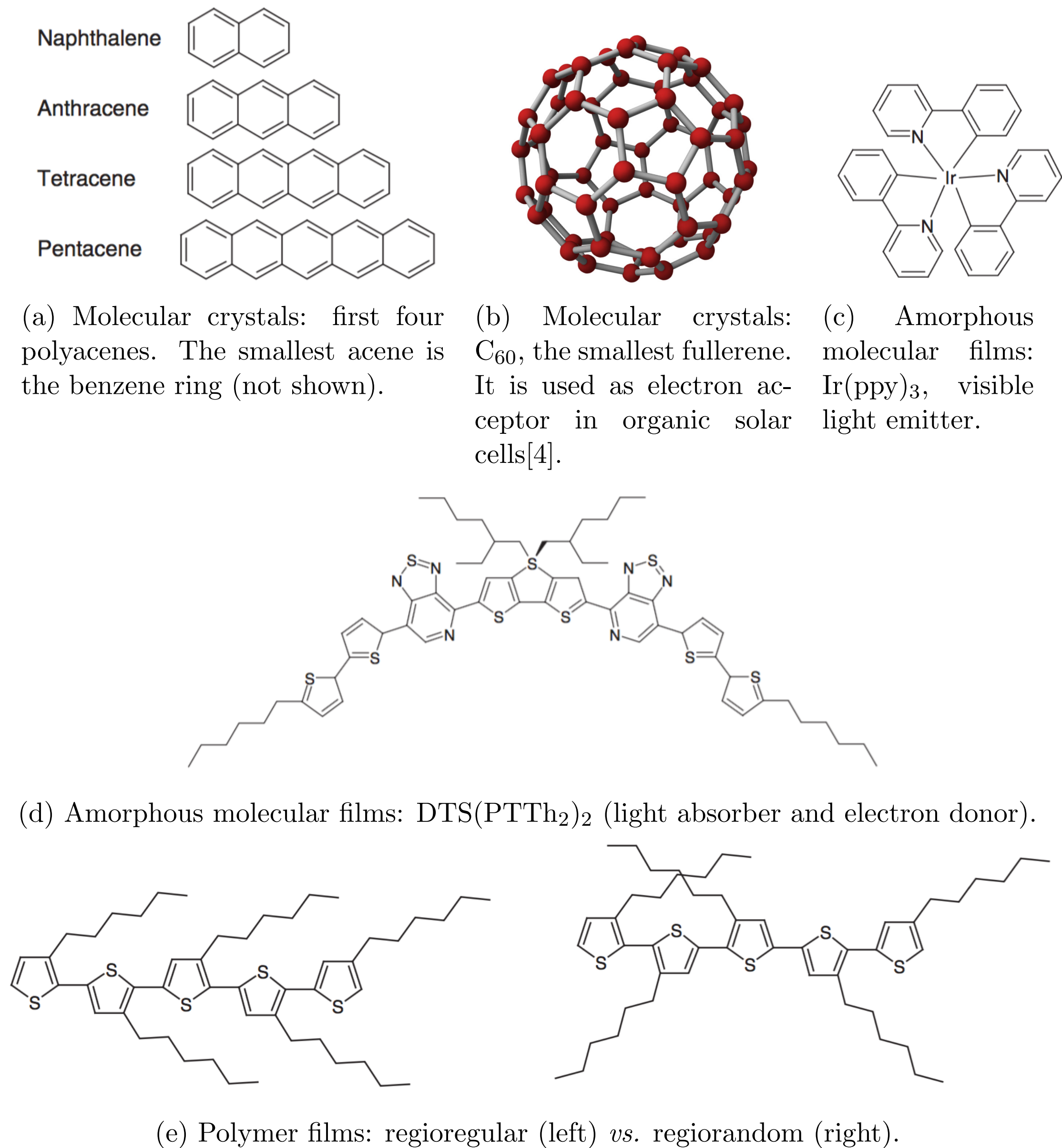

(a) Molecular crystals: first four polyacenes. The smallest acene is the benzene ring (not shown).

(b) Molecular crystals: C_{60}, the smallest fullerene. It is used as electron acceptor in organic solar cells[4].

(c) Amorphous molecular films: $Ir(ppy)_3$, visible light emitter.

(d) Amorphous molecular films: $DTS(PTTh_2)_2$ (light absorber and electron donor).

(e) Polymer films: regioregular (left) *vs.* regiorandom (right).

Figure 2.1: Examples of molecular structures of organic semiconductors.

The compounds that can be processed in this way must be soluble in organic solvents, and thus require side chains to increase solubility. Common wet processing techniques are:

- *spin coating*: a drop of the solution is deposited on the substrate, which is then spinned at thousands of rotations per minute, distributing evenly the solution on the substrate and making the solvent evaporate[6];
- *doctor blading*: a drop of the solution is deposited on the substrate, and

then spread with a blade moving in one direction;

- *drop casting*: a drop of the solution is deposited on the substrate and the solvent is left to evaporate spontaneously;
- *zone casting*: the solution is slowly drizzled onto a moving substrate, so as to allow the solvent to evaporate almost as soon as the solution touches the substrate [7];
- *dip coating*: the substrate is immersed in the solution and then extracted, making the solvent evaporate.

Vapor deposition Vapour deposition is used for relatively small or insoluble molecules. It can't be used for all molecules and it is generally more expensive than wet processing. It allows the creation of thin films with a lower disorder and a high degree of purity, but although it is usually required to create molecular crystals, the results can be amorphous films, too.

- *VTE (vacuum thermal evaporation)*: in a vacuum chamber, kept at low pressure to avoid reaction with air, the material is heated until it evaporates. The vapour condenses as a thin film on any colder surface in line of sight with the melting pot, such as the substrate and the vacuum chamber walls, if the wettability of the surface is right;
- *OVPD (organic vapor phase deposition)*: the organic compound is thermally evaporated inside a stream of hot inert gas, which transports the vapour to the cold substrate surface where it condenses[8];
- *CVD (chemical vapour deposition)*: the process is similar to that for VTE, except that the deposition of the vapour involves a chemical reaction, not thermal condensation.

The processing methods used in this work are spin coating for the deposition of the organic semiconductor, CVD for the encapsulation of the samples in a protective material, and VTE for the deposition of metallic contacts.

2.1.2 Energy Levels

Except the case of molecular crystals, for which the band theory valid for inorganic crystals can be adapted, there is the need to find a theory that models the energy levels inside an organic semiconductor.

In general, the energy of the orbitals for a single molecule can be found using the linear combination of atomic orbitals (LCAO) approximation. When carbon or other molecules from the IV group are involved, full or partial hybridisation of the valence orbitals can happen, which is favoured by the energetic balance in most reactions carbon takes part in. The hybridised 2sp orbitals of two adjacent atoms form σ-bonds, while not-hybridised 2p orbitals form π-bonds, which create,

respectively, σ- and π-orbitals. The spatial probability density of the shared electrons differs in the two cases: while with the σ-bond it is highest between the two atomic nuclei, with a π-bond it distributes above and below the molecular axis [4]. If we add to this representation of the molecule the interaction of the orbitals with the atomic nuclei, we find that this leads to a removal of the energy degeneration of the orbitals, which are splitted in bonding and anti-bonding orbitals. The splitting is severe for σ-orbitals, which separate in a strongly bonding σ- and strongly antibonding $\sigma^\star$-orbitals, which lie at energies, respectively, much lower and much higher than the unsplitted orbitals. Since the interaction of π-bonds with the nuclei is lower than that of σ-bonds, the splitting of the π and $\pi^\star$ orbitals will be much less severe than in the previous case.

Organic semiconductors are π-conjugated molecules, and thus require the carbon atoms to be hybridised in a $2sp_2 2p_z$ configuration.

Observing the resulting energy diagram, one can define the highest occupied molecular orbital (HOMO) and the lowest unoccupied molecular orbital (LUMO). These two energy levels are extremely important in order to understand the characteristics of the compound under study, since they define characteristics such as the absorption and emission wavelength, or the tendency to receive or release a charge carrier. Depending on their readiness to give up or accept an electron, molecules can be referred to as *hole transporting* or *electron transporting* molecules, respectively.

The molecular orbitals are populated with electrons starting from the lowest energy and, if we consider only the valence orbitals, the σ and π orbitals of carbon-based molecules are full, while the $\pi^\star$ and $\sigma^\star$ orbitals are empty (fig. 2.2). Because of the lower splitting, the excitation of electrons from π to $\pi^\star$ is energetically favoured over any other transition, therefore the HOMO and LUMO levels are π and $\pi^\star$-orbitals.

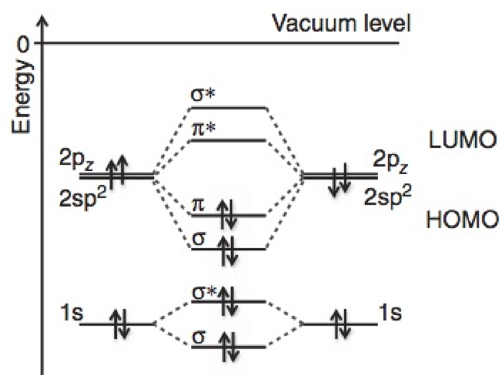

Figure 2.2: Example of the energy level diagram of an organic molecule.

The energy difference between the HOMO and LUMO levels determines the electronic properties of the material, therefore π-orbitals and the splitting between π and $\pi^\star$ have a very important role in organic semiconductors. π-orbitals are especially important when selecting a dopant or a metal for the injection of charges, because depending on the energy difference of the HOMO and LUMO with an electrode's conduction and valence band, hole or electron injection can be hindered because of the presence of a potential barrier.

Moreover, in organic compounds in the solid state π-orbitals are the means

of charge carrier transport, therefore it is very important to achieve molecular stacking in order to have good mobilities.

Density of States

The disorder intrinsic to organic compounds has profound effects on the *Density of States* (DOS), which in turn influences the transport properties of charge carriers, since it governs the hopping transport of a charge carrier between energy states.

The DOS of a large number of isolated organic molecules of a single species is simply a delta function, since the LUMOs and HOMOs all lie at the same energy level.

Inside of an organic film, though, many factors can influence the energy levels. The interaction of an excess charge carrier with the molecules of an organic semiconductor causes polarisation of the surrounding molecular environment, which in turn causes fluctuations in the energy diagram. These are caused also by the relaxation of the molecule and that of the lattice. Moreover, when working with polymers the energy levels inside the organic compound are randomly distributed around a value E_0 because the conjugation lengths don't have a fixed value. These conditions allow us to apply the central limit theorem, which predicts that the DOS follows a Gaussian distribution centred around E_0. [4]

$$\rho(E) = \frac{1}{\sqrt{2\pi}\sigma} \exp\left(-\frac{(E-E_0)^2}{2\sigma^2}\right) \tag{2.1}$$

where the parameter σ, the standard deviation of the distribution, is called the "disorder parameter" and measures the spread of the DOS. As we have hinted, this form of the DOS has a marked influence on the transport of charges in the film.

2.1.3 Transport Properties in Organic Semiconductors

Charge transport inside an organic semiconductor is governed by different phenomena from that of inorganic semiconductors.

Because of the lower dielectric constant of organic compounds, Coulomb interactions have a much stronger effect than within inorganic semiconductors. This means that a charge carrier within an organic film has a drastic effect on its surroundings, polarising and flexing the molecules it passes through. Because of this, a charge carrier inside an organic semiconductor can be modelled as the deformation it imposes to the molecular environment, which is a quasi-particle and is given the name of *small polaron*.

Since the relaxation energies of the molecular structure of an organic compound are rather high, the polaron tends to localise, rather than delocalise as an excitation of an inorganic semiconductor would. A consequence of the localisation is that the polaron doesn't move inside the material following the band theory, but by *hopping transport*.

Hopping transport occurs when a charge carrier jumps from a localised state to another, that means that the charges have to "hop" from the potential well of one molecular orbital to the next by quantum tunneling. The motion of the charge carrier proceeds incoherently between energy states.

Because of the disorder present in organic semiconductor, accurately predicting their charge transport properties is extremely difficult, since one has to consider factors such as the solid state distribution of the molecules and the testing conditions [9].

Mobility in an Organic Semiconductor

A pivotal parameter to describe the transport properties of an organic semiconductor is the mobility. In general, it is defined as the velocity v of the charge carrier per unit electric field E,

$$\mu = \frac{v}{E} \tag{2.2}$$

and in the conventional microelectronic units system it is measured in $\mathrm{cm^2V^{-1}s^{-1}}$. The mobility is tied to the current flowing through the organic semiconductor through the following equation: for a unipolar electron current

$$j = en\mu E \tag{2.3}$$

where n is the number density of electrons (while p would be the number density of holes). The current can be either *injection-limited* or *space-charge-limited* (SCL)[4].

An *injection-limited current* is drift-driven and only gives information about the injection process and not about the transport inside the bulk of the organic semiconductor, and thus doesn't yield any information on the mobility of the organic compound.

An *SCL current* can be obtained by using an *ohmic electrode*, which is an electrode able to inject more charges into the organic semiconductors than what can be transported through the bulk of the organic material. In this case the current is dominated by diffusion and can be used to infer the value of μ. Despite the name of the electrode, a current injected by an ohmic electrode does not follow Ohm's law: since the quantity of charges that can be transported away from the contact is limited by the characteristics of the organic semiconductor, there will be an accumulation of charges around the electrode. Thus, the ability to sustain an SCL current depends both on the injection barrier (the difference between the work function of the electrode and the ionization potential or electron affinity of the organic semiconductor) and on the mobility of the organic bulk, which sets a limit to the quantity of charges that can be transported through the material.

The mobility in organic semiconductors is generally dependent on the applied electric field and on the charge carrier concentration[10]. The mobility usually increases in value with increasing applied field and carrier concentration[4, 11],

even though there are very rare recorded cases where the contrary happens. The latter cases, where the trend is for the mobility to decrease with the increase of the applied fields, were explained by the presence of high disorder or high doping of the material[12, 13, 14, 15].

Charge Transport in Polymers

In polymers, polarons are localised inside π-orbitals, over a string of adjacent coupled monomers where they can delocalise in a coherent manner [4]. The mean number of monomers involved is given by the *effective conjugation length*, which determines the optical and electrical properties of the polymer. The mean number of π-conjugated monomers is usually between 5 and 30. Conjugation may be broken by a number of factors along a polymer chain, such as bending of the chain, torsion of the π-bonds, or other conformational variations of the chain.

Hopping transport is necessary, for example, for a charge carrier to pass from a π-conjugated part of a polymer chain to another. While intramolecular transport is much faster than the intermolecular one, which is why polymers with high molecular weight present the highest mobilities, hopping slows the charge carrier down, lowering its drift velocity and therefore its mobility.

A way to improve the electronic characteristics of polymer-based organic devices, such as the mobility, is to employ semi-crystalline polymers, which self-assemble in stacks tied together by π-bonds. This leads to improved conduction perpendicular to the stacking direction, while also increasing the π-conjugation length of the stack.

2.1.4 Doping in Organic Semiconductors

Organic compounds are usually insulators, because of their wide band gap, and therefore are not intrinsically semiconductors. In order to create a current flowing through the material, it is necessary to bring holes to the HOMO or electrons to the LUMO. This can be achieved by connecting the compound to a metallic electrode (called cathode if it injects electrons, anode if it injects holes), light exposure if the compound is a light absorber, or introducing dopants inside the compound that may act as electron donor or acceptor.

Contrary to inorganic crystals, substitutional doping is not feasible in organic semiconductors, because substituting an atom of an organic molecule would just create another neutral molecule. Therefore, doping is achieved by inserting molecular impurities inside the matrix of the material which act as donors or acceptors.

In order to p-dope an organic semiconductor, the impurity must have a very low laying LUMO, so that electrons find it energetically convenient to jump from the HOMO of the matrix to the LUMO of the impurity, increasing the hole density inside the semiconductor matrix. N-doping works with the same principle, but requires an impurity with a HOMO laying higher than the LUMO of the matrix, which increases the electron density of the matrix (fig. 2.3). These requirements

put serious restraints on the energy levels of the potential dopants, and are not easily satisfied[4].

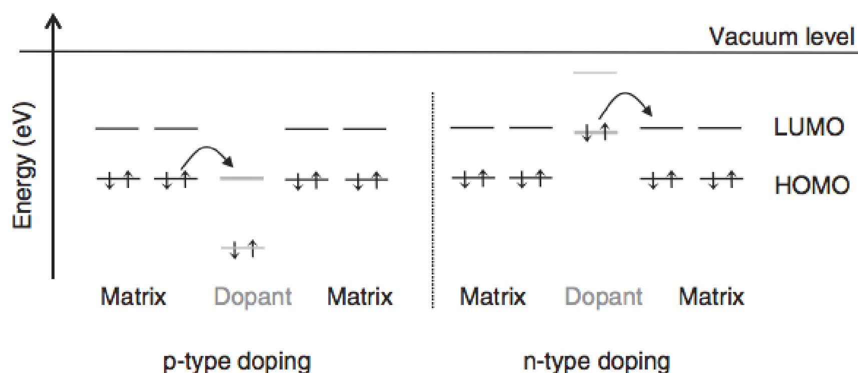

Figure 2.3: Scheme of molecular orbital levels for p- and n-type doping.

The simplest way to achieve doping is to expose the semiconducting film to the vapour or a solution of the desired dopant. This method, though, leads to inconsistent doping in time: the dopant molecules tend to diffuse out of the film easily; thus research is being poured into the subject to try and solve this problem.

2.1.5 Trapping in Organic Semiconductors

In semiconductor physics, a trap state is an energy level inside the band gap which has the ability to immobilise charge carriers, and thus may influence the local concentration of charge carriers inside the semiconductor. Traps can be shallow or deep, depending on the energy requirement necessary to free the charge carrier. This is given by the difference between the energy level of the trap and the electron affinity in the case of electron traps, or the ionization potential for hole traps[4]. Deep traps can impede the movement of a carrier for a very long time, which can be the order of days or even higher.

Trap levels can arise inside a semiconductor because of different reasons. The most common one, shared also by inorganic semiconductors, is the presence of a chemical impurity or defects in the order of the molecular structure. For example, the use of metal catalysts such as Pd or Ni is essential for the process of polymerisation, but traces of these metals may remain in the compound even after purification.

A common insulator used in solid state physics is SiO_2; its presence can be intentional or accidentally created by oxidation of a layer of Si exposed to air. SiO_2 presents, on the surface, H atoms bonded to the O terminations. The presence of OH groups leads to the creation of surface trap states relative to the LUMO of common organic semiconductors. The occurrence of this phenomenon in organic

devices is unfortunate, since the occurrence of trap states inside field effect transistors at the interface between semiconductor and insulator, where the conduction channel is created when the transistors are switched on, can severely modify the performance of the devices. In organic applications, the surface of the SiO_2 can be passivated by substituting the H atoms with organic molecules that render the surface inert. The downside of this process is that the wettability of the surface is thus strongly reduced, making it harder to deposit the organic semiconductor by spin-coating or similar processes which involve a solvent. Another method to passivate the surface is by coating the silicon dioxide with parylene C, which provides a surface with the same wettability as SiO_2 [16]. This process, though, doesn't eliminate the trap states, which are still present at the interface between SiO_2 and parylene C, it only makes it harder for charge carriers to reach them.

2.2 MIS Capacitors and Field-Effect Transistors

2.2.1 Metal-Insulator-Semiconductor (MIS) Capacitor

The metal-insulator-semiconductor capacitor (also called MOS if the chosen insulator is an oxide) is a capacitive structure which employs the electric potential applied to the metallic section of the device in order to draw charge carriers in the semiconducting section.

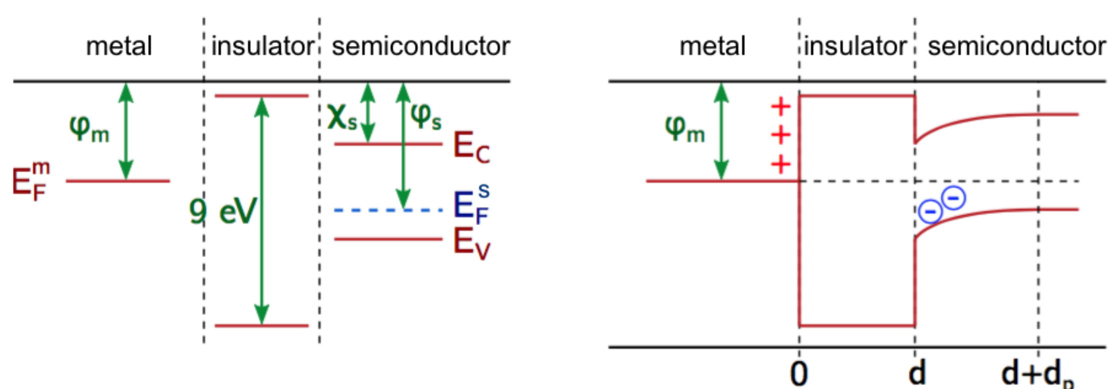

Figure 2.4: Example of the energy levels of a metal insulator semiconductor junction made of Al, SiO_2 and Si(p+) before (left) and after (right) contact. Before contact the heights of the Fermi levels $E_F^{(m,s)}$ are determined by the ionization potential $\phi_{(m,s)}$, while the height of the conduction band of the semiconductor (E_C) is determined by electron affinity χ_s. After contact the Fermi levels align, which creates a bending in the conduction and valence (E_V) bands between x=d and x=d+d_p, leading to an accumulation of charges in the depletion zone, which in turn produces an accumulation of opposite charge at the interface metal-insulator.

It is made of a semiconducting layer, an insulating layer and a metal electrode called gate. When the three materials are contacted, the Fermi levels of the metal and the semiconductor align, causing a bending in the conduction and valence band of the semiconductor. Because of level bending, a depletion zone at the interface between insulator and semiconductor is created, where minority carriers accumulate. Because of the excess of charge at the interface insulator-semiconductor, a corresponding excess of opposite charge accumulates at the interface metal-insulator (fig. 2.4).

Applying a potential bias between metal and semiconductor, it is possible to shift the Fermi levels at the interface so that there is no charge accumulated at the interfaces with the insulator. The potential which fulfils this condition is called threshold voltage V_{th}.

In our experiment, the injecting contact was chosen so as to have unipolar transport: that the entrance of one charge carrier species in the semiconductor would be hampered by the presence of a potential barrier, while the ejection of the opposite carrier species would be greatly favoured.

2.2.2 Inorganic Field-Effect Transistors

Field-effect transistors are extremely important in modern electronics, since they can act as amplifiers or as electronic switches, depending on the voltages applied. The field effect transistor (FET) is a circuit element with three terminals and it is the most widespread kind of transistor.

The FET is a unipolar device, meaning that the currents are dominated by only one kind of charge carriers at a time, which can be minority or majority carriers depending on the specific kind of the device.

The terminals of a FET are *source*, *drain*, and *gate*. The names of the terminals refer to their function: the current flows from the source to the drain, through an electric channel whose width is governed by the gate voltage. In most kinds of FETs there is a fourth terminal, the *body* or *bulk*, which connects source and drain and serves the purpose of biasing the device into operation but usually it is not connected to contacts other than source and drain. The materials which constitute source, drain and bulk are semiconductors, except for the gate that has to be built out of a metal-like material.

MOSFET

Let us focus our attention on the MOSFET, the metal-oxide-semiconductor field-effect transistor, which will allow us to make a comparison with OFETs. The basic layout of a MOSFET is shown in fig. 2.5. It is a four terminal transistor, in which source and drain must be inversely doped compared to the bulk. The gate is built over the bulk between source and drain, separated from the bulk by a thin layer of oxide, which provides electrical insulation. The junction gate-oxide-bulk is a MIS junction.

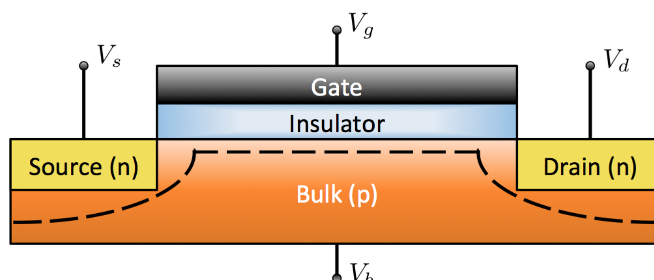

Figure 2.5: MOSFET layout. The depletion zone inside the bulk for small V_g is drawn.

Let us consider source and drain n-doped and the bulk p-doped. At the interfaces, depletion zones are created because the gradient in n and p densities generates a diffusion current, which is balanced at the equilibrium by a drift current created by the electric field that has arisen between depletion zones. When the device is off, no current can travel from the source to the drain because of the presence of the depletion zones at either side of the bulk. For the same reason, it is not sufficient to apply a voltage difference to source and drain in order to turn on the device, but a voltage has to be applied to the gate. When this happens, the system gate-oxide-bulk becomes a capacitor: the potential difference attracts minority carriers (electrons) from the bulk and creates an inversion zone at the interface with the oxide. When the gate voltage exceeds a threshold value V_{th}, the accumulation of charges at the interface opens a channel of minority carriers that allows current to flow between the source and the drain terminal.

The thickness of the channel is controlled by the applied bias on the gate and it limits the current. When the voltage difference between source and drain (V_d) reaches the order of magnitude of the gate potential, the current saturates inside the channel and it can't be increased unless the gate voltage is increased first.

2.2.3 Organic Field-Effect Transistors (OFETs)

Organic field-effect transistors are devices that employ the same working principles as FETs. The layout of the devices is in principle the same as that of MOSFETs[17]: the four terminals encountered in the previous section, drain, source, bulk and gate, are still present. The difference consists in the materials with which they are built: the heart of the device is the bulk, which has been substituted with a thin organic semiconducting film. Since charge carriers must be injected into the organic layer in order for conduction to begin, the device needs to have metallic reservoirs from which it can draw the necessary charge carriers. This is the reason why the source and drain contacts of an OFET must have metallic characteristics.

As is the case in inorganic transistors, when an OFET is turned on a transport

channel opens in the layer of organic semiconductor, in the region towards the gate contact, by drawing charges from the metallic contacts towards the interface with the oxide. Assuming L and W as the channel length and width, x as a spatial coordinate indexing the source-drain distance, h as the thickness of the organic semiconductor and d as the thickness of the insulator, the on-current is given by the following equation:

$$I_d = h \cdot W \cdot \rho \cdot \mu \frac{\partial V(x)}{\partial x} \tag{2.4}$$

where μ is the charge carrier mobility. Since the organic layer is one face of a plane capacitor, one can assume that the charge carrier density ρ is given by

$$\rho = \frac{\hat{C}}{h}(V_g - V(x)) \tag{2.5}$$

where $\hat{C}$ is the areal capacitance of the insulator. By adding the boundary conditions $V(0) = 0$, $V(L) = V_d$, we obtain an expression for the drain current which is completely analogous to the ones found for the inorganic device:

$$|I_d| = \frac{\hat{C}W}{2L}\mu \begin{cases} (2(V_g - V_{th}) - V_d)V_d & \text{if } |V_d| < |V_g| \\ (V_g - V_{th})^2 & \text{if } |V_d| \geqslant |V_g| \end{cases} \tag{2.6}$$

The device performance can be characterised by the current I_d flowing between source and drain; in this way, we can identify four different regimes of device operation.

- When $V_g < V_{th}$, the current I_d vanishes.

- When $V_d \ll V_g$, the current grows linearly with both voltages:

$$I_d = \frac{W\mu\,\hat{C}}{L}(V_g - V_{th})V_d \tag{2.7}$$

- When $V_d \lesssim V_g$, another term has to be introduced in eq. (2.7):

$$I_d = \frac{W\mu\,\hat{C}}{L}\left((V_g - V_{th})V_d - \frac{V_d^2}{2}\right) \tag{2.8}$$

  The term $\frac{V_d^2}{2}$ was previously ignored because it was vanishingly small. This is the quadratic regime.

- When $V_d = (V_g - V_{th})$, the current saturates:

$$I_d = \frac{W\mu\,C_{ox}}{2L}(V_g - V_{th})^2 \tag{2.9}$$

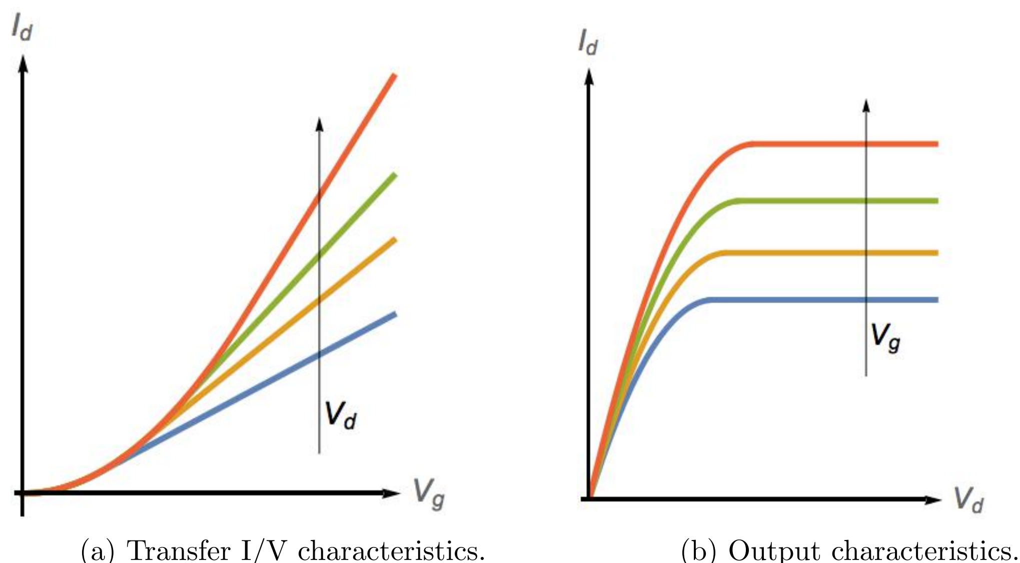

(a) Transfer I/V characteristics. (b) Output characteristics.

Figure 2.6: Transistor characteristics.

The equations above, called *Shockley equations*, which are also valid for inorganic MOSFETs, can be used to graph the dependence of the drain current on the gate and drain potentials (fig. 2.6): the resulting graphs describe the *transfer* and *output characteristics* and are unique for each device.

The threshold voltage V_{th} needs to be introduced to take into account the presence of phenomena such as doping or traps. Using the equations (2.6), one can graph the output and transfer I/V characteristics, from which informations about the semiconducting layer can be inferred. In fact, the presence of doping charges inside the semiconducting layer causes the device not to turn off at $V_g = 0V$, which means that the current in the transfer I/V characteristics graph doesn't vanish at that point but at lower or higher voltages, depending on the sign of the doping charges. Traps, instead, capture charge carriers and therefore impede the opening of the conduction channel, increasing the V_g necessary for conduction. In both cases there is a shift in the onset of the current I_d. This is also valid for both organic and inorganic devices.

Research on OFETs is a very active field, albeit one that has not yet been widely industrially exploited. Organic transistors could allow the construction of fully flexible devices[1], disposable smart-packaging devices, even biodegradable devices made from biocompatible and biodegradable materials[18].

2.3 The Kelvin Probe

The *Kelvin probe* is a device that allows the measurement of the work function of a material by measuring the contact potential difference between the surface of the

sample under study and a tip made of a reference material. The working principle of the Kelvin Probe is based on the continual measurement of the electrostatic forces between two materials.

A Kelvin probe circuit consists of a measuring tip (the probe), a voltage generator, a voltmeter and an ammeter (fig. 2.7) connected to the sample under study. The basic setup for a Kelvin probe experiment is given by two conductors arranged as a parallel plate capacitor, where the spacing between the two plates is dependent on time. The time dependence is thus transferred to the capacitance and the charge accumulated on the plates, creating a time-dependent current in the circuit, from which a measurement of the contact potential difference can be inferred. [19]

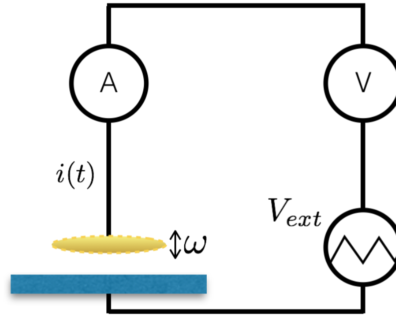

Figure 2.7: Basic layout of a Kelvin probing circuit.

The probe is made of a conducting material whose work function is taken as reference point, which is oscillated through piezoelectric actuators. The probe and the sample are positioned facing each other, in such a way as to create a capacitor, whose capacitance is continuously changed by the oscillation of the tip as the distance between the two "capacitor plates" varies. The variation of the capacitance induces a variation in the amount of accumulated charge on the plates, which in turn generates a current that can be measured with the ammeter.

Any two conductors have, in general, different work functions, which control the distance between the conduction levels (which in metals correspond to the Fermi level) and the energy of vacuum, that is the energy of a free electron. When the two conductors are brought into contact, the difference ΔW between work functions generates a potential difference $\Delta\varphi$ at the contact point; the two are tied by the following equation.

$$\Delta W = e \cdot \Delta\varphi \tag{2.10}$$

When contact is made between the two conductors, electrons will flow from the conductor with the higher Fermi level to the one with the lower Fermi level and a diffusion current will arise, until the two Fermi levels are aligned. Even though

the current vanishes almost immediately when the equilibrium of the system is reached, the work functions are not aligned and thus create a potential difference between the two materials. The two conductors, thus, behave like two capacitor plates with capacitance C, and the total flowed charge is given by

$$Q = C \cdot \Delta\varphi \tag{2.11}$$

where the expression for C depends on the shape and relative distance of the two conductors. If the surfaces of the two conductors facing each other are plane and parallel, the expression for the capacitance is

$$C = \epsilon_r \epsilon_0 \frac{A}{d} \tag{2.12}$$

where A is the area of the surfaces, d is the distance between them and ϵ_r is the relative permittivity of the dielectric between the two plates.

Let us consider the case where both the tip and the sample have flat surfaces facing one another. When applying an external bias, equation (2.11) becomes

$$Q = C \cdot (\Delta\varphi - V_{ext}) = \epsilon_r \epsilon_0 \frac{A}{d} \cdot (\Delta\varphi - V_{ext}) \tag{2.13}$$

If we assume that the tip oscillates around the equilibrium following the equation of motion $\Delta d \cdot \sin(\omega t)$, with Δd being the amplitude of the oscillation, the current flowing in the circuit is therefore

$$i(t) = \frac{d}{dt} Q = \frac{d}{dt} C \cdot (\Delta\varphi - V_{ext}) = (\Delta\varphi - V_{ext}) \cdot \frac{d}{dt} \frac{\epsilon_r \epsilon_0 A}{d + \Delta d \cdot \sin(\omega t)} \tag{2.14}$$

The dependence of the current on the relative distance between tip and sample is valid for any shape of the tip, and therefore for any expression of C. The Kelvin probe continuously modifies the applied bias V_{ext} in order to make the current flowing in the circuit vanish, and, from the measurement of the applied bias, the contact potential $\Delta\varphi$ can be extracted.

Kelvin Probing with Organic Materials

The previous paragraph investigated what happens when the Kelvin probe is used to study the work function of a conductor, while the focus of this work is to investigate electronic processes inside an organic semiconductor.

If HOMOs and LUMOs levels are considered instead of the conduction and valence bands, the description given above remains valid for any two materials that are brought into contact, even though the charge carrier mobility may be lower than in the case of intrinsic conductors, leading to a slower response of the sample under measurement. While with metals and inorganic semiconductors the redistribution of charges is almost instantaneous, when working with organic

semiconductors the characteristic times lengthen of five or six orders of magnitude because of lower mobility.

The response time of the organic material is, in general, much longer than the oscillation ω of the probe. During operation, the Kelvin probe reaches equilibrium with the injecting contact but not with the organic semiconductor. The slow charges travelling through the organic bulk are not compensated by the charges inside the probe, and thus they give their contribution to the contact potential difference and can be detected by the probe.

Since the Kelvin probe integrates all the contributions to the potential inside the sample layer, it can detect the presence of immobile charges deep inside the material, such as trap states, whose contributions will add to the measured potential.

2.3.1 Kelvin Probe Force Microscopy

The *Kelvin probe force microscopy* (KPFM) (or *Scanning Potential Microscopy, Volta Potential Microscopy, Surface Potential Microscopy, Scanning Electrostatic Potential Microscopy*) is a technique that combines the Kelvin probe method to measure contact potential differences with *atomic force microscopy* (AFM) [20].

The AFM allows to examine a surface with a resolution of fractions of nanometers, three orders of magnitude higher than the resolution that can be obtained by optical diffraction. The technique is based on the interaction between the surface and a fine tip, mediated by a force between the sample and the tip. The tip is usually positioned at the end of a cantilever, which is made to oscillate at its resonance frequency by a piezoelectric actuator. If the gradient of the force between the tip and the sample surface is not zero, there is a change in the compliance of the cantilever, which causes the tip to oscillate outside of resonance frequency. This modifies the amplitude of the cantilever oscillation, which is accurately monitored by a heterodyne laser interferometer (fig. 2.9). Thus from the amplitude changes one can extract the gradient of the force acting on the tip and, in turn, from the gradient the force itself.

The KPFM is based on the same working principle as the Kelvin probe, but in order to find the contact potential $\Delta\varphi$, instead of measuring a current, it measures the electrostatic force that arises between the AFM tip and the sample in the steady state, when the Fermi levels are aligned.

$$F_e = \frac{1}{2}\frac{\partial C}{\partial z}\left(\Delta\varphi\right)^2 \tag{2.15}$$

where z is the vertical distance between the tip and the sample.

Also, while the Kelvin probe measures the average of the contact potential difference over an area of the same order of magnitude as the tip, the KPFM allows to create a map of the contact potential difference of the whole surface with a resolution as high as a few tens of nanometers (2.8).

Experimental applications of KPFM

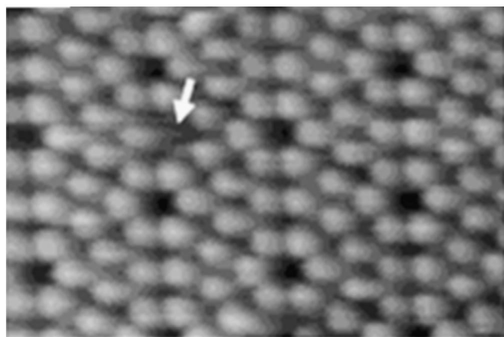

Figure 2.8: Atomic-resolution KPFM images of Si(111)-(7x7) with vacancy[21].

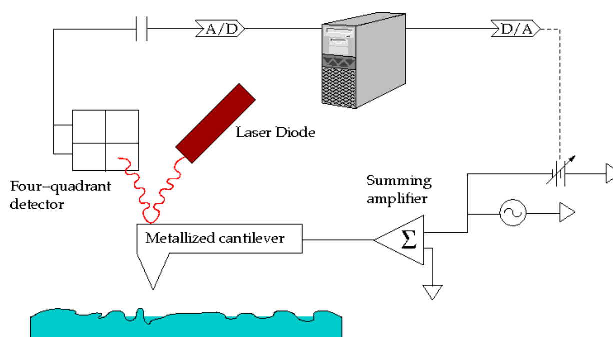

Figure 2.9: Layout of a generic KPFM control circuit.

KPFM is a very versatile technique which can be used also in extreme applications, such as in ultra-high vacuum or controlled atmosphere and it is possible to employ a number of different operating methods which can be used in different measuring conditions in order to enhance the resolution of the scanning apparatus. Its response time is faster than other scanning techniques and it is not limited by a poor conductivity of the sample, whereas its resolution is extremely high: the distance between tip and sample can be determined with an error of a single atomic monolayer, the lateral resolution can be as precise as a few tens of nanometers and the determination of the contact potential $\Delta\varphi$ has a sensitivity in the order of 1 mV[20].

With KPFM it is possible to study both organic and inorganic materials, in order to scan electronic and chemical properties. It is especially versatile with organic compounds, since it is not limited by the conductivity of the sample. For example, it has been used to give a direct determination of the DOS of amorphous organic semiconductors [22, 23], or to study charge trapping at grain boundaries between crystalline domains in polycrystalline films [24, 25].

2.3.2 Applications of KPFM to OFETs

In particular, KPFM was used to study transport properties in a thin organic film embedded in an OFET device [26].

The devices on which the study focused were p-type pentacene OFETs with a p^{++}-Si gate, a SiO_2/ PMMA double-layer gate dielectric, an evaporated polycrystalline pentacene layer, and Au top contacts, with a 5 μm channel length L (fig. 2.10). The presence of the PMMA layer was exploited to enable bipolar transport in the transistor channel. It is possible, using KPMF at a fixed position, to observe the regimes the devices can operate in, by applying the same potential U_C between the grounded gate gate and the top contacts, source and drain [27].

Different regimes are identified by different dependencies of the surface potential ϕ from U_C.

Multiple sweeps of U_C, from 20V to -30V and back to 20V with a sweep velocity, respectively, of -2Vs^{-1} and +2Vs^{-1}, were executed. The response of the organic layer, that is the surface potential recorded by the KPFM at fixed positions, is in fig. 2.10.

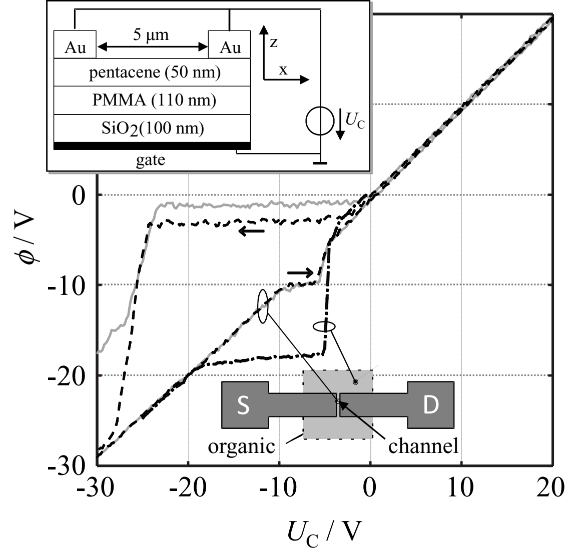

Figure 2.10: Surface potential ϕ vs. contact potential U_C. Grey line: first sweep inside the channel. Dashed line: fourth sweep inside the channel. Dash-dotted line: sweep outside of the channel.

The first series of sweeps were executed with the tip at the centre of the channel. From the starting point of $U_C = 20$V to $U_C = 0$V, the channel is full of positive charge carriers, exactly following the applied bias. At$U_C = 0$V, the channel depletes of charges, until at approximately -23V the injection of electrons starts, after which conduction is dominated by electrons. During the reverse sweep a similar process can be observed: the surface potential accurately follows U_C, until more or less at -10V the channel becomes electron-depleted. The channel remains depleted until -3V, where the device switches from electron to hole accumulation, after which the surface potential again follows the applied bias. The situation remained almost unchanged after four bias sweeps (fig. 2.10, grey and dashed line).

In order for the surface potential to reflect changes applied to the injecting contacts, the injected charges must be given enough time to reach the measuring position. Since the time they need depends on the channel conductivity, and since the conductivity depends on the carrier density, when the applied bias approaches 0V the few carriers present in the channel are not able to spread to the measuring position in time, making the surface potential saturate.

The sweeps were repeated by placing the KPFM tip several tens of micrometers away from the channel (fig. 2.10, dash-dotted line), showing that the saturation of the surface potential happened at a lower bias, while the hole injection began at a higher bias, which can both explained with an increased carrier transit time.

In order to study the front of injected charge carriers enter the channel during the sweep from negative to positive U_C, having already observed that the surface potential evolution enters a steady state after few sweeps, the measurement was repeated at 70 points inside the channel distant ~120nm from each other (fig.

2.11).

The behaviour of the device was examined by adapting to it the transmission-line model by Burns [28]. In this model the charging of the transistor channel is described by the surface potential evolution

$$\frac{\partial \phi(t,x)}{\partial t} = \frac{\mu}{2} \frac{\partial^2 \phi(t,x)^2}{\partial x^2} \tag{2.16}$$

where μ is the carrier mobility and x is the axis connecting the two top contact, with origin in the middle of the channel (fig. 2.11). While the bias Burns considered was a step function, the model in this study was subject to a bias ramp, with increase rate β:

$$U_C(t) = \beta \cdot t \tag{2.17}$$

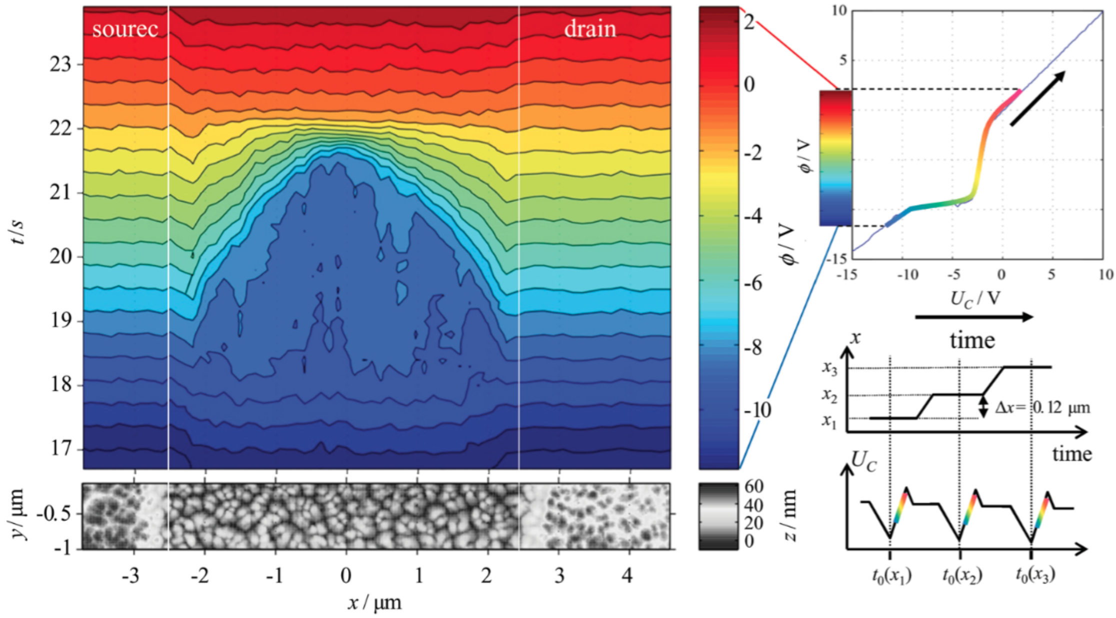

Figure 2.11: To the left: time evolution of the surface potential distribution upon an applied bias with increase rate $+2\mathrm{Vs}^{-1}$. To the right, from top to bottom: interval of U_C used in the picture on the left; incremental position of the KPFM tip at successive sweeps; $U_C(t)$.

The surface potential is given by the applied bias and the response function of the device $\chi(x,t)$:

$$\phi(x,t) = U_C(t) \cdot \chi(x,t) \tag{2.18}$$

By introducing the new variable Y,

$$Y = \frac{(x + \frac{L}{2})}{2(\beta \cdot \mu)^{1/2} \cdot t} \tag{2.19}$$

eq. (2.16) transforms to a second order ordinary differential equation:

$$4\chi(Y) = 4Y \cdot \frac{\partial\chi(Y)}{\partial Y} + \chi(Y)\frac{\partial^2\chi(Y)}{\partial Y^2} + \left(\frac{\partial\chi(Y)}{\partial Y}\right)^2 \tag{2.20}$$

The right contact can be ignored and the equation can be solved with the conditions that the response at the left contact is $\chi(0) = 1$, while $\chi(\infty) = 0$. The solution can be found numerically, but it can be approximated by:

$$\chi(Y) = \begin{cases} 1 - 2Y & \text{if } Y < \frac{1}{2} \\ 0 & \text{if } Y \geqslant \frac{1}{2} \end{cases} \tag{2.21}$$

Thus, writing the exp orm for Y and using (2.17) and (2.18):

$$\chi(x,t) = \begin{cases} \beta \cdot t - \left(x + \frac{L}{2}\right)\left(\frac{\beta}{\mu}\right)^{1/2} & \text{if } x + \frac{L}{2} < (\beta\mu)^{1/2} \cdot t \\ 0 & \text{if } x + \frac{L}{2} \geqslant (\beta\mu)^{1/2} \cdot t \end{cases} \tag{2.22}$$

The time required for the front wave of carriers to reach the middle of the channel ($x = 0$) is

$$\tau = \frac{L}{2(\beta\mu)^{1/2}} \tag{2.23}$$

Inserting the experimental data $L \simeq 5\mu$m, $\tau \simeq$3s, $\beta = 2$Vs^{-1}, the mobility for charges outside of the channel, where the electric field was lower than between the contacts, was found to be lower than $2 \cdot 10^{-8}$cm^{2}V^{-1}s^{-1}, almost eight order of magnitudes lower than the one found for the *on*-state of the device, which was 0.14cm^{2}V^{-1}s^{-1}.

From OFETs to MIS capacitors

This experiment described in the previous paragraph showed that charge carriers penetrate into the organic layer also at relatively far distances, multiple times the length of the conduction channel, and provided a way to estimate the charge carrier mobility at low electric fields. The questions arise of whether this is a phenomenon that is limited to distances in the order of tens of micrometers or if it is observable at distances orders of magnitude bigger, and whether it is still possible to estimate the charge carrier mobility at low electric fields.

The objective of this thesis is to investigate these questions and provide an answer to them. The devices used will be MIS capacitors with a conducting channel in the order of centimetres. They will be subjected to a low frequency periodic bias and the movement of charges inside the channel will be tracked at the steady state by measuring the surface potential at increasing distances from the contact with the use of a Kelvin probe.

It will be investigated whether the charges are indeed able to spread centimetres away from the contact, and if so the transport properties will be analysed in order to find a measurement for the charge carrier mobility inside the organic semiconductor.

Chapter 3

Experimental Setup

The objective of this experiment is to analyse the lateral transport of charge carriers inside of an organic semiconducting film. By lateral transport we mean the movement of charges inside the semiconducting layer perpendicularly to the normal of the film, and therefore the movement of charge carriers inside the film. In particular, in our experiment the charge carriers move in MIS-capacitors at the interface between insulating oxide and organic semiconductor. This phenomenon is known in literature, having already been observed in organic layers constituting transistors [26].

The devices in which lateral transport was studied are organic MIS-capacitors of macroscopic dimensions, which were charged and discharged by a low-frequency periodic bias applied between the metal and the semiconductor. By using a Kelvin probe setup, we observed the flow of charge carriers in and out of the organic semiconducting layer, and therefore the charging and discharging of the capacitor. This would allow the inference of the electronic properties of the semiconductor at low fields and low currents without a direct current determination, but simply observing the evolution of the surface potential of the semiconductor.

At the same time, we built OFET samples with the same materials and procedure. The extracted charge carrier mobility could be compared to the experimental results obtained with the Kelvin probe measurements.

Moreover, the influence of different injection potential barriers under these measuring conditions was investigated.

In this chapter the layout of the samples, the materials used to build them and experimental methods with which they were analysed are introduced.

3.1 Layout of the samples

The samples built in this work were MIS capacitors or transistors. The MIS capacitors were the samples meant to be examined with the Kelvin probe, while the transistors would be investigated with a FET probe station, which allows the measurement of transistor characteristics. Since the Kelvin probe setup was kept

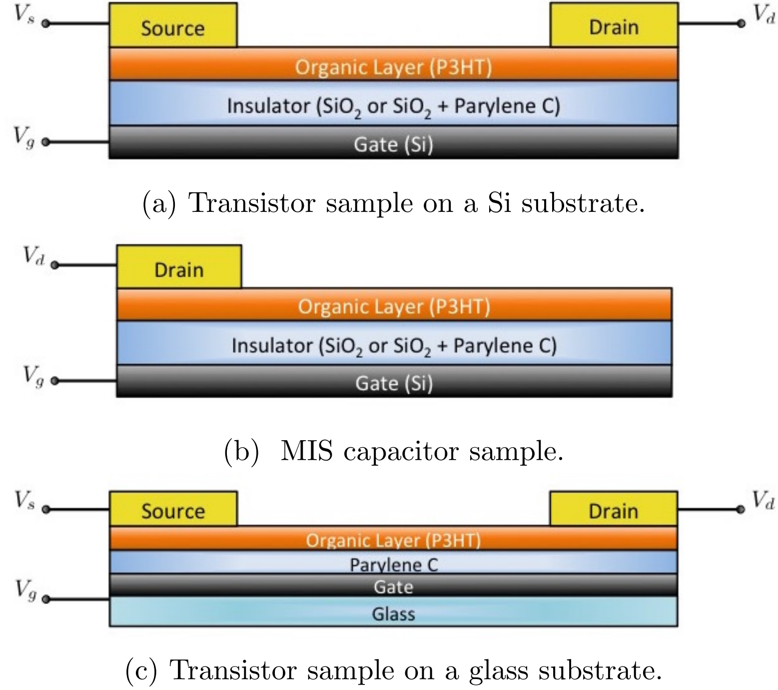

(a) Transistor sample on a Si substrate.

(b) MIS capacitor sample.

(c) Transistor sample on a glass substrate.

Figure 3.1: Vertical layouts of the samples.

in air and the FET probe station was positioned inside a nitrogen-filled glovebox, the MIS capacitors would have to be exposed to oxygen during measurements while the transistors would remain in N_2-atmosphere. Since O_2 is a dopant for the organic semiconductor used in this work, the finished samples were encased in a protective inert plastic layer to reduce oxygen contamination. The vertical layouts of the samples are in fig. 3.1 (encasing layer not shown).

Most of the samples were built over a Si/SiO_2 substrate, which would serve as gate electrode in the following measurements, while for one batch transistors were built over glass substrates, too.

The MIS capacitors samples had three simple L shaped electrodes each (fig. 3.2c). The "upper" part of the L was used to contact the electrode, while the "lower" part was needed to have a wide charge injection interface. In analogy with transistors, the bottom silicon layer and the top electrode were dubbed, respectively, gate and drain.

The transistor masks used, instead, allowed to build six long and six short transistors per sample (fig. 3.2a). The ones which were used for measurement had a channel length L of 50 μm, while the channel width was 900 μm.

In total 7 batches of samples were fabricated, each comprehended MIS capacitors and transistor samples. Each batch was made at most of four samples, because of limitations given by the instruments employed in the building procedure. The characteristics of the batches are listed below.

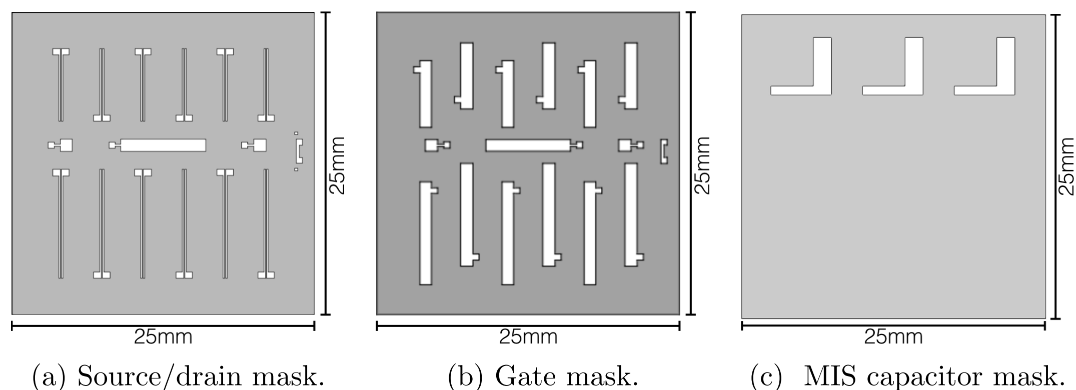

(a) Source/drain mask. (b) Gate mask. (c) MIS capacitor mask.

Figure 3.2: Layouts of the masks used to deposit the contacts on the substrate.

Batch number	Parylene C insulation	Top electrodes
Batch 1	No	Au
Batch 2	Yes	Au
Batch 3	Yes	Au
Batch 4	Yes	Ag
Batch 5	Yes	Ag
Batch 6	Yes	Au
Batch 7	Yes	Ag

3.2 Materials

3.2.1 Regioregular Poly(3-hexylthiophene-2,5-diyl)

The organic semiconductor used to fabricate the devices studied in this work is ***regioregular poly(3-hexylthiophene-2,5-diyl)*** (**P3HT,** linear formula $(C_{10}H_{14}S)_n$), produced by *Sigma Aldrich*. Since the material is stored in air, we have to consider that it might be unintentionally p-doped.

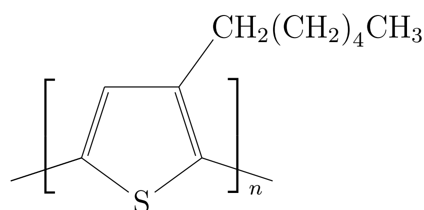

Figure 3.3: Poly(3-hexylthiophene-2,5-diyl).

This material is well known in literature: it has been thoroughly investigated because of its good solubility in organic solvents, the resistance to degradation and the possibility to reach relatively high charge carrier mobilities under the appropriate processing, which make it a suitable semiconductor for transistors and solar cells. It was the first polymer to reach a mobility one tenth that of amorphous silicon [9].

The monomer of P3HT is depicted in fig. 3.5. One molecule of P3HT is formed

by hundreds of such units[1], which create a one-dimensional macromolecule. The compound is referred to as ”regioregular” because the covalent bond between one repeating single unit and the next is always between the same two atoms relative to the position of the side chains. The resulting molecule has all side chains point in the alternating direction with respect to the backbone of the molecule, which leads to more ordered morphologies in the semiconducting film (fig. **??**). Because of its polymeric nature, the dominant interactions are Van der Waals forces, which govern the interaction between molecules on the same plane, and π-interactions, which are the main vector of interaction between molecules laying in two adjacent planes. This allows for the formation of pseudo-crystals in which P3HT molecules tend to stack themselves in an ordered fashion: polymers that assemble in such a way are called semicrystalline.

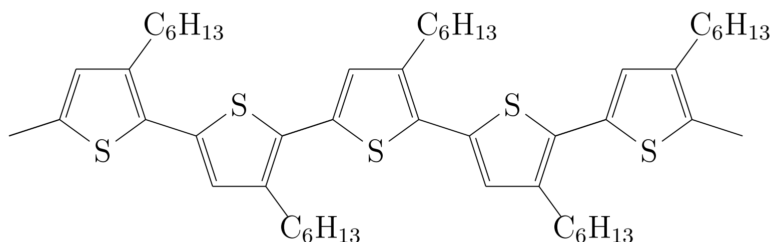

Figure 3.4: Regioregular polymeric assemblage of regioregular P3HT single units.

The charge carrier mobility in P3HT is maximum along the backbone of the molecules, since it is mediated by covalent bonds; it is lower but still relevant perpendicularly to the plane of the molecules, where the vectors for transport are π-bonds, and it is vanishing in the direction of the side chains, whose presence greatly impairs charge transport.

The pseudo-crystalline regions are much smaller than the length of a single P3HT polymer: since the polymeric structure is not rigid, the backbone of the molecule often bends a few times. It is possible, therefore, that a single molecule of P3HT takes part in the formation of a number of pseudo-crystalline regions. When a charge carrier encounters such bend in the polymer, its mobility decreases dramatically, since it has reached the end of a π-conjugated part of the chain and has to resort to hopping transport to travel further.

The side-chains around the axis of the repeating unit allow for solubility in organic solvents, such as toluene or chlorobenzene, which makes it ideal for wet processing. The wet processing used in this work is *spin-coating*, which consists in the following process: the organic compound to be spin-coated is dissolved in a suitable volatile organic solvent; the solution is then deposited on the sample, which is then spinned at thousands of *rpm* for a few seconds. The spinning causes the solvent to evaporate and allows to create homogeneous thin films of organic

[1]In the P3HT used in this work, one polymeric chain contains between 90 and 270 monomers.

matter in a very simple and cheap way. To make sure that the solvent is completely evaporated, the sample is then annealed on a hot plate for a few minutes. The characteristics of the resulting layer will depend on the concentration of the semiconductor in the organic solution, on the number of rotations per minute, and on the temperature and annealing time.

The ionisation potential and the electron affinity of the material lay, respectively, at -3.1 eV and -5 eV with respect to the energy of vacuum E_{vac}.

When it is stored in air, the material presents itself as a thick dark-grey powder. When it is dissolved in toluene or chlorobenzene, which are transparent liquids, the solution acquires a bright fuchsia color, which darkens into violet after spin-coating.

P3HT is photosensitive and therefore has to be shaded from light as much as possible, in order to slow down the degradation of the material.

3.2.2 Parylene C

Parylene C is an inert plastic which has the same wettability as SiO_2 and its dielectric constant is 3.15 at low frequency signals. It has a melting temperature of 290°C and it can be deposited by chemical vapour deposition (CVD), creating a thin, uniform and optically transparent polymeric layer which is stable under vacuum, a pivotal characteristic needed when transferring samples to and from the storage nitrogen-filled gloveboxes.

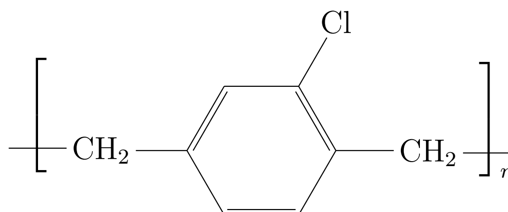

Figure 3.5: Parylene C.

Within our samples it serves the double purpose of reducing the voltage leakage due to imperfections in the SiO_2 insulating layer, and to passivate the traps which are present at the SiO_2 surface due to the hydroxil terminal groups. An additional encapsulation layer of Parylene C was deposited on the finished samples, in order to reduce oxygen and water vapour infiltration in the P3HT layer. Other than protecting the organic semiconductor from doping, the encapsulation layer doesn't influence the measurements.

The Parylene C layer in our devices was deposited with a *PDS2010 Coating System*.

3.2.3 Injecting Electrodes

The top electrodes to inject charges in the semiconducting layer were deposited by vacuum sublimation; masks were used to deposit the contacts in the desired shapes (fig. 3.2). The metals for the electrodes were chosen to be either gold (Au)

or silver (Ag) because of their different work function and thus expected different injection barriers towards P3HT. In fact, the literature values of the Fermi level of gold (as deposited by the evaporator used in this work) is at -4.9 eV, while silver's is at -4.2 eV. Thus the injection of holes into P3HT should be ohmic with gold electrodes and limited by a Schottky barrier with silver electrodes. By creating samples with either metal, we can provide a comparison of the performances of the devices with and without a Schottky injection barrier.

3.2.4 Glass and Si/SiO_2 Substrates

For the fabrication of our devices we used two kinds of substrates: glass and Si/SiO_2. They were used as base over which the organic layers of P3HT and Parylene C and the electrodes were deposited. The Si/SiO_2 also provided the opportunity to use the Si layer as bottom electrode for the MIS capacitors and as gate for the transistors.

The Si/SiO_2 substrates were cut out from commercially available silicon wafers, which consist in a highly positively doped ((p^{++})Si, thickness 625 μm) substrate with a layer of silicon dioxide deposited on top ((250 ± 12.5) nm thickness) as insulator. The glass was pre-cut optical glass.

Because of limitations given by the instruments used during the building process, the substrates had to be squares with sides of 25 mm.

3.3 Sample preparation

The samples used in this work were custom built, so that they would fit the requirements of the measuring apparatus.

The samples were built in a bottom-gate configuration. Because of the sensitivity to oxygen of the organic semiconductor used, almost every step until the final protective casing was performed under a nitrogen atmosphere. We will have a detailed look at the fabrication of the layouts in fig. 3.1a and 3.1b, and then explain briefely the different processing needed to obtain 3.1c.

Fabrication of samples on Si/SiO_2 substrates

The substrates on which the samples were deposited were custom cut with a glass cutter from Si/SiO_2 wafers. The silicon layer was later used as gate for the devices. The substrates were then cleaned at room temperature in an ultrasonic cleaner (fig. 3.6a), first for ten minutes in acetone[2] and then for ten minutes in isopropanol[3].

For every batch of samples except for the first, a further insulating layer of Parylene C was added on top of the SiO_2 by CVD.

[2] $(CH_3)_2CO$

[3] Isopropyl alcohol, C_3H_7OH

After the aforementioned steps, which involved exposure to air, the substrates were inserted into a glovebox filled with nitrogen atmosphere, where they were spin-coated with a solution of P3HT dissolved into toluene[4] with a concentration of 10mg/1ml. The thickness of the resulting semiconducting film was of ∼60nm[5]. After spin-coating, the samples were annealed at 110°C on a hot plate for five minutes, during which the P3HT formed local pseudo-crystals. It has been shown that varying the annealing time and temperature strongly influences the electronic behaviour of the P3HT layer[29].

The next step was the deposition of the contacts, which was achieved by vacuum sublimation (fig. 3.6b, 3.6c). The metals used were gold or silver, and the thicknesses deposited were ∼30nm for the gold contact and ∼50nm for the silver contact. During the procedure, the substrates were placed behind masks which allowed to obtain the desired contact layout (fig. 3.2). The top contacts were deposited without taking the samples out of the nitrogen atmosphere, in order to avoid oxygen contamination especially at the interface between the top contact and the semiconductor.

The final step was to encapsulate the samples in a thick layer Parylene C, so as to reduce the effects of oxygen infiltration in the semiconductor layer and to protect it from humidity, thus allowing to perform measurements in atmospheric conditions, as the Kelvin probe setup required. Unfortunately, the placement of the samples in the CVD machine involved a quick, unavoidable exposure of the organic layer to normal atmosphere.

After fabrication, the samples were stored inside the nitrogen filled glovebox and wrapped in aluminum foil, in order to protect them from oxygen poisoning and light degradation. It has been shown that negative effects of the presence of oxygen inside P3HT and other organic semiconductors can be reduce by storing the samples in N_2-atmosphere, because of the degassing of oxygen [30].

Fabrication of samples on glass substrates

The procedure followed was similar to the previous case, with some differences.

The glass substrates used were already factory cut to the right size. They were cleaned, as described before, using the ultrasonic cleaner with acetone and isopropanol. The following step consisted in the deposition of the gate contacts by vacuum sublimation with a chromium adhesion layer, which was followed by the deposition of Parylene C via CVD. The Parylene C layer thickness was chosen so as to have the same areal capacitance as the SiO_2/Parylene C insulation layers of the Si/SiO_2 substrate based devices. The following steps were the same as in the previous paragraph.

---

[4] C_7H_8

[5] The thickness was measured with a *Bruker DEKTAK XT* surface profiler.

(a) Ultrasonic cleaner.

(b) Vacuum sublimation setup.

(c) Vacuum sublimation chamber.

Figure 3.6: Ultrasonic cleaner and vacuum sublimation setup used in the building process.

3.4 Measuring Setup

3.4.1 Kelvin Probe Setup

For the Kelvin probe measurements various electronic modules had to be used (fig. 3.8). In order to ensure the correctness of the measurements, the grounded terminals of all modules were connected together. The schematic layout of the circuit is in fig. 3.7.

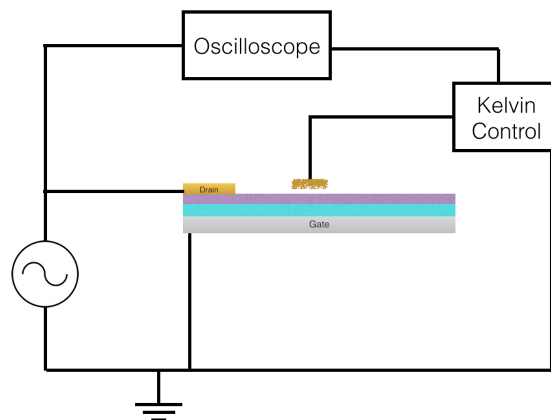

Figure 3.7: Schematic layout of circuit realized with the Kelvin Probe setup.

Kelvin Probe

The probe and corresponding control unit used in this work are the *Kelvin Probe S* and the *Kelvin Control 07* fabricated by the *Besocke Delta Phi G.m.b.H.*. This apparatus, which has a wide range of operating conditions (if needed, it can function from 4K to 220°C), was chosen because of its greatly reduced costs in comparison with AFM machines, due to the macroscopic dimension of the probing tip.

The probe is a circular horizontal grid made of gold (Au), 3 mm in diameter (fig. 3.8b), which is oscillated by a piezoelectric drive. The probe is protected by a thick metal grid on the sides and on the top, both because of its fragility and in order to reduce to a minimum capacitative coupling with the surroundings (fig. 3.8c). The probe and the protective grid are fixed to an horizontal arm mounted on a tower on which it can be moved on the vertical axis using a digital micrometer. Under the probe lays the support where the samples can be positioned for measurement, which is also movable in a plane by two micrometers (fig. 3.8d). Since the probe is made of gold, this material is used by the apparatus as fixed reference for the measurement of surface potential differences.

The Kelvin Control module has a built-in preamplifier and a lock-in amplifier with variable gain, which locks automatically to the oscillating frequency of the

probe in order to reduce background noise. The time constant of the amplifier can be controlled, too, and it can be made short or long depending on the user's needs. The module also has an analogical ammeter that shows the instantaneous current flowing in the circuit; this current must be kept low in order not to overload the system and has to vanish during measurements. If needed, an offset voltage between -5V and +5V can be applied to the probe from the control module. From the module, the amplitude of the oscillation of the probe can be controlled[6].

There are two output channels: the *CPD*, which provides the contact potential difference between the probe and the sample, and the signal monitor, *sig. mon.*, which gives the current flowing in the system due to the continuously changing capacitive coupling between probe and sample.

The module has two modes of operation: manual and automatic.

When manual mode is selected, current flows in the circuit because the feedback system that zeroes the current is turned off. This operation mode is useful when placing the probe in place over the sample, since the circuit current increases dramatically when the probe nears the surface of the sample. Usually, during this operation a voltage offset is applied to the probe, in order to make the current bigger and thus more easily measurable. In this case, the *CPD* signal is 0, while the *sig. mon.* is a periodic signal. The probe must not touch the surface of the sample because it could be damaged or contaminated, while it should be as close to the sample surface as possible in order to reduce background noise.

The automatic mode, instead, operates by zeroing the current between probe and sample, adjusting the probe potential to the surface potential of the sample in order to zero the electric field in between them to get a vanishing electronic coupling. This mode is used to acquire data on the sample, since the setup now works as described in paragraph 2.3. Contrary to the previous case, the *sig. mon.* is now 0, while the *CPD* can be a constant or an oscillating signal, depending on the voltage applied to the sample.

Oscilloscope & Digital Multimeter

When operating in automatic mode, the output *CPD* signal given by the Kelvin control module is monitored by a digital multimeter for DC measurements (fig. 3.8e) or by a DSO1012A digital oscilloscope for AC measurements.

When the manual mode is used to adjust the probe over the sample, the oscilloscope is instead used to monitor the output voltage of the *sig. mon.*. Together with the built-in ammeter of the Kelvin control, it is used to make sure that the probe is close enough to the sample to give a strong signal, but not close enough to touch the sample. When this happens, the circuit overloads with current, lighting the red LED next to the ammeter.

[6]but not the velocity, which has to be constant. This means that increasing the amplitude of the oscillation increases the period, too

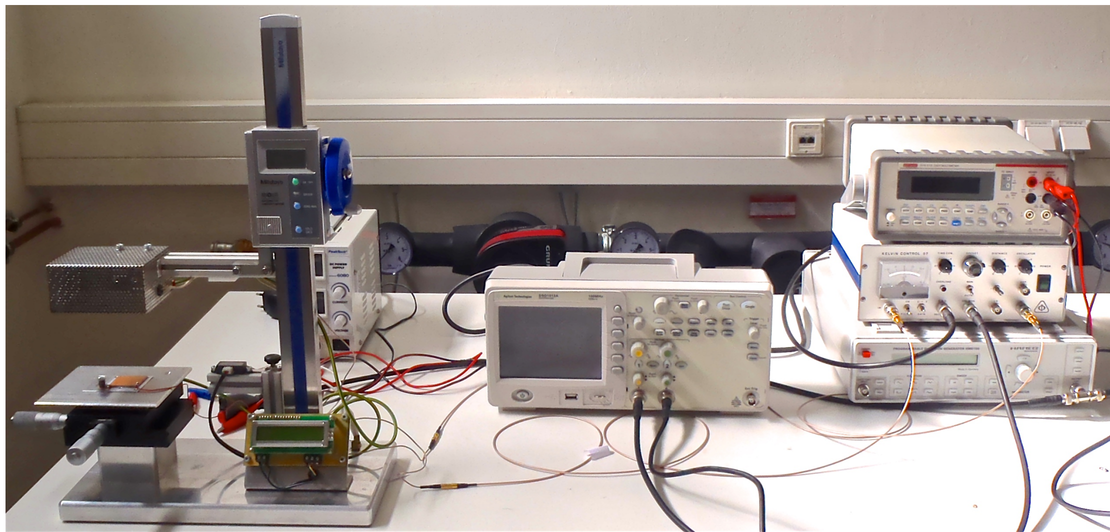

(a) Kelvin probe measuring setup.

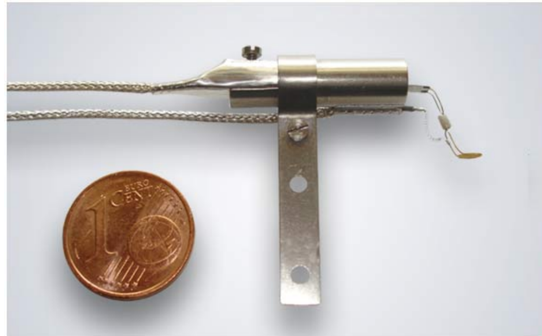

(b) Measuring probe (photo from catalogue).

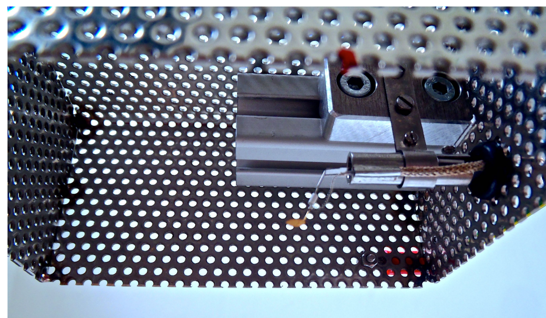

(c) Measuring probe and protection grid.

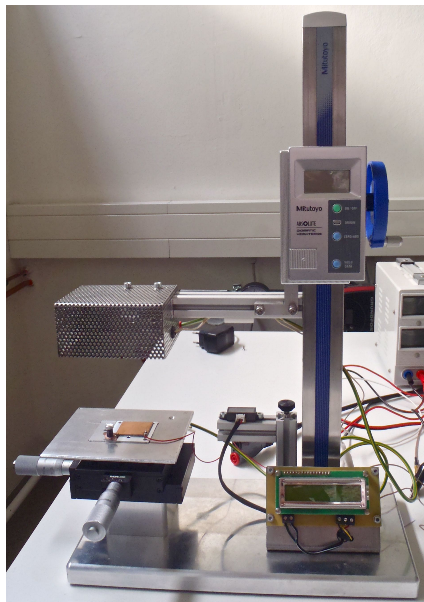

(d) Sample measuring layout.

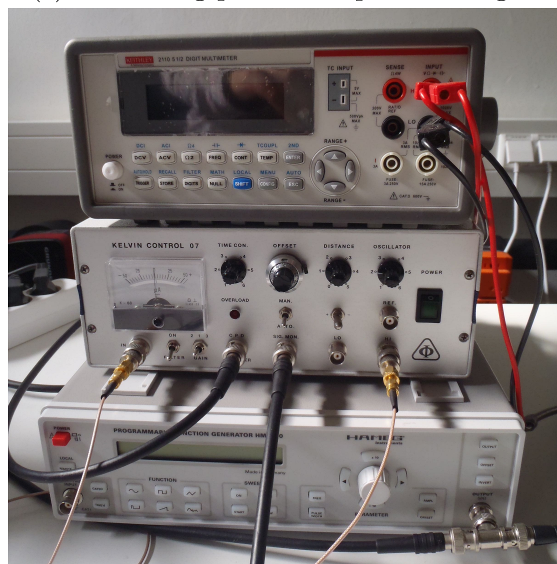

(e) Modules from top to bottom: digital multimeter, Kelvin Control 07, function generator.

Figure 3.8: Kelvin probe experimental setup.

Function generator & DC power supply

The voltage biases required for the measurements are supplied by two different modules: a DC power supply by *PeakTech* and a programmable function generator HM8150 by *Hameg Instruments*. The DC power supply can be adjusted to output a constant current or a constant voltage, as needed.

The function generator can output six different kinds of periodic signals: a sinus wave, a rectangular wave, a triangular wave, a periodic impulse, a chainsaw tooth wave and an arbitrary wave. These signals can be adjusted in amplitude and frequency, and a constant offset can be added to the output signal. In all cases, the output can be modelled by:

$$\underbrace{V_1}_{\text{DC}} + \underbrace{f(t, V_0)}_{\text{AC}} \tag{3.1}$$

where V_1 is a constant offset and V_0 the amplitude of the AC part.

3.4.2 FET probe station

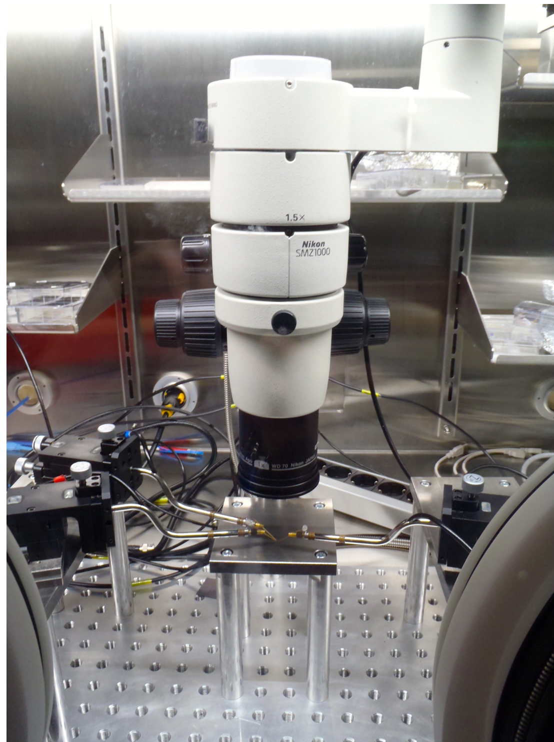

Figure 3.9: Part of the FET probe station that was kept in the nitrogen-filled glovebox. At the lower sides of the image, the gloves used to work inside the glovebox are partly visible.

The FET probe station is the apparatus that was used to measure the transfer and output characteristics of the transistors and lies partly inside the nitrogen-filled glovebox (fig. 3.9). The measuring module is a *Keithley SCS4200 Parameter Analyzer*, which lies outside of the glovebox and allows to perform various tests on many kinds of samples through a computer interface.

The samples under study lie inside the glovebox over an aluminum base. The samples are connected to the module by applying needles of tungsten covered with gold to the contacts, which can pierce through insulating layers when possible. The needles are used both to apply a voltage bias to the electrodes of the sample and to measure the current that flows through the sample.

The needles are moved by micrometers which allow movement in all three directions. Moreover, a digital microscope is placed over the aluminum base and it is connected to the computer interface in order to provide a zoomed view of samples.

3.4.3 Sample Connection

The completed samples had to be connected to the measuring apparatuses in order for measurements to begin. The connection was executed differently for the transistor samples and the MIS capacitor samples.

Transistor samples

The transistor samples built on the silicon substrate used the substrate as gate. Since, during the building process, some of the Parylene C used for encapsulation had been accidentally deposited on the bottom of the samples, the bottom silicon was painted with silver conducting paste, which would dissolve Parylene C and ensure a conductive connection to the gate. The treated sample was then rested on the aluminum base of the FET probe station over a copper plaque. The source and drain contacts were contacted by being pierced through with the gold needles of the probe, while a third needle was contacted to the copper plaque for the gate connection.

The transistor samples built on glass substrates needed no further processing. The contacting procedure required only piercing the contacts with the conductive needles.

MIS capacitor samples

The capacitance area was confined by gently scratching the P3HT and Parylene C at the surface of the sample, so as to create three isolated areas 5 mm by 20 mm, each containing one charge carrier injecting top electrode. This meant that the active area of the device for the measurement of lateral transport was around 15 mm in length, the top electrode being 4.75 mm in length. The scratching served the double purpose of limiting the loss currents and to limit the measurements

to one dimension. The gate contact was the same for all three electrodes. Each electrode was then welded with silver paste to a thin copper wire, with which was used to apply the required voltage biases (fig. 3.10a).

The gate of the MIS capacitor was also painted with silver paste and confined from the top electrodes by scratching away the P3HT that had dripped from the sides of the substrate during spin-coating. The external connection with the copper wire was achieved on the top of the sample, so that the sample could lay flat during the Kelvin probe measurements. The wire was attached with silver paste to a small area from which the P3HT and Parylene C had been scratched away and that had been connected with silver paste to the bottom gate.

To ensure that the wires had been connected correctly, all connections were checked with a multimeter.

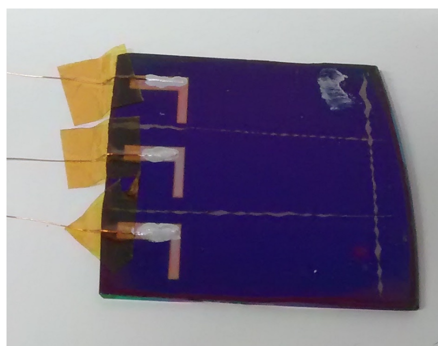

(a) MIS-capacitor with all three top electrodes connected. The scratching of the upper surface to delimit the operation area is present. The gate hasn't been connected yet.

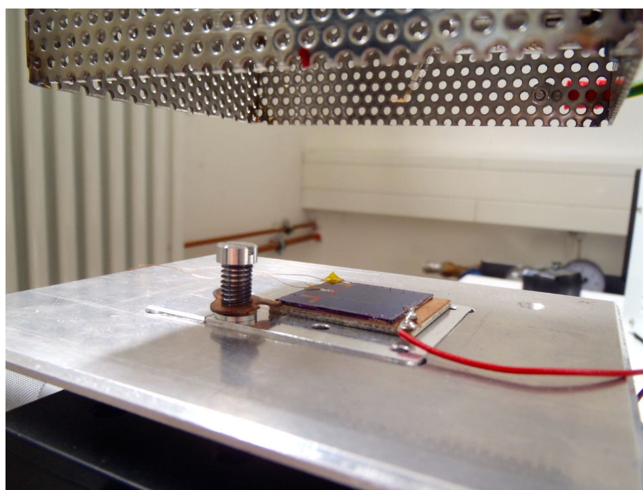

(b) MIS-capacitor connected and laid on the copper plate, under the Kelvin probe. Before measurement could begin, the probe had to be lowered almost to sample level.

Figure 3.10: Sample connection: MIS-capacitors.

To further ensure that the gate had the desired potential, the sample was laid on a copper plaque, which for most measurements was grounded. This was done also to ensure that the sample didn't move during measurement, since the copper plate was held in place by a spring (fig. 3.10a).

Since the connection of the gate required scratching away part of the top organic coating, part of the channel length of one electrode per sample had to be destroyed. This operation rendered the electrode unsuitable for measurement. Thus, the choice of where to connect the gate was made by observing which of the three electrodes seemed visually to have the most fabrication defects, or which was most damaged by the scratching operation.

Of the remaining two electrodes, both underwent measurement and were analysed.

3.5 Device Characterization

3.5.1 Areal capacitance of the devices

We can define $\hat{C}$ as the areal capacitance of a device, when it is considered as a plane capacitor with plates given by the organic layer and the gate, be it a transistor or a MIS-capacitor. Because of the Parylene C layer added on top of the SiO_2, this term is different for each batch of devices, because, while within each run of the CVD machine the thickness layer deposited on the devices is constant, it is almost impossible to deposit the same amount of Parylene C with two different runs of the CVD machine. Thus, the thickness of the Parylene C layer was measured for each sample with a *Bruker DEKTAK XT* surface profiler multiple times, which were averaged to give a single value; the error assigned to the measurement was the standard deviation of the mean.

Since the permittivities of SiO_2 and Parylene C [31] are, respectively

$$\begin{aligned} \epsilon_{SiO_2} &= 3.9 \\ \epsilon_{PC} &= 3.15 \end{aligned}$$

while the formula for the areal capacitance $\hat{C}$ is

$$\hat{C}_i = \frac{\epsilon_0 \epsilon_i}{d_i} \qquad i = \mathrm{SiO_2},\ \mathrm{PC} \tag{3.2}$$

where d_i is the thickness of the layer under study, we can calculate the total capacitance of the device by considering the two layers as series capacitors

$$\hat{C}_{\mathrm{tot}} = \left(\hat{C}^{-1}_{\mathrm{SiO_2}} + \hat{C}^{-1}_{\mathrm{PC}}\right)^{-1} = \frac{\epsilon_0 \epsilon_{\mathrm{SiO_2}} \epsilon_{\mathrm{PC}}}{\epsilon_{\mathrm{PC}} \cdot d_{\mathrm{SiO_2}} + \epsilon_{\mathrm{SiO_2}} \cdot d_{\mathrm{PC}}} \tag{3.3}$$

The error associated to the found value is given by error propagation.

$$\sigma_{\hat{C}_{\mathrm{tot}}} = \sqrt{\left(\frac{\partial \hat{C}_{\mathrm{tot}}}{\partial d_{\mathrm{SiO_2}}}\right)^2 \sigma^2_{\mathrm{SiO_2}} + \left(\frac{\partial \hat{C}_{\mathrm{tot}}}{\partial d_{\mathrm{PC}}}\right)^2 \sigma^2_{\mathrm{PC}}} = \frac{1}{\hat{C}_{\mathrm{tot}}} \frac{\sqrt{\epsilon^2_{\mathrm{PC}} \sigma^2_{d_{\mathrm{SiO_2}}} + \epsilon^2_{\mathrm{SiO_2}} \sigma^2_{d_{\mathrm{PC}}}}}{(\epsilon_{\mathrm{PC}} \cdot d_{\mathrm{SiO_2}} + \epsilon_{\mathrm{SiO_2}} \cdot d_{\mathrm{PC}})} \tag{3.4}$$

where $\sigma_{\mathrm{SiO_2}}$ and σ_{PC} are the standard deviations associated to the thicknesses of the SiO_2 and Parylene C layers.

3.5.2 Characterisation of the Kelvin probe setup

In order to test the correctness of the response of the Kelvin probe, a linearity test was executed by measuring the surface potential of a copper plate whose potential was kept at constant known values by the DC power supply. The line expected for a linear response should have a slope of 1.

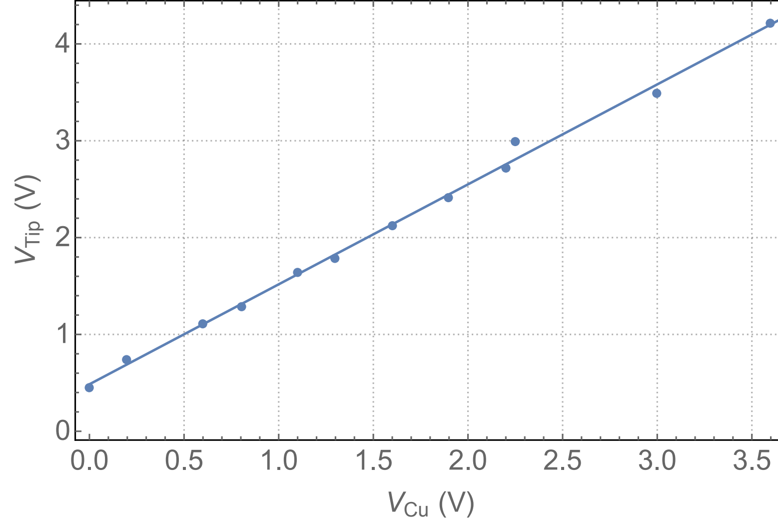

Figure 3.11: Test of the linearity of the response of the Kelvin probe.

The result of a linear interpolation of the data (fig. 3.11) is

$$V_{probe} = (1.00 \pm 0.01) \cdot V_{Cu} + (0.50 \pm 0.02)$$

The slope is well within one standard deviation from the expected value, therefore the device responds correctly to external stimuli.

In an earlier work by the same group, further characterisation of the device was made. It was found that the parasitic coupling of the probe was small enough to allow measurements when:

$$\frac{d}{a} < 6$$

where d is the mean distance between probe and sample, and a is the amplitude of the probe oscillation [32]. Since this condition was fulfilled in this experiment, we can assume parasitic coupling to be negligible.

3.5.3 Characterisation of the MIS capacitors

For each MIS capacitor sample, the best-fabricated device on each sample was examined in detail. Each complete measurement consisted in five measurements at increasing distance from the top electrode, which was expressed as the distance between the rim of the electrode and the centre of the probe. This distance was

increased by steps of 2mm between each run. Since the distance between the rim of the electrode and the scratch encasing the semiconductor was in the order of 15 mm and since the probe is 3 mm wide, in order to avoid distortions due to boundary effects or the influence of the electrode [32], the measurements were taken at distances of 4 mm, 6 mm, 8 mm, 10 mm and 12 mm from the contact.

Before applying an external bias, the contact potential difference between the sample and the probe was measured, which would then be subtracted from the registered surface potential, thus yielding only the transient effects due to the bias. This contact potential difference is given by the difference between work functions of the sample and the probe, and it is constant in time.

The biases were chosen in order to always have a positive bias between drain and gate,

$$V_d - V_g \geqslant 0 \tag{3.5}$$

in order to have holes as charge carriers. This choice was made because P3HT has a higher hole mobility than electron mobility, and because the contact between P3HT and gold, one of the metals chosen for the injecting contacts, is ohmic for holes. For all measurements with the Kelvin probe, the gate was grounded, $V_g = 0$V.

Voltage loss

In a previous work it was observed that the surface potential, when applying a constant voltage bias between the gate and the drain, was not constant but decreased when the distance from the top electrode was increased. This meant that the dielectric layer in the samples did not provide loss-tight insulation, which may be due to coating defects in the SiO_2 or parylene layer, or to the penetration of charges through the parylene. It was observed, though, that adding the layer of Parylene C over the SiO_2 reduced the voltage losses by one order of magnitude [32].

Batch	Mean Parylene C thickness (nm)	Voltage loss (V)
1	-	1.64
2	298.0±3.1	0.09
3	264.8±5.5	0.56
4	287.5±2.0	0.03
5	269.7±1.2	0.45
6	300.0±1.9	0.18
7	300.0±1.9	0.20

Table 3.1: Voltage losses measured at a distance of ∼10mm from the injecting contact with a constant external bias of 8V.

In order to measure the voltage loss, the gate was grounded, while the drain was

connected to the DC power supply. With this configuration, the surface potential was measured with the digital multimeter at various distances of the probe from the contact.

This measurement allowed to objectively verify the quality of the sample. Moreover it provided a test of the effects of adding the Parylene C layer over the SiO_2, which contributed significantly to the reduction of voltage losses. The measured voltage losses at a 8V are reported in table 3.1. The effect of the Parylene C layer is to reduce the losses of about an order of magnitude. The high losses in batches 3 and 5 are probably due to fabrication defects. The devices subjected to losses higher than 0.20 V didn't provide reliable results because the model, which will be developed in the next chapter, partially failed to describe their behaviour.

Behaviour under external bias

As in the DC case, the gate of the MIS capacitor was grounded, while a periodic voltage bias was applied to the drain by the function generator. For each bias, the surface potential was measured with the oscilloscope at increasing distances from the contact. The data was gathered and saved by the digital oscilloscope.

The frequency of the signal generated by the function generator was set at 0.01 Hz, which resulted in a period of 107s (0.009Hz), where the 7 second increase was caused by the insufficient frequency resolution of the function generator.

One channel of the oscilloscope was connected to the *CPD* output of the Kelvin control module, while the other measured the bias applied to the sample directly from the function generator (fig. 3.12).

For each batch, the measurement was repeated for multiple values of V_0 and setting $V_0 = V_1$ (where V_0 and V_1 are, respectively, the AC amplitude and the DC offset of the generic bias defined in eq. (3.1)), in order to compare the behaviour of the devices for different applied biases.

3.5.4 Characterisation of the Transistors

For the transistor samples, output and transfer I/V characteristics were measured. The data gathered with the latter measurement would then be used to extract the charge carrier mobility of the P3HT layer and thus compare the mobilities obtained in the *on*-state of the transistors and the lateral mobility obtained with the MIS capacitor samples.

In fig. 3.13a and 3.13b an example measurement run is shown. For both output and transfer characteristics, three voltage return sweeps were executed, respectively varying the drain voltage V_d or the gate voltage V_g at a rate of $0.2\mathrm{Vs}^{-1}$ between about 0V to 80V and back. For the output sweeps V_g was set at the constant values of -20V, -40V and -60V, while for the transfer sweeps V_d was set at the constant values of -40V, -50V and -60V. During both kinds of measurement the voltage of the source contact V_s was kept at 0V. Each sweep was executed both

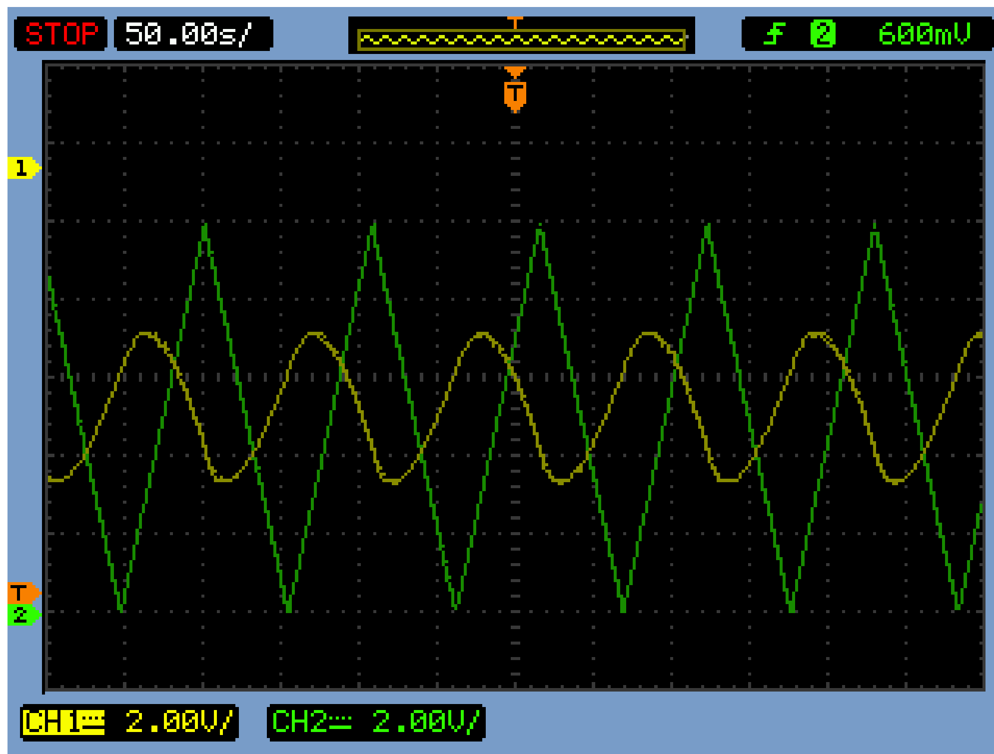

Figure 3.12: Example of the data gathered by the oscilloscope. Green line: applied bias measured directly from the function generator. Yellow line: *CPD* output. Since the *CPD* output gives the difference between the sample's surface potential and the reference potential of the probe, in order to have the actual surface potential the *CPD* output has to be multiplied by -1

for increasing and for decreasing values of V_g or V_d, in order to verify the absence of hysteresis.

The blue lines in fig. 3.13a and 3.13b show the measured drain current I_d, while the red line shows the gate current I_g, which is a loss current and should always remain at $\sim 10^{-10}$A in order for the transistor to work properly.

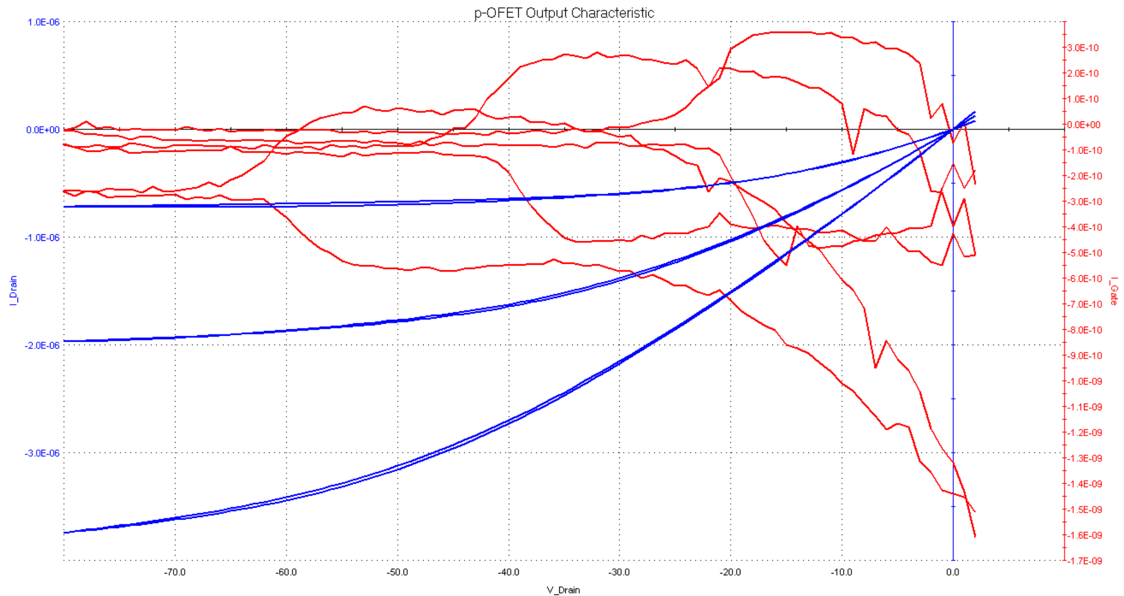

(a) Example of output characteristics recorded with the FET probe station.

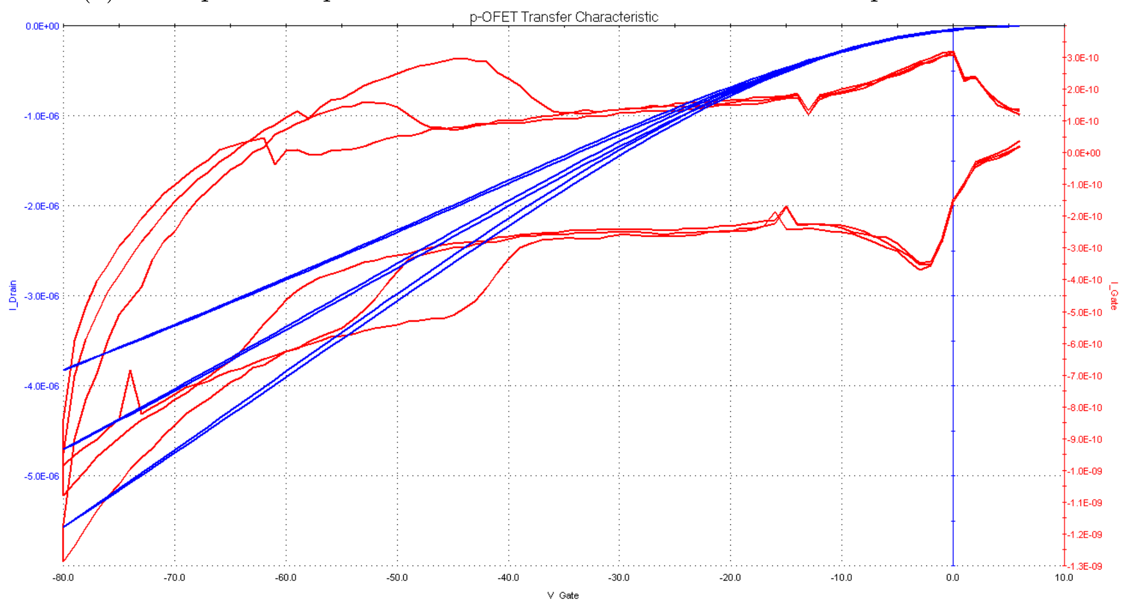

(b) Example of transfer characteristics recorded with the FET probe station. Slight hysteresis is present.

Figure 3.13: Example of data gathered with the FET probe station. The unit for the x-axes are Volt, the one for the y-axes is Ampere. In both cases the blue lines represent the measured drain current I_d, while the red line represents the gate current I_g, which is a loss current and should always remain at $\sim 10^{-10}$A in order for the transistor to work properly.

Chapter 4

Analysis of Experimental Results

4.1 Analysis of MIS capacitors

The MIS capacitors were subjected to measurement with the setup explained in the previous chapter. The applied bias was chosen to be oscillating at positive values, so as to always have a positive voltage difference between the two electrodes, and it was composed of a DC offset and an AC oscillating contribution.

$$\underbrace{V_1}_{\text{DC}} + \underbrace{f(t, V_0)}_{\text{AC}}$$

These contributions were applied so that the applied voltage would vanish whenever $f(t, V_0) \equiv f(t)$ reached a minimum, by choosing the amplitude V_0 of the oscillating part equal to the constant offset.

$$V_0 = V_1$$

After the application of the bias, the surface potential of the MIS capacitor was recorded with the Kelvin probe at multiple, increasing distances from the top contact (fig. 4.1) in order to study the wave of charge carriers injected into and ejected from the organic layer.

Using the minima of $f(t)$ as trigger, a complete set of data gathered from the oscilloscope at fixed V_0 presented itself as in fig. 4.2. The labels of the various sets refer to the distance between the edge of the top contact and the centre of the measuring tip. The comparison between the measured applied bias and the surface potential evolution suggests that, inside the organic layer, the signal changes shape: it is dampened and subjected to a phase shift, thus qualitatively it can be said that the lower the mobility, the bigger the deviation of the signal from the applied bias is. In order to provide a quantitative estimate for the mobility, a model is needed to describe our system, which will be developed by drawing inspiration from a 1969 contribution by Burns describing the transmission of signals inside the semiconducting layer in MOSFETs.

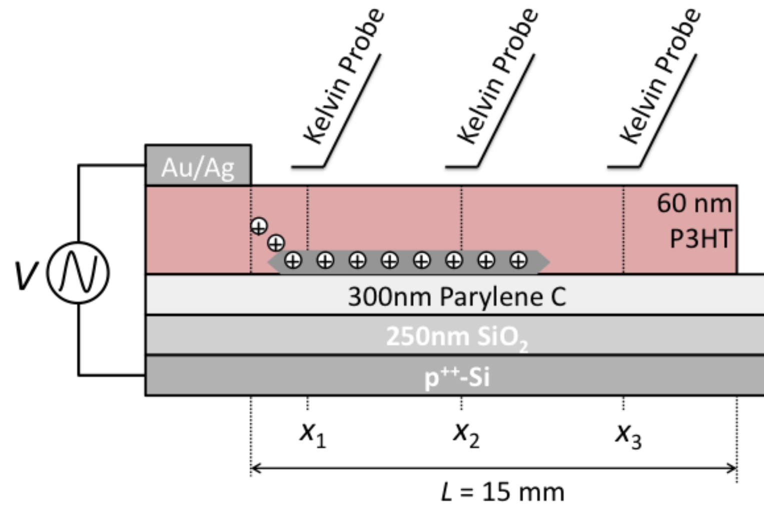

Figure 4.1: Sketch of the vertical layout of the MIS capacitor and the Kelvin probe during measurements. The surface potential was recorded at increasing distances from the top contact in order to record the movement of charge carriers inside the organic layer under a periodic bias.

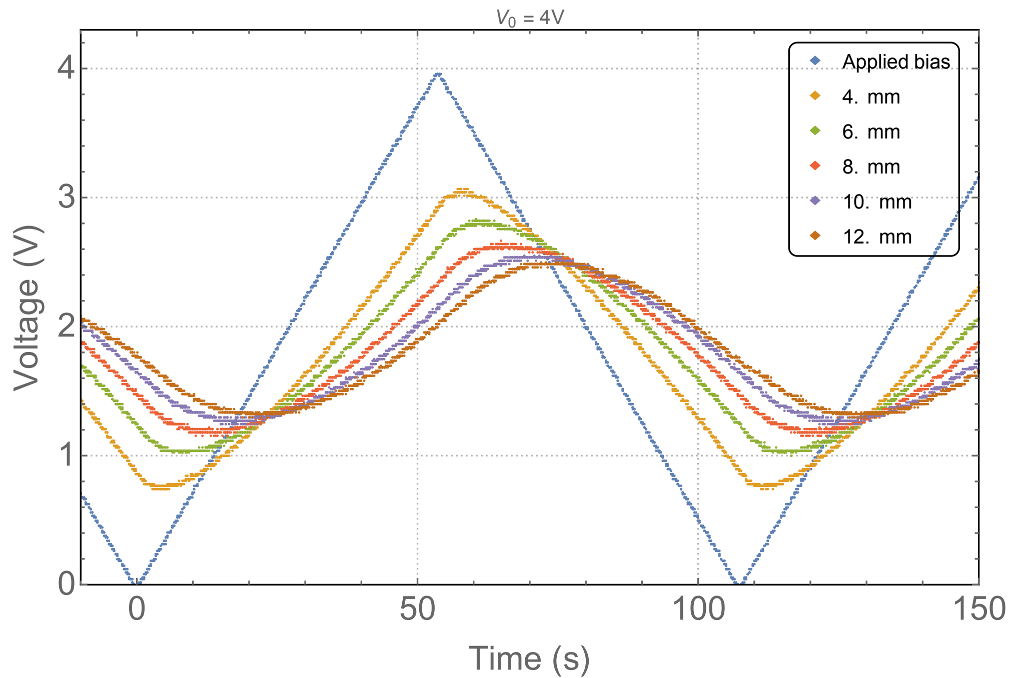

Figure 4.2: Example of a complete set of data gathered with the oscilloscope for the time and spatial evolution of the surface potential, at an applied bias amplitude $V_0 = 4\text{V}$.

4.1.1 Transit-Time Effects in an Organic Thin Film

When the electronic processes inside a field-effect transistor are considered, one finds that the front wave of charges entering the channel can be modelled by a series of resistors and capacitors (fig. 4.3). The resistors represent the penetration of charges within the semiconducting layer and the capacitors model the accumulation of charges in the channel. This system can therefore be described by the transmission line equations, or telegrapher's equations, when an external bias is applied, making an analogy between the surface-potential change in our device and the potential drop on the line. Since, in this model, we only need one charge-injecting electrode, the MOSFET can be approximated to a diode by neglecting the source electrode.

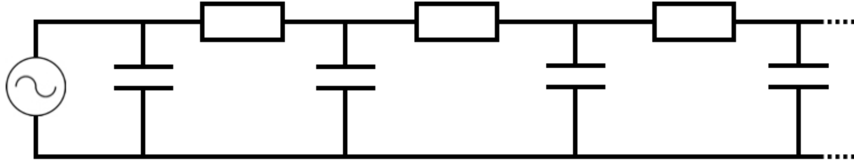

Figure 4.3: Transmission line schematics.

Let us consider an applied bias between the drain contact and the grounded gate, modelled as a bias between the two parallel lines of the transmission line, made of an oscillating AC bias $f(t)$ of frequency ω and amplitude V_0 and a DC offset $V_1 = V_0$.

According to the transmission line equations, the surface potential at a distance x away from the contact is given by [28]:

$$\frac{\partial\psi(t,x)}{\partial t} = \frac{\mu}{2}\frac{\partial^2\psi(t,x)^2}{\partial x^2} \tag{4.1}$$

In all generality, it can be assumed that the surface potential is given by the sum of a constant offset and an oscillating potential.

$$\psi(t,x) = \underbrace{\phi_0}_{\text{DC}} + \underbrace{v(t,x)}_{\text{AC}} \tag{4.2}$$

With this assumption, we linearize eq. (4.1) and execute a Fourier transform on it. We consider Dirichlet and Neumann boundary conditions, respectively at the contact and at the end of the organic layer,

$$\tilde{v}(\omega,0) = \tilde{f}(\omega) \tag{4.3}$$

$$\left.\frac{\partial\tilde{v}(\omega,\hat{x})}{\partial\hat{x}}\right|_{\hat{x}=1} = 0 \tag{4.4}$$

where $\tilde{v}(\omega, x)$ and $\tilde{f}(\omega)$ are, respectively the Fourier transform of $v(t, x)$ and the AC part of the external bias $f(t)$, and $\hat{x} = x/L$. The first boundary conditions says that the AC response of the device at the contact is equal to the AC stimulus, while the second reflects the fact that the electric field at the furthest boundary from the contact vanishes.

With these conditions, one obtains the differential equation governing the behaviour of the oscillating part of the surface potential.

$$i\omega\tau \cdot \tilde{v}(\omega, \hat{x}) = \frac{\partial^2 \tilde{v}(\omega, \hat{x})}{\partial \hat{x}^2} \tag{4.5}$$

This is a linear differential equation, which is much more easily solvable than eq. (4.1). In eq. (4.5) we have introduced the time constant τ, which is given by

$$\tau = \frac{L^2}{\mu \cdot \phi_0} \tag{4.6}$$

Response Function of the Sample

From eq. (4.5), if the form of the applied bias is known, it is possible to find the response function of the device χ, which is defined as

$$\tilde{v}(\omega, \hat{x}) = \chi(\omega, \hat{x}) \tilde{f}(\omega) \tag{4.7}$$

The response function is an intrinsic characteristic of the device and is independent of the bias applied and can thus be used to predict the response of the system under any kind of applied bias. By solving eq. (4.5), one finds that the response function of a generic device that can be modelled with the transmission line equations under AC-stimuli is

$$\chi(\omega, \hat{x}) = \frac{\cos\left(\frac{1-i}{\sqrt{2}}\sqrt{\omega\tau}(1-\hat{x})\right)}{\cos\left(\frac{1-i}{\sqrt{2}}\sqrt{\omega\tau}\right)} \tag{4.8}$$

The complex terms in this equation predicts that the device will not only respond to a stimulus by modifying the amplitude of the signal, but also its phase, which can be studied by noticing that, when $\omega\tau > 1$, eq. (4.8) reduces to

$$\chi(\omega, \hat{x}) \simeq \exp\left(-(1+i)\sqrt{\frac{\omega\tau}{2}}\,\hat{x}\right) \tag{4.9}$$

which gives informations about the phase shift.

Creating a graph of these two functions (fig. 4.4), we can observe that the response of the device is therefore severely dampened both when one moves away from the injecting electrode and when the term $\omega\tau$ shifts from the DC value of 0, which means that the response would be maximized by low frequency stimuli.

The detailed calculations for this section are in Appendix A.

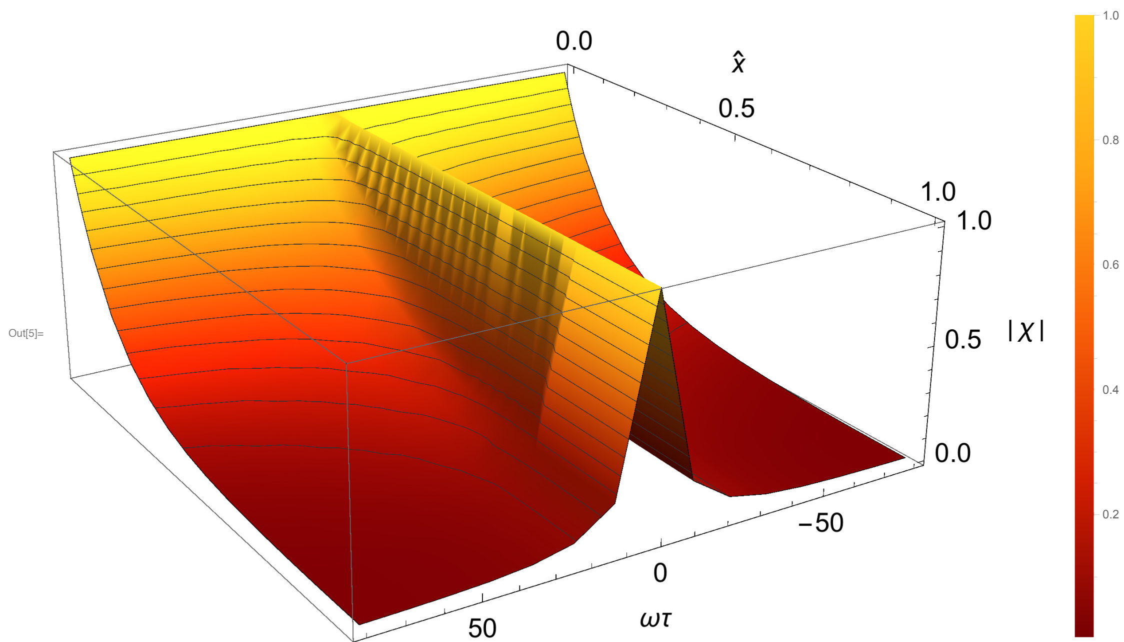

(a) Amplitude of $|\chi|$ as a function of the distance from the electrode $\hat{x}$ and $\omega\tau$. The amplitude of the response is maximum for a DC or very low frequency signal.

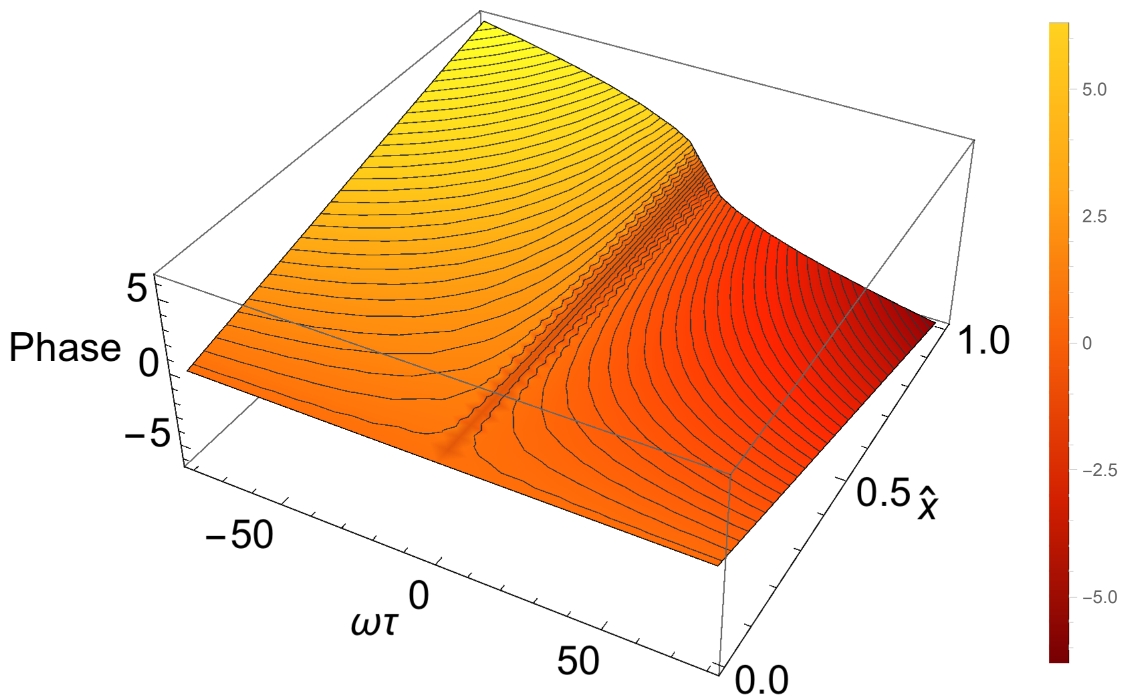

(b) Phase of χ as approximated in eq. (4.9). The maximum response around $\omega\tau = 0$ is evident from the phase-shift pattern, too.

Figure 4.4: Characteristics of the response function $|\chi|$.

4.1.2 Theoretical Description of the Charging of a MIS capacitor under a Periodic Bias

As we discussed in paragraph 4.1.1, the response function to an external oscillating stimulus for a device approximated to a transmission line is given by eq. (4.8). By inserting this in eq. (4.7), one can predict how the surface potential will evolve at various distances from the contact under the influence of a generic bias. Both these equations, though, are defined in the frequency domain: after choosing the suitable AC function $f(t)$ to describe the oscillating part of the bias and after finding its expression $\tilde{f}(\omega)$ in the frequency domain, it will therefore be necessary to execute an inverse Fourier transform to the result of eq. (4.7) in order to find the evolution of the system in the time domain.

The results will then be fitted to the acquired data in order to verify the accuracy of the model and to extract pivotal informations about the semiconducting layer.

The detailed calculations for this section are in Appendix B.

4.1.3 Harmonic Function

Since eq. (4.7) is defined in the frequency domain, the simplest periodic bias that can be taken into account is a sinusoidal wave because it has only one frequency. We can consider, for example, the function:

$$f(t) = V_0 \cos(\omega_0 t) \tag{4.10}$$

With this expression for the bias, its Fourier transform is:

$$\tilde{f}(\omega) = \frac{V_0}{2}(\delta(\omega - \omega_0) + \delta(\omega + \omega_0)) \tag{4.11}$$

which, by boundary condition (4.3), is equal to $\tilde{v}(\omega, 0)$.

We find that eq. (4.7) in the frequency domain is given, in this case, by

$$\tilde{v}(\omega, \hat{x}) = \frac{V_0}{2} \cdot \frac{\cos\left(\frac{1-i}{\sqrt{2}}\sqrt{\omega\tau}(1-\hat{x})\right)}{\cos\left(\frac{1-i}{\sqrt{2}}\sqrt{\omega\tau}\right)}(\delta(\omega - \omega_0) + \delta(\omega + \omega_0)) \tag{4.12}$$

In order to return to the time domain, we need to execute an inverse Fourier transform. If we define $\hat{t} = {}^{\tau}/_{t}$ and $\Omega = \omega_0\tau$, where τ is defined in eq. (4.6), this operation yields:

$$v(\hat{t}, \hat{x}) = \frac{V_0}{\cos\left(\sqrt{2\Omega}\right) + \cosh\left(\sqrt{2\Omega}\right)} \cdot$$
$$\cdot \left\{ \cos\left(\Omega\hat{t}\right) \left(\cos\left((\hat{x}-2)\sqrt{\frac{\Omega}{2}} \right) \cosh\left(\hat{x}\sqrt{\frac{\Omega}{2}} \right) + \cos\left(\hat{x}\sqrt{\frac{\Omega}{2}} \right) \cosh\left((\hat{x}-2)\sqrt{\frac{\Omega}{2}} \right) \right) + \right.$$
$$\left. - \sin\left(\Omega\hat{t}\right) \left(\sin\left((\hat{x}-2)\sqrt{\frac{\Omega}{2}} \right) \sinh\left(\hat{x}\sqrt{\frac{\Omega}{2}} \right) + \sin\left(\hat{x}\sqrt{\frac{\Omega}{2}} \right) \sinh\left((\hat{x}-2)\sqrt{\frac{\Omega}{2}} \right) \right) \right\} \tag{4.13}$$

4.1.4 Chainsaw Tooth Function

As seen in the previous paragraph, the Fourier transform of an harmonic function is an easy operation but this kind of function doesn't provide a clear separation point between the injection and ejection phases of the experiment. Thus, in order to be able to see this difference clearly and in order to create an analogy with the experiment described in paragraph 2.3.2 and this work, it was chosen to work with a bias described by a chainsaw tooth function, or triangular function, whose fundamental oscillation is given by

$$f(t) = V_0 \cdot \left(1 - \frac{2t}{T}\,\mathrm{sgn}(t) \right) \tag{4.14}$$

where $2T$ is the period of the oscillation. Since $f(t)$ increases linearly with time, this implies that the voltage, and thus the electric field, between the contacts are also linear in time, which in turn imply that the density of charge carriers and the injection current are linear in time, too.

The Fourier series of eq. (4.14) is given by the following expression:

$$f(t) = \sum_{n=-\infty}^{\infty} C_n e^{in\omega_0 t} = \sum_{n=-\infty}^{\infty} \frac{4V_0}{\pi^2(2n-1)^2} e^{i(2n-1)\omega_0 t} \tag{4.15}$$

where $2T$ is the period of the bias and $\omega_0 = \pi \cdot T^{-1}$. Because of the presence of sharp angles where the function is not differentiable, the Fourier series has an infinite number of terms.

In order to find the surface potential, we need to find its Fourier series and combine it with eq. (4.7), the surface potential oscillations are given by

$$v(t, \hat{x}) = \sum_{n=-\infty}^{\infty} \tilde{v}(\omega_n, \hat{x})\, e^{i\omega_n t} = \sum_{n=-\infty}^{\infty} \chi(\omega_n, x) \cdot C_n\, e^{i\omega_n t} =$$
$$\sum_{\substack{n=-\infty \\ n \text{ odd}}}^{\infty} \frac{4V_0}{\pi^2 n^2} \frac{\cos\left(\frac{1-i}{\sqrt{2}} \sqrt{\frac{n\pi\tau}{T}} (1-\hat{x}) \right)}{\cos\left(\frac{1-i}{\sqrt{2}} \sqrt{\frac{n\pi\tau}{T}} \right)} e^{i\frac{n\pi}{T}t} \tag{4.16}$$

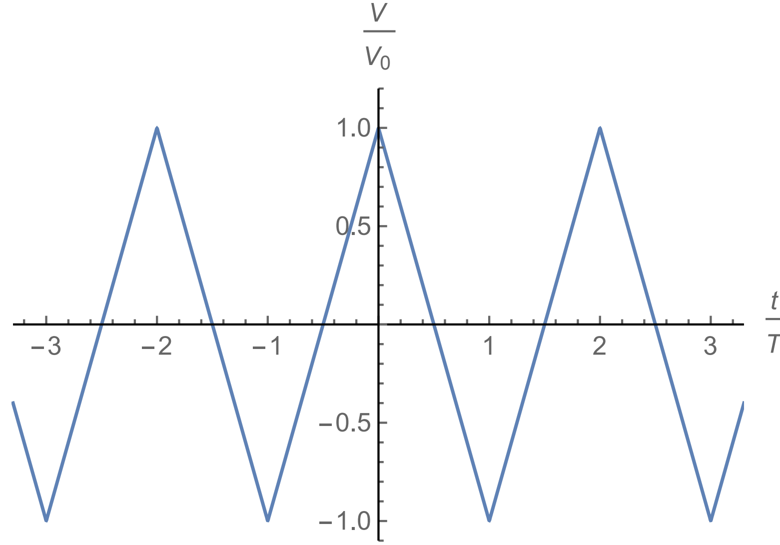

Figure 4.5: Normalised chainsaw tooth, or triangle, function, given by repetitions of the fundamental oscillation (4.14): $f(t + n \cdot 2T), n \in \mathbb{Z}$.

where $\omega_n = n \cdot \omega_0$. In this expression, by remembering the definition of ω_0, we have eliminated the frequency dependence. The calculation yields:

$$\begin{aligned} v(t,\hat{x}) = \sum_{\substack{n=1 \\ n \text{ odd}}}^{\infty} \frac{4V_0}{\pi^2 n^2} \frac{1}{\cosh(\sqrt{2n\pi\tau_0}) + \cos(\sqrt{2n\pi\tau_0})} \cdot \\ \cdot \Bigg\{ \cos\left(\frac{n\pi}{T}t\right) \Bigg[\cosh\left(\sqrt{\frac{n\pi\tau_0}{2}}\hat{x}\right) \cos\left(\sqrt{\frac{n\pi\tau_0}{2}}(\hat{x}-2)\right) + \\ + \cos\left(\sqrt{\frac{n\pi\tau_0}{2}}\hat{x}\right) \cosh\left(\sqrt{\frac{n\pi\tau_0}{2}}(\hat{x}-2)\right) \Bigg] + \\ - \sin\left(\frac{n\pi}{T}t\right) \Bigg[\sinh\left(\sqrt{\frac{n\pi\tau_0}{2}}\hat{x}\right) \sin\left(\sqrt{\frac{n\pi\tau_0}{2}}(\hat{x}-2)\right) + \\ + \sin\left(\sqrt{\frac{n\pi\tau_0}{2}}\hat{x}\right) \sinh\left(\sqrt{\frac{n\pi\tau_0}{2}}(\hat{x}-2)\right) \Bigg] \Bigg\} \end{aligned} \tag{4.17}$$

where the quantities $t_0 = {}^t/_T$ and $\tau_0 = {}^\tau/_T$ were defined.

In order to proceed with the analysis, this infinite sum was truncated at n=20, which provided accurate analysis results while optimising the computation time.

4.2 Analysis

The data gathered from the oscilloscope was saved in three-columned files, that were:

1. the time elapsed from the beginning of the measurement;

2. the signal from the function generator, which was used as bias applied to the sample;

3. the signal from the *CPD* output of the Kelvin control module, that represented the contact potential difference between the sample and the Kelvin probe tip.

Before the analysis could take place, the raw data had to be processed. Firstly, the time axis was shifted so that, for each measurement with fixed $V_1 = V_0$, all subsets of data gathered at increasing distances from the contact were triggered at a minimum of $f(t)$.

Secondly, the surface potential of the sample was extrapolated from the *CPD* signal by subtracting the contact potential difference that had been measured before applying the external bias. The result of this operation was then inverted in sign in order to have the actual surface potential of the sample, since the *CPD* signal gave instead the difference between the sample's surface potential and the reference potential of the probe.

Lastly, a data matrix was created with all subsets of a single measurement with fixed $V_1 = V_0$.

The processed data could then be analysed by a script written with the analysis program Mathematica.

Disclaimer on the Determination of Errors to the Data

The determination of experimental errors in measurements obtained from organic semiconductors is not an easy matter. The uncertainty in the results is given by the extreme difficulty to produce two samples that are exactly the same and by the natural degradation that the organic semiconductor after synthesis. Moreover, slight changes in the atmospheric conditions under which the measurement is taken may lead to significantly different results. Because of this huge variability, in literature results are often given only as an order of magnitude[4, 5].

Reported values of hole mobility for P3HT, in general, range from $\sim 10^{-5}$ to $\sim 10^{-1}\text{cm}^2\text{V}^{-1}\text{s}^{-1}$, depending on the amorphousness of the obtained film and the regioregularity of the employed polymer[5]. Considering only measurements executed at room temperature on spin-coated P3HT, the uncertainty decreases, with literature-reported values of $\mu \sim 10^{-3}\text{cm}^2\text{V}^{-1}\text{s}^{-1}$[13, 15].

The errors assigned to the data presented in this chapter, therefore, are only a statistical result of the data gathering and analysis, and do not reflect the actual variations of hole mobility in spin-coated P3HT measured at room temperature.

4.2.1 Fitting the Data

The processed data was fitted using the appropriate $v(t, \hat{x})$. The fitting procedure was executed at the same time on all the runs that constituted a single measurement and it involved five parameters:

- the half period of the signal T for the chainsaw bias, or the fundamental oscillation ω_0 for the harmonic bias;
- the constant offset voltage ϕ_0;
- the parameter V_0 in $v(t, \hat{x})$, which corresponds to the amplitude of the applied oscillating bias $f(t)$;
- the time constant characteristic to the device τ;
- the phase-shift with respect to the DAQ trigger, since data was triggered at a minimum of the applied bias but the model was constructed assuming a maximum in $t = 0$s.

from which an estimate for the mobility could be inferred by inserting the values given by the fit in (4.6).

Disruptive effects of traps and losses.

The ϕ_0 and V_0 were extrapolated from the fit of the data gathered away from the contact in order to find the effective external voltage felt by the device, which could be different from the bias we applied at the contact because of the presence of losses or long-lived trapped charges. The comparison between the extrapolation of the effective bias felt by the device with the actual bias measured directly from the function generator provided us with a qualitative estimate for the goodness of our device and, in most samples, allowed us to ignore the contributions of losses or trapped charges.

Both the presence of traps and that of losses could have a serious influence on the data, hindering the analysis process and modifying the effective applied bias felt by the device.

The expected effect of traps would be to increase the residual charge inside the organic layer, which would increase the value of the DC surface potential offset ϕ_0, which without the presence of traps would be equal to $V_1 = V_0$. Since the surface potential cannot reach higher voltages than the ones applied, this would mean also a dampening in the amplitude of $v(t, \hat{x})$ and therefore a lower value of V_0.

The effect of losses, instead, would have the inverse effect on the offset ϕ_0 and decrease its value. This would also mean a dampening in the amplitude of $v(t, \hat{x})$.

The combined effect of traps and losses would be expected to leave the offset more or less at the same voltage, but dampen the estimate for V_0. As hinted in paragraph 3.5.3, the model didn't work well on batches 3, 5 and especially 1

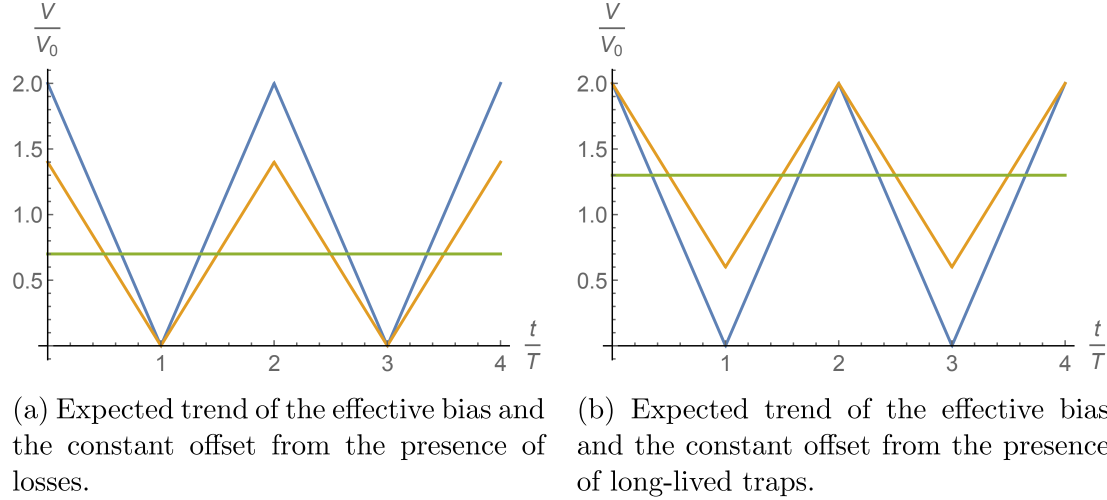

(a) Expected trend of the effective bias and the constant offset from the presence of losses.

(b) Expected trend of the effective bias and the constant offset from the presence of long-lived traps.

Figure 4.6: Expected trends of the effective bias felt by the device in the presence of losses or traps (yellow line), compared to the actual applied bias (blue line). In both cases, the constant offset felt by the device (green line) would shift from the applied DC offset of 1.0.

because of the too high voltage losses along the devices, which led to the partial failure of the fitting procedure.

The influence of high losses is clearly visible in the data gathered for batch 1: in fig. 4.7, the effect described in fig. 4.6a is clearly visible, with a dampening of the signal. Moreover, the measured value for V_0 decreases from 4.38V at a distance from the top contact of 4 mm, already 0.62V lower than the applied value of 5V, to 4.16V at a distance of 12 mm: this means that the effect of traps, in comparison to that of losses, is negligible.

This effect is even more clearly visible when the data are fitted to the model (fig. 4.7): the effective applied bias extrapolated from the model reproduces exactly the trend hypothesised in fig. 4.6a.

The data for batches 3 and 5 reproduce, in smaller measure, the problems that afflict the batch 1 data.

4.2.2 Chaisaw fit results

Each of the samples was subjected to multiple measurements with increasing $V_1 = V_0$. For all of the batches, the highest applied voltages were reached with the applied bias with $V_1 = V_0 = 5$V, which was used to compare the devices. The results of the fits are in table 4.1, where the trigger phase-shift and the half period T, which in all cases was successfully found to be $\sim$ 53s by the fit, were not reported because they are not relevant for the analysis of the devices.

The errors on the parameters were the ones extracted from the fit combined

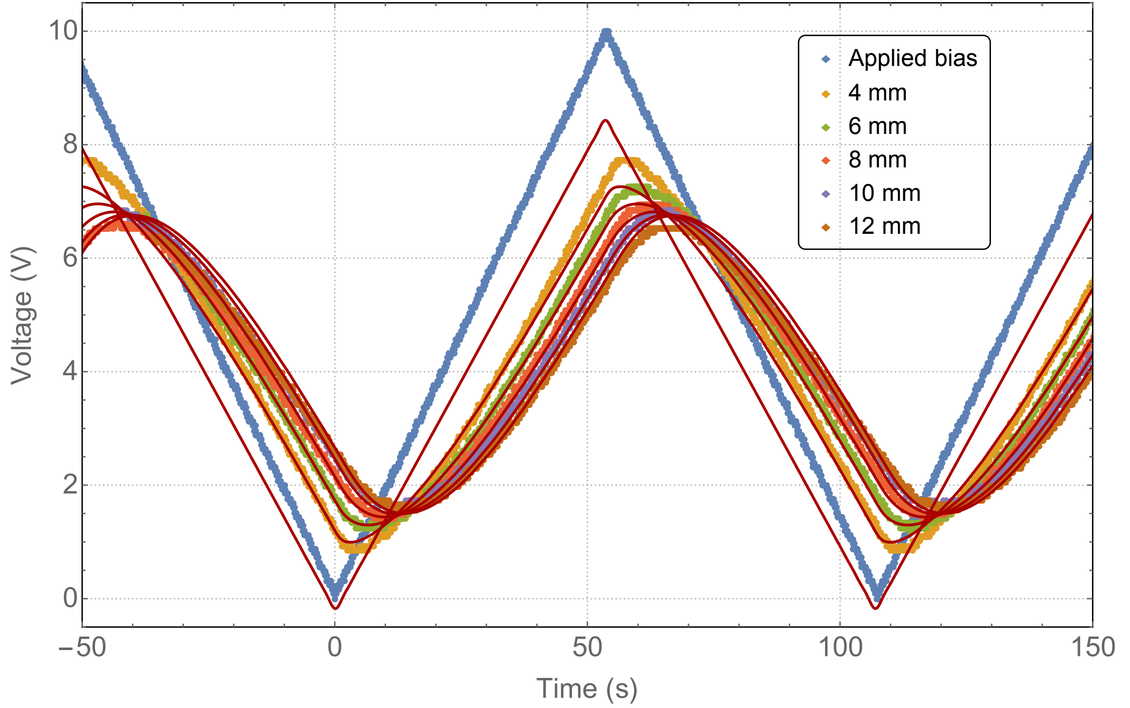

Figure 4.7: Attempt at analysis for batch 1 data, unreliable because of the influence of high losses. Blue dots: applied bias measured directly from the function generator. Otherwise coloured dots: data gathered with the Kelvin probe at increasing distances from the injecting contact. Red lines: fitted model. Because of the high losses of the device, the effective applied bias calculated from the fit doesn't match the actual applied bias.

with the measurement error given by the oscilloscope through error propagation.

The effect of the losses discussed in paragraph 4.2.1 can be seen in the predicted values of ϕ_0 which only for batches 1, 3 and 5 has smaller values than the applied value $V_1 = 5$V. Meanwhile, the values for V_0 were all within 2σ from the applied value of 5V.

The values of τ can't be directly compared between different batches, since, due to the fabrication procedure, there are small variations in the order of 0.5mm in the length of the channel of each device.

Examples of fitted data (batches 2 and 4) can be seen in fig. 4.8. In both cases the extrapolated shape of the effective applied bias coincides almost exactly with the actual applied bias. The imprecise reproduction of the shape in fig. 4.8a is due to the difficulty of finding the exact alignment between edge of the top contact and centre of the Kelvin probe, leading to a systematic error of the order of 0.1mm in the determination of the distance between probe and top contact.

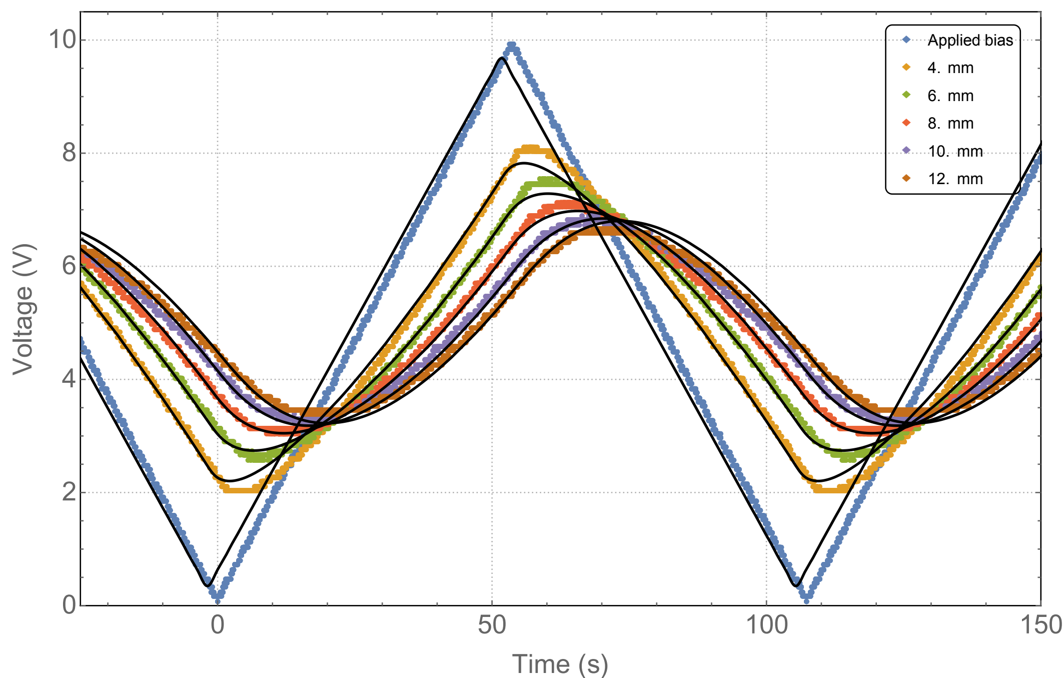

(a) Batch 2, gold top contact, $V_0 = 5$V.

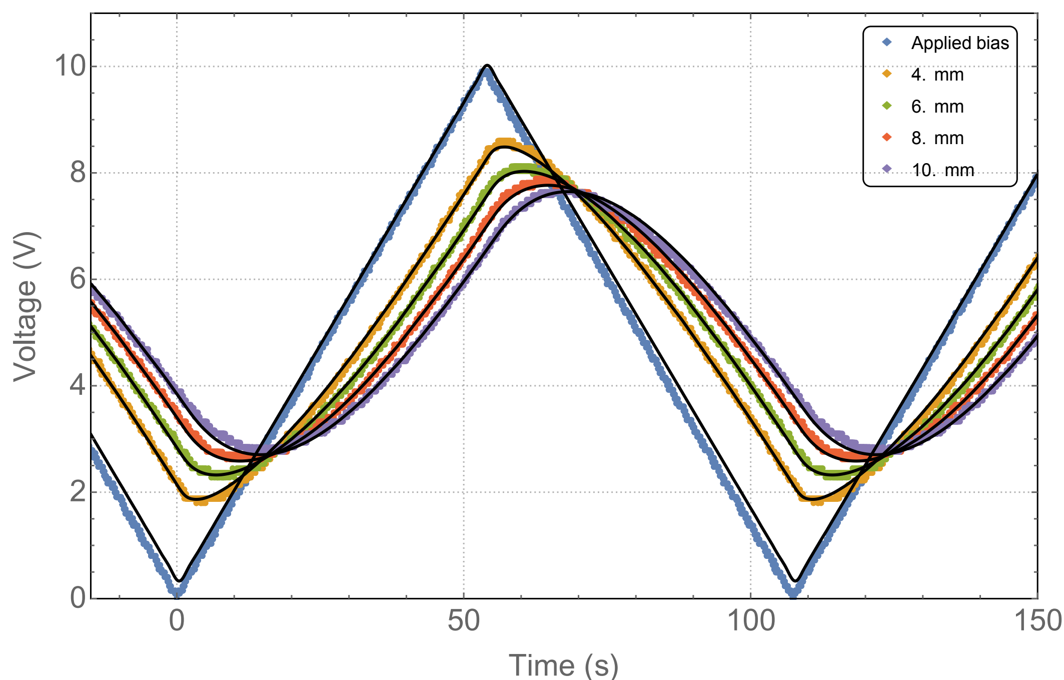

(b) Batch 4, silver top contact, $V_0 = 5$V.

Figure 4.8: Examples of fitted functions for batch 2 and batch 4 for amplitude $V_0 = 5$V. Blue dots: applied bias measured directly from the function generator; otherwise coloured dots: data gathered with the Kelvin probe at increasing distances from the contact; black lines: fitted model. In both cases, the extrapolated applied bias, which is the effective voltage bias felt by the organic film, reproduces very well the actual applied bias.

Batch	V_1 (V)	ϕ_0 (V)	τ (s)
1	4.34 ± 0.15	4.13 ± 0.15	39.16 ± 1.20
2	4.71 ± 0.15	5.02 ± 0.16	76.71 ± 1.20
3	4.77 ± 0.15	4.71 ± 0.15	56.56 ± 3.01
4	4.89 ± 0.16	5.18 ± 0.16	54.36 ± 1.20
5	5.07 ± 0.16	4.84 ± 0.15	78.31 ± 1.20
6	5.00 ± 0.16	5.21 ± 0.16	46.16 ± 1.20
7	4.92 ± 0.16	5.13 ± 0.16	22.10 ± 1.20

Table 4.1: Fit results for the $V_1 = V_0 = 5$V measurements.

4.2.3 Mobility calculation

From the time constant τ provided by the fit, it was possible to calculate the mobility for the P3HT using eq. (4.6).

$$\mu = \frac{L^2}{\tau \phi_0} \tag{4.18}$$

By repeating the analysis for each sample[1] with multiple bias amplitudes V_0, it was found that for all batches the estimates of μ decreased with increasing ϕ_0, that is with increasing charge carrier densities (fig. 4.9a). This is an unusual behaviour for the mobility, contrary to what is usually reported in literature: μ has been mostly observed to follow a positive trend with the increase of the charge carrier density[11, 15] (fig. 4.9b).

In order to understand this unexpected behaviour, some considerations about the samples and their fabrication procedure must be made.

As mentioned above, the presence of oxygen doping in P3HT is known to change the electrical properties of the organic semiconductor. Oxygen contamination was reduced as much as possible during sample fabrication, but some exposure to air was unavoidable while preparing the samples for the CVD deposition of the encapsulating Parylene C layer.

Moreover, the thick encasing layer of Parylene C deposited on the finished samples does indeed provide protection from oxygen and humidity infiltration to the semiconducting layer, but it is nonetheless permeable to gasses: this characteristics in some cases has a positive influence on experiments, such as when the samples left in a nitrogen-filled glovebox are able to outgas the oxygen infiltrated in the organic layer[30], but negative in others: in the case of our diodes, the measurements forced the samples to remain in air for hours.

Finally, the trap states are present at the interface between the SiO_2 and the organic layer, too. It has been shown that these traps can be passivated by de-

[1]The analysis for the MIS capacitor of batch 1 was interrupted here because the purpose in its construction was to verify results obtained in previous works by the same research group.

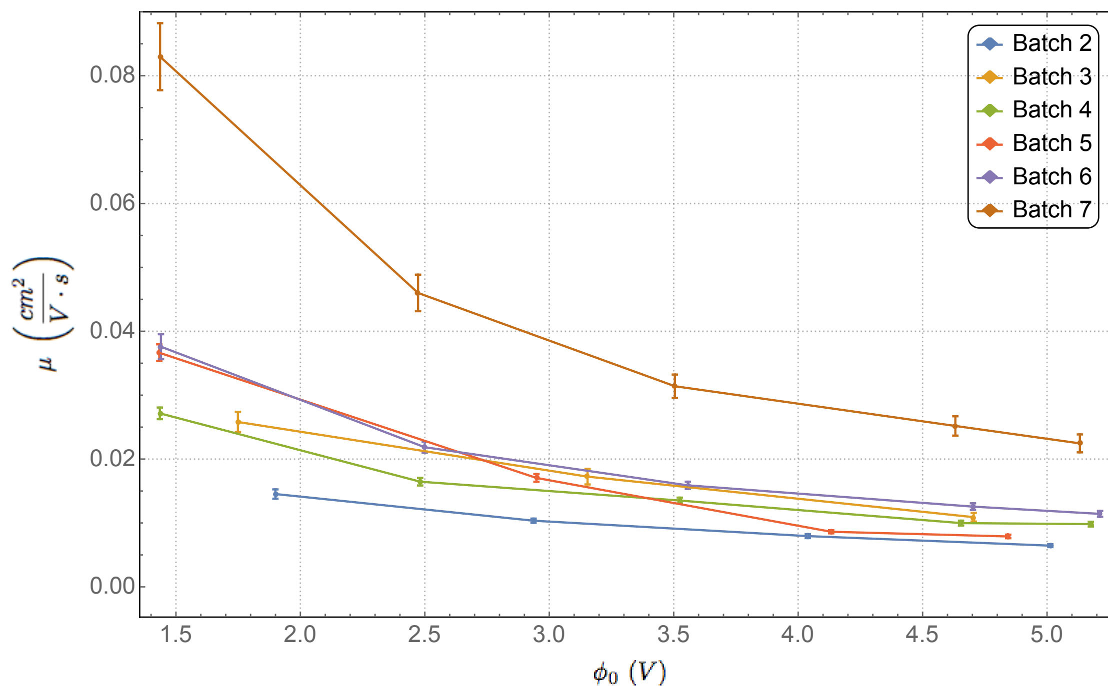

(a) Trend of charge carrier mobility extracted from the series of measurements executed with multiple bias amplitudes V_0. The x-coordinate assigned to each measurement is the effective applied bias ϕ_0 calculated from the fit, which is proportional to the charge carrier density.

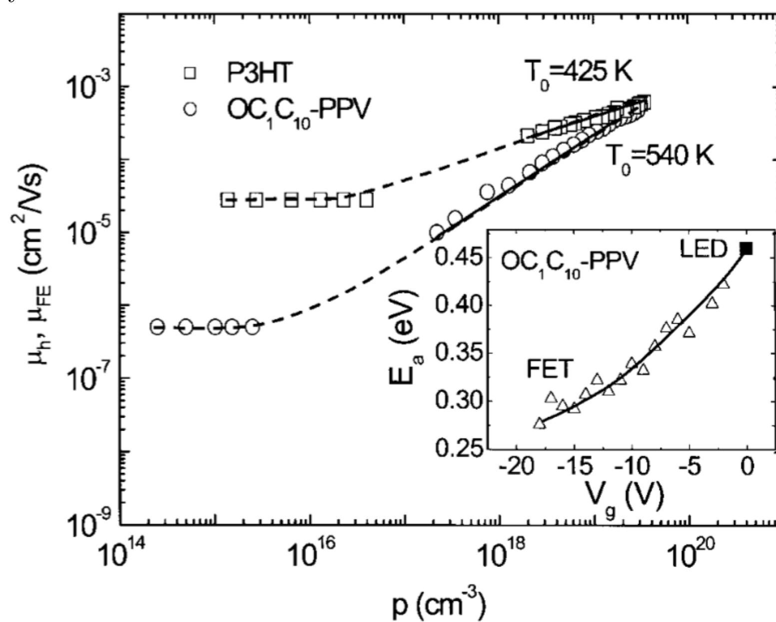

(b) Example of the literature-known dependance of the mobility μ on the charge carrier density p.

Figure 4.9: Trends of μ extrapolated from the Kelvin probe measurements and literature-known. The x-axes of the two figures are proportional to one another since the effective applied bias is proportional to the charge carrier density p.

position of a Parylene C layer, which, though, allows a slow seepage of charges anyway, which in turn can fill the trap states of the SiO_2[16].

In fact, negative dependence of the mobility on the applied electric field has been reported in literature for conjugated polymers in general[12, 15] and P3HT in particular[13, 14], and it was usually attributed to spatial disorder or to the presence of dopant molecules. By taking into consideration the fabrication process of the samples and the measurement procedure, the latter explanation seems the most probable.

These considerations hinted at the necessity to correct the first estimates for the mobility considering the contribution of doping charges to the transient electronic processes. The description of the devices made with the transmission line equations was updated so that the current included the contribution qN_l, where q is the elementary charge and N_l is the linear density of doping charges (calculations made in paragraph A.2.1).

This procedure allowed to arrive to a new definition of the transient time τ_{tr}, introduced in eq. (4.6), as a function of the time constant extracted from the fit τ_m. From this, we arrive at the following expression, where the only unknown terms are the areal density of charge carriers $\hat{N}$ and the mobility μ.

$$\frac{L^2}{\phi_0 \cdot \tau_m} = \mu \left(1 + \frac{q\hat{N}}{\hat{C}} \frac{1}{\phi_0} \right) \tag{4.19}$$

The value of $\hat{C}$ is the areal capacitance of the insulating layer of the MIS capacitors and is found combining the capacitances of SiO_2 and parylene C, whose thicknesses and dielectric constants are known (table 3.1).

Batch	$\hat{C}$ $(F \cdot m^{-2})$
1	$(1.38 \pm 0.07) \cdot 10^{-4}$
2	$(5.58 \pm 0.11) \cdot 10^{-5}$
3	$(5.97 \pm 0.15) \cdot 10^{-5}$
4	$(5.70 \pm 0.12) \cdot 10^{-5}$
5	$(5.91 \pm 0.13) \cdot 10^{-5}$
6	$(5.55 \pm 0.24) \cdot 10^{-5}$
7	$(5.55 \pm 0.24) \cdot 10^{-5}$

Table 4.2: Areal capacitance of the insulating layer of the MIS capacitors.

The unknown values $\hat{N}$ and μ were found executing the linear fit $a \cdot x + b$ of eq. (4.19) on the data reported in fig. 4.9a, by using ϕ_0^{-1} as ordinate and $L^2 \cdot \phi_0^{-1}\tau^{-1}$ as abscissa (fig. 4.10). The statistical errors were assigned using error propagation on the errors given by the fitting procedure (tab. 4.3).

Naming σ_a and σ_b the standard deviations on the slope and intercept, respectively, of the line extracted from the fit, the following expressions give the desired

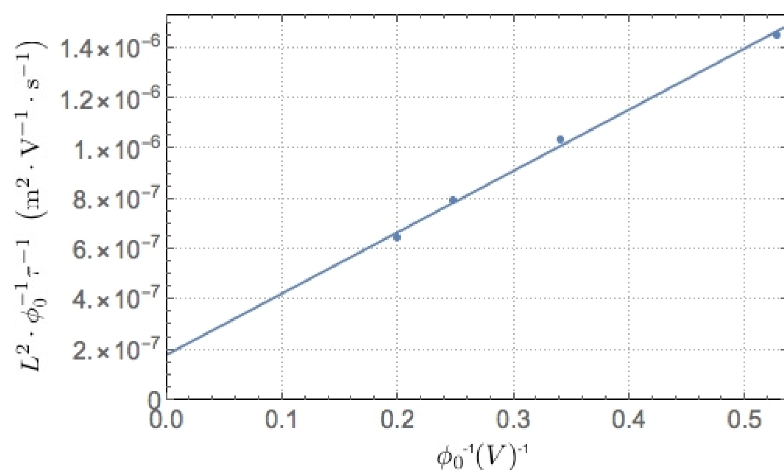

(a) Batch 2, Au top contact.

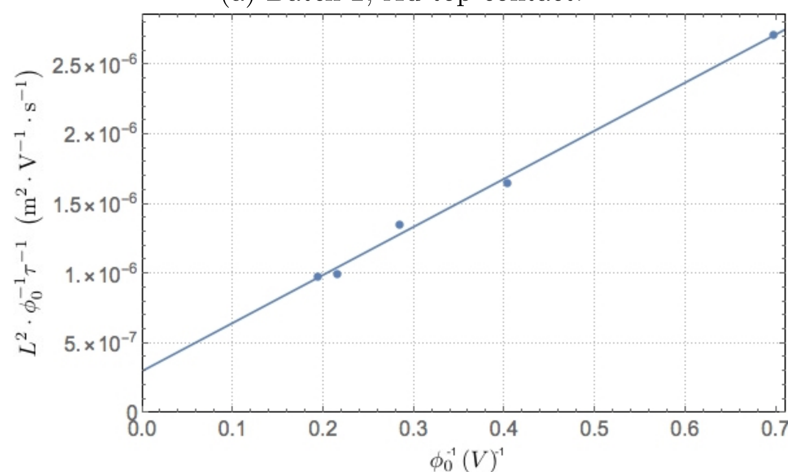

(b) Batch 4, Ag top contact.

Figure 4.10: Examples of the linear fit of eq. (4.19), both for Au (batch 2) and Ag (batch 4) top contacts. For each batch, all mobilities calculated with different V_0 with eq. (4.18) were used to find a single value for μ, given by the intercept of the fitted line.

values and connected statistical errors.

$$\mu = b \tag{4.20}$$

$$\sigma_\mu = \sigma_b \tag{4.21}$$

$$\hat{N} = \frac{\hat{C} a}{b \cdot q} \tag{4.22}$$

$$\sigma_{\hat{N}} = \hat{N} \sqrt{\left(\frac{\sigma_a}{a}\right)^2 + \left(\frac{\sigma_b}{b}\right)^2 + \left(\frac{\sigma_{\hat{C}}}{\hat{C}}\right)^2} \tag{4.23}$$

Batch	μ $\left(\mathrm{cm}^2 \cdot \mathrm{V}^{-1} \cdot \mathrm{s}^{-1}\right)$	$\hat{N}$ (cm^{-2})
2	$(1.81 \pm 0.36) \cdot 10^{-3}$	$(4.70 \pm 0.96) \cdot 10^{11}$
3	$(3.30 \pm 2.42) \cdot 10^{-3}$	$(4.52 \pm 3.38) \cdot 10^{11}$
4	$(3.02 \pm 0.55) \cdot 10^{-3}$	$(4.07 \pm 0.76) \cdot 10^{11}$
6	$(2.35 \pm 0.16) \cdot 10^{-3}$	$(5.49 \pm 0.44) \cdot 10^{11}$
7	$(1.72 \pm 1.07) \cdot 10^{-3}$	$(1.47 \pm 0.92) \cdot 10^{12}$

Table 4.3: Results obtained by processing the linear fit of (4.19).

In general, these values for mobility and areal dopant density $\hat{N}$ in good accord with literature-known measurements of analogous devices, where values of $\mu \sim 10^3 \mathrm{cm}^2 \cdot \mathrm{V}^{-1} \cdot \mathrm{s}^{-1}$ and $\hat{N} \simeq 4 \cdot 10^{11}$ cm^{-2} have been reported[15, 30].

Batches 6 and 7 were accidentally left for hours in air before the protective Parylene C encapsulation layer was deposited. The measurements on these samples were therefore executed after leaving the samples in storage for two weeks inside the nitrogen-filled glovebox, in order to allow the outgassing of the excess oxygen through the Parylene C. The batch 6 sample seems to have successfully outgassed the dopant oxygen, acquiring values for $\hat{N}$ similar to those of the other batches. The same cannot be said for the batch 7 sample, which has an estimate for $\hat{N}$ that is two to three times higher than the values found for the other samples and in literature, but the estimate for μ is in accord with literature and the other estimates.

As it has already been hinted, the analysis for batches 3 and 5 would not be reliable because of the relatively high voltage leakage. This led to higher statistical errors for batch 3, while the results found for batch 5 are not reported because they are inconsistent.

By taking the weighted mean of the values in tab. 4.3, a value of the mobility for spin-coated regioregular P3HT examined under ambient conditions can be given for gold and silver injecting electrodes.

$$\mu_{\mathrm{Au}} = (2.26 \pm 0.15) \cdot 10^{-3} \ \mathrm{cm}^2 \cdot \mathrm{V}^{-1} \cdot \mathrm{s}^{-1}$$
$$\mu_{\mathrm{Ag}} = (2.75 \pm 0.49) \cdot 10^{-3} \ \mathrm{cm}^2 \cdot \mathrm{V}^{-1} \cdot \mathrm{s}^{-1}$$

Both these values are in good accord with the literature values of $\sim 10^{-3} \mathrm{cm}^2 \cdot \mathrm{V}^{-1} \cdot \mathrm{s}^{-1}$, which means that the model developed for lateral transport inside the organic layer of a MIS capacitor is successful in predicting the mobility for spin-coated regioregular P3HT.

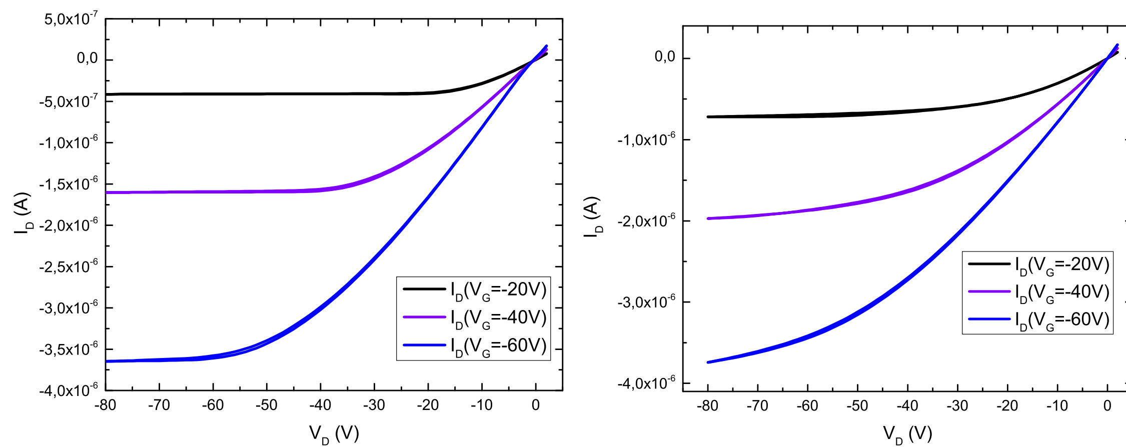

(a) Output characteristics.

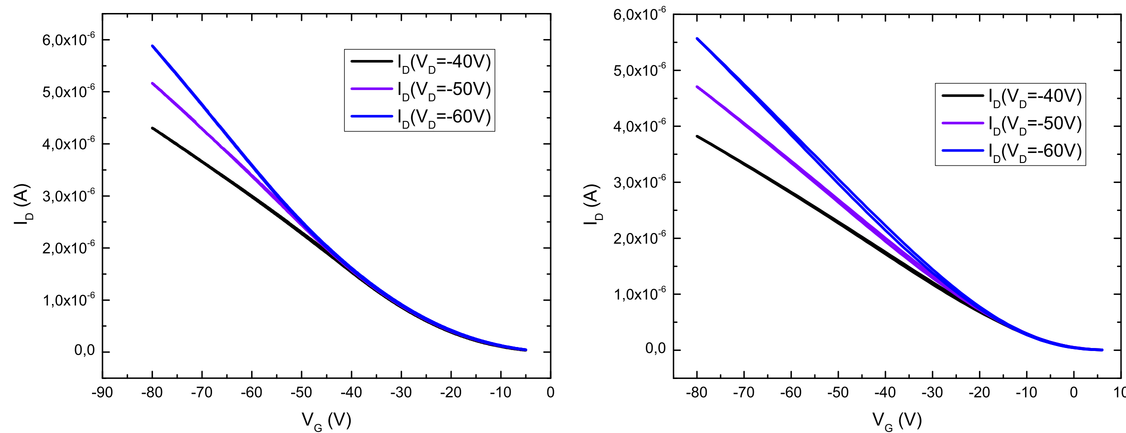

(b) Transfer characteristics. The saturation regime is present at low values of V_g, where the curves coincide.

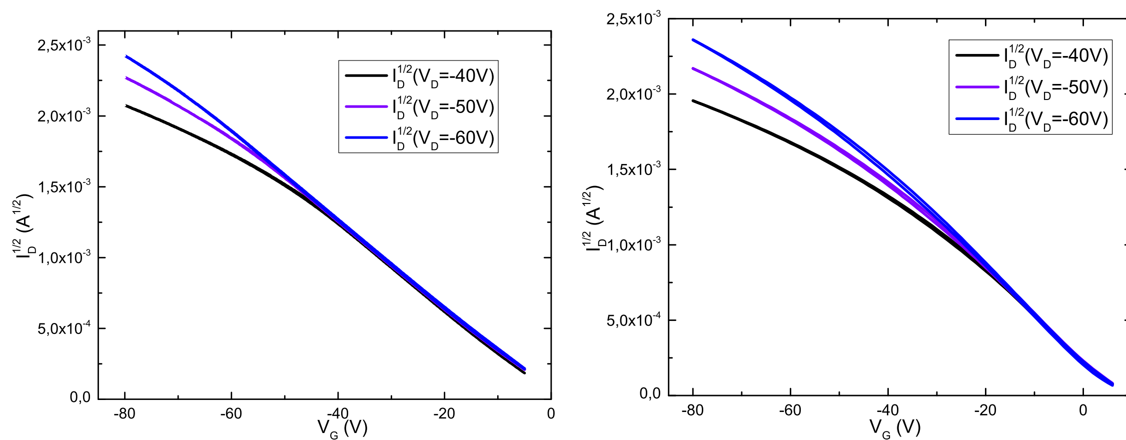

(c) Modified transfer characteristics for the extraction of mobility. By plotting $\sqrt{I_d}$, the saturation regime is clearly visible as the linear part of the curves.

Figure 4.11: Examples of transistor data gathered with the FET probe, both for Au (batch 6, right side) and Ag (batch 4, left side) top contacts.

4.3 FET Probe Station Data

4.3.1 Extraction of μ from Transistor Transfer Characteristics

The output characteristics were measured by executing three voltage sweeps on the voltage of the drain V_d from about 0 to -80V while the gate voltage V_g was set at the constant values of -20V, -40V and -60V. Likewise, the transfer characteristics were measured by executing three voltage sweeps on V_g by setting V_d to -40V, -50V and -60V. During both measurements the voltage of the source contact V_s was kept at 0V.

Each sweep was executed both for increasing and for decreasing values of V_g or V_d, in order to verify the absence of hysteresis. The transistor, samples built simultaneously with the MIS capacitor samples, work as expected, with good transfer and output characteristics (fig. 4.11).

As test of the correctness of the of the analysis on the MIS capacitor samples, the charge carrier mobility was extracted from the transistors' transfer I/V characteristics using eq. (4.24).

The expectation, since the voltages reached with the transistor samples are almost one order of magnitude higher than the ones reached by the diode samples, is that this method would provide a higher estimate for the mobility than the one found with the MIS capacitor samples.[11].

Extraction of the mobility

By observing eq. (2.6), it can be noticed that the drain current in the saturation regime $|V_d| \geqslant |V_g|$ depends only on V_g, not V_d.

$$\sqrt{I_d} = \sqrt{\frac{\hat{C}W}{2L}} \sqrt{\mu}(V_g - V_{th}) \tag{4.24}$$

Therefore, by executing a simple linear fit on the transfer characteristics graph, modified so as to have axes $\left(V_g,\ I_d^{1/2}\right)$, it is possible to extract the mobility μ and the threshold voltage V_{th} of the device.

From the slope m of the fitted line, an for the mobility can be found, using the formula:

$$\mu = m^2 \frac{2L}{\hat{C}W} \tag{4.25}$$

$$\sigma_\mu = \frac{2L}{\hat{C}W} \cdot \sqrt{m^2 \left(4 \cdot \sigma_m^2 + \frac{m^2}{\hat{C}^2} \sigma_{\hat{C}}^2\right)} \tag{4.26}$$

From the intercept q of the fitted line, an estimate for the threshold voltage can be found, using the formula:

$$V_{th} = -\frac{m}{q} \tag{4.27}$$

$$\sigma_{V_{th}} = \sqrt{\frac{1}{m^2} \cdot \left(\sigma_m^2 \left(\frac{m}{q} \right)^2 + \sigma_q^2 \right)} \tag{4.28}$$

The σ_m and σ_q are given by the linear fit and are the standard deviation.

For each set of transfer characteristics data with $V_d = (-40\text{V}, -50\text{V}, -60\text{V})$, the zone of each curve for which $V_d \ll V_g$ was identified (fig. 4.11c). Since, for each sweep, each V_g value was measured twice, it was possible to linearly fit each curve twice, once with increasing and once with decreasing values of V_g, thus obtaining six straight lines for each set of measurements.

Since each measurement consisted on three voltage sweeps executed for increasing and decreasing values of V_g, the linear fit could be executed six times for each transistor, yielding six estimates for the mobility and the threshold voltage. A weighted mean was executed on the parameters extracted from each transistor, yielding the results in table 4.4. As for the MIS capacitor, the results for batch 5 were not reported because they are inconsistent.

Batch	μ $\left(\text{cm}^2 \cdot \text{V}^{-1} \cdot \text{s}^{-1}\right)$	V_{th} (V)
1	$(1.81 \pm 0.01) \cdot 10^{-3}$	45.54 ± 0.03
2	$(1.18 \pm 0.01) \cdot 10^{-3}$	30.36 ± 0.05
3	$(2.68 \pm 0.03) \cdot 10^{-3}$	43.32 ± 0.02
4	$(4.23 \pm 0.04) \cdot 10^{-3}$	0.46 ± 0.01
6	$(1.28 \pm 0.03) \cdot 10^{-2}$	6.69 ± 0.01
7	$(7.13 \pm 0.07) \cdot 10^{-3}$	5.26 ± 0.02

Table 4.4: Results from the analysis on the data gathered from OFETs.

Again, the reader is reminded that the errors are so small because they are only statistical errors that can't take into account the sample variability given by fabrication and handling.

Some batches have very high values of V_{th}, which should be around ~3V. This is probably due to initiating the first sweep at values higher than 0V: it has been reported in literature that executing voltage sweeps on an organic semiconductor may lead to the capture of charge carriers by trap-levels created by the presence of oxygen doping, which leads to a shift in V_{th}[30]. It is possible that the same happened here, with the samples having some residual doping and being accidentally illuminated during measurements.

The influence of the accidental higher doping on batches 6 and 7 is visible in the mobility estimate: μ increases with doping, thus batches 6 and 7 have higher values of μ than the other samples.

The weighted mean of the values in tab. 4.4 can be calculated for gold and silver top electrodes (excluding batch 1 because of its too high losses).

$$\mu_{\mathrm{Au}} = (1.34 \pm 0.01) \cdot 10^{-3}\ \mathrm{cm}^2 \cdot \mathrm{V}^{-1} \cdot \mathrm{s}^{-1} \tag{4.29}$$

$$\mu_{\mathrm{Ag}} = (4.94 \pm 0.03) \cdot 10^{-3}\ \mathrm{cm}^2 \cdot \mathrm{V}^{-1} \cdot \mathrm{s}^{-1} \tag{4.30}$$

These results are in good accord with literature values of these values are in good accord with the literature values for spin-coated regioregular P3HT of $\mu \sim 10^{-3}\mathrm{cm}^2\mathrm{V}^{-1}\mathrm{s}^{-1}$. As was the case with the MIS capacitors, there are no relevant differences between the silver and gold contacts visible.

The mobility values are similar to those found for the MIS capacitors, even though the applied voltages are one order of magnitude higher. The reason is that the charge carrier bias is proportional to $V - V_{th}$.

The voltage threshold for the MIS capacitors can be found with the formula

$$e \cdot \frac{\hat{N}}{\hat{C}} \tag{4.31}$$

which for our transistors yields threshold voltages between -11V and -16V for batches 2, 3, 4 and 6 and ~-42V for batch 7 because of the high doping.

This means that the effective bias for the MIS and the transistors was in the same order of magnitude of ~10V, thus the charge carrier density, proportional to $V - V_{th}$, was of the same order of magnitude in both cases. This is why the mobility results are so similar.

4.4 Comparison Between Ag and Au Electrodes

As we have seen, the mobilities calculated for MIS capacitors with the silver and gold contacts were of the same order of magnitude as the one expected from literature and they were in good accord with the one extracted from transistor samples, even though the applied fields were one order of magnitude higher in the latter case. Moreover, the extrapolated applied bias reproduced very well the actual bias applied to the MIS capacitors, irrespective of the injecting contact material.

This might seem odd, since the comparisons between the Fermi levels of silver and gold with the molecular orbitals of P3HT predict the following: the Ag-P3HT contact should create a Schottky barrier for hole injection into the organic semiconductor of about 0.8eV, while this barrier should be absent or negligible for hole injection into the organic semiconductor at the contact Au-P3HT.

Therefore, the current injected from gold, being injected from an ohmic contact, is limited only by the ability of the organic bulk to transport charges and it can be used to study the mobility.

The same cannot be said for the current injected from silver: as a rule of thumb, *injection limited* (IL) current in polymers with mobilities comparable with that of P3HT may arise when the Schottky barrier is higher than 0.3 - 0.4 eV[4].

Since it cannot be ruled out *a priori* that the current injected from the Ag electrode be an IL current, some considerations must be made about what influences this kind of current would have on the measurements.

Since the presence of the Schottky barrier limits injection but not ejection of charges, the IL current would lead to asymmetric I/V characteristics. What would be seen from the Kelvin probe measurements with a IL current would therefore be a drop of the DC offset ϕ_0, an increase in the time constant τ and a drop of the AC amplitude V_0. If the barrier and the current were too large, the potential bias might even be deformed entering the channel and thus the model developed for MIS capacitors would fail, since the shape of the effective applied bias would be unknown.

This, though, as we have seen, is not what happens: the model describes very well the response of the MIS capacitors, also of those with an Ag contact, and neither the AC amplitude V_0 nor the DC offset ϕ_0 are significantly modified by injection.

The reason is the extremely low injection currents due to the very low frequency of the bias applied, which allows time for the charges to overcome the Schottky barrier.

The current flowing in the MIS capacitor per unit width is given by (manipulating eq. (A.10)):

$$I_W = \hat{C}L\frac{1}{\tau}\frac{\partial v(t,x)}{\partial \hat{x}} \tag{4.32}$$

For an applied harmonic bias of frequency ω and amplitude V_0, and in the limit $\omega\tau \gg 1$, the current flowing at the contact per unit width is given by:

$$I_W = \hat{C}L\sqrt{\frac{\omega}{\tau}}V_0 \tag{4.33}$$

For the samples in this work, where $\hat{C} \sim 5 \cdot 10^{-5}\ \mathrm{F} \cdot \mathrm{m}^{-1}$, $V \sim 5\mathrm{V}$, $L \sim 15\mathrm{mm}$, $\tau \sim 50\mathrm{s}$ (tab. 4.1), $\omega = \frac{2\pi}{T} = \frac{2\pi}{107\mathrm{s}} \sim 2\pi \cdot 0.01\mathrm{Hz}$, we obtain

$$I_W \sim 10^{-7}\ \mathrm{A} \cdot \mathrm{m}^{-1} \tag{4.34}$$

which is two order of magnitude smaller than the transistor current at the same applied potential ($\sim 10^{-5}\ \mathrm{A} \cdot \mathrm{m}^{-1}$). Low frequency and thus low currents might explain why there is no observable difference between the samples with gold or silver contacts.

4.5 Summary of Results

In this chapter, a model for a generic MIS-like structure was developed, modelling the wave of charge carriers entering the device with the transfer line equations.

The model was applied to the data gathered at various distances from the injecting contact with the Kelvin probe for fixed values of the AC amplitude V_0 of the applied bias, and it allowed extrapolate the effective potential felt by the device through the channel, ensuring that the signal was not warped during injection. From the fitted model, it was possible to extrapolate the time constant τ, from which the mobility μ was calculated using the formula:

$$\mu = \frac{L^2}{\tau \phi_0}$$

Repeating the analysis for measurements with increasing AC amplitudes V_0, a negative dependence of the mobility μ from the effective DC offset ϕ_0 was found. Examining the conditions of fabrication and handling of the devices, and researching literature, the unusual negative dependence was attributed to the presence of doping inside the material. The model was updated taking into account the contribution to the current of doping charges, which led to a new definition of τ:

$$\frac{L^2}{\phi_0 \cdot \tau_m} = \mu \left(1 + \frac{q\hat{N}}{\hat{C}} \frac{1}{\phi_0} \right)$$

For each batch all the results calculated with the previous definition of tau were used to execute a linear fit of this equation, yielding a single value of μ for each sample. This method yielded as a side product also the charge carrier concentration $\hat{N}$.

In order to check the mobility results obtained with the MIS model, the transistor transfer characteristics were analysed in the regime $V_d \ll V_g$. The data gathered in this interval were fitted using the formula

$$\sqrt{I_d} = \sqrt{\frac{\hat{C}W}{2L}} \sqrt{\mu} (V_g - V_{th})$$

This yielded, for each batch, another estimate for the charge carrier mobility of P3HT independent from the MIS model.

For each batch, the current-injecting electrode had been chosen to be either Au or Ag. For each kind of electrode, the results were averaged and are reported in the table below.

	MIS capacitors	Transistors
$\mu_{Au}\left(\mathrm{cm}^2 \cdot \mathrm{V}^{-1} \cdot \mathrm{s}^{-1}\right)$	$(2.26 \pm 0.15) \cdot 10^{-3}$	$(1.34 \pm 0.01) \cdot 10^{-3}$
$\mu_{Ag}\left(\mathrm{cm}^2 \cdot \mathrm{V}^{-1} \cdot \mathrm{s}^{-1}\right)$	$(2.75 \pm 0.49) \cdot 10^{-3}$	$(4.94 \pm 0.03) \cdot 10^{-3}$

We remind the reader that the errors have only statistical significance, since they are extracted from the analysis and cannot take into account the variability given by sample fabrication and handling, and by the natural decay of the semiconductor after synthesis.

The devices behave in the same way with both kinds of electrodes, even though, for hole injection, there is a Schottky barrier between Ag and P3HT while Au creates ohmic contacts with P3HT. The similarity between the two kinds of contacts descends, probably, from the low frequencies used, which allow the charges time to overcome the Schottky barrier.

The estimates for the mobilities are in good accord with literature, where values of $\mu \sim 10^{-3}\mathrm{cm}^2\mathrm{V}^{-1}\mathrm{s}^{-1}$ have been reported, both for transistor and MIS capacitor samples. The model developed in this chapter was therefore successful in predicting the mobility for regioregular P3HT spin-coated samples measured under ambient conditions. Therefore, it provides a new, contactless way to infer the transfer characteristics of P3HT at very low applied currents.

Chapter 5

Conclusions

In this work, a description for transient electronic processes inside MIS capacitors subjected to a periodic bias was developed. It was based on experimental measurements on organic macroscopic devices with an external periodic bias applied examining the surface potential of the channel with a macroscopic Kelvin probe.

Custom samples were built with a channel length of about 15mm based on regioregular poly(3-hexylthiophene-2,5-diyl) (P3HT) and subjected to a very low frequency bias ($\sim$ 0.01Hz). The charges were drawn into the organic layer by capacitive coupling between the top and the bottom contacts, and the wave of charge carriers injected into the organic layer was observed with the Kelvin probe in the steady state at various distances from the injecting contact. The measurements demonstrated that charge carriers inside P3HT are able to spread laterally over distances in the order of centimetres when an electric field is used to inject them inside the organic layer. It was observed that, due to the small velocity of charge carriers, the externally applied bias was dampened and subjected to a phase shift when moving away from the injecting contact.

Based on these observations, a theoretical model for the device was developed describing the wave of charge carriers entering the organic layer of the MIS capacitor with the transfer line equations. Through this description, it was possible to arrive at the response function of de device. Combining the response function with the known shape of the applied bias allowed to successfully predict the time and spatial evolution of the surface potential of the device measured by the Kelvin probe.

The analysis based on the model led to results which are in good accord with literature, with a mobility of $\sim 10^{-3}\text{cm}^2 \cdot \text{V}^{-1} \cdot \text{s}^{-1}$, and allowed to develop a new contactless method for the determination of lateral charge carrier mobility at low currents. This method, being based on the use of a Kelvin probe, allows to study the transfer characteristics of the organic semiconductor without touching the organic layer or interfering with the electronic processes inside the device.

As a side product of the analysis, it was also possible to determine the areal density of dopant molecules present inside the organic semiconducting layer, which

was also in good accord with literature with values of $\sim 10^{11}\text{cm}^{-2}$.

As further verification for our results, transistor samples were built simultaneously with the MIS capacitors with the same vertical layout. After measuring their characteristics and verifying that the transistor worked correctly, an independent estimate for the mobility for P3HT was extracted from the I/V transfer characteristics of the transistors, which confirmed the estimate of $\mu \sim 10^{-3}\text{cm}^2\text{V}^{-1}\text{s}^{-1}$ found with the MIS capacitors.

In order to compare the effects of an ohmic contact against a contact with a significant Schottky barrier, the samples were built either with gold or silver injecting contact. In the end, the mobility measurements showed no differences between the samples with silver or gold injecting contacts either with the transistor samples or the MIS capacitors. Moreover, for MIS capacitors the extrapolated applied bias reproduced very well the actual applied bias, and the transistor characteristics of the devices were similar, irrespective of the injecting contact material. This indifference to the presence of an injection barrier is probably due to the small frequencies used, which allows charge injection through the barrier through tunneling.

Appendix A

Electronic Processes Involved in Charging and Discharging of a Transistor

A.1 Description of a FET with the Telegrapher's equations.

It is known from literature that, under low frequency stimuli, the performance of a MOSFET with a channel of length L and width W can be analysed by modelling the channel as a RC transmission line, where the voltage inside the line is a function of both time and distance[28]. This description can be applied to OFETs because of the analogies they have with MOSFETs.

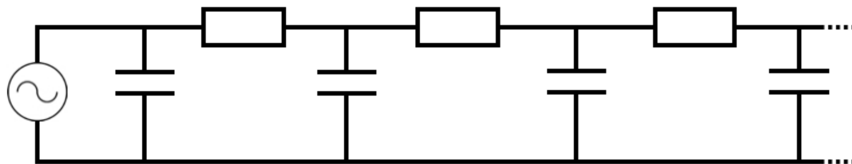

The resistances represent the channel, while the capacitors represent the capacitive coupling between the channel and the gate, which draws the charges in the channel.

In order to set down the telegrapher's equations, that solve the transmission line, we need to consider a Δx portion of channel. Let's consider the lower line as grounded, so that the potential change is limited to the upper line. The resistance and capacitance per unit length Δx are R_l and C_l . There might be a leak in the transmission line, which we indicate with $1/G_l$ where G_l is the conductance, and an inductive coupling L_l between the two lines.

The telegrapher's equations can be easily found by applying Kirchhoff's rules

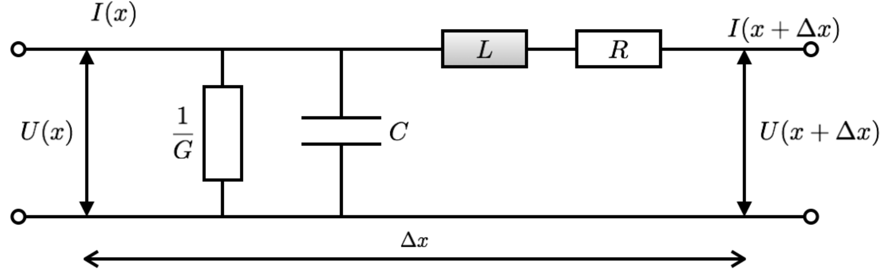

Figure A.1: Transmission line schematics.

to the circuit[33]. By Kirchhoff's second rule, the solution of the line is given by:

$$U(x+\Delta x) - U(x) + R_l \cdot I(x+\Delta x) + L_l \frac{\partial I(x+\Delta x)}{\partial t} = 0 \tag{A.1}$$

If we send $\Delta x \to 0$, we can write:

$$U(x) + \frac{\partial U(x)}{\partial x}\Delta x - U(x) + R_l\left(I(x) + \frac{\partial I(x)}{\partial x}\Delta x\right) + L_l \frac{\partial}{\partial t}\left(I(x) + \frac{\partial I(x)}{\partial x}\Delta x\right) = 0 \tag{A.2}$$

$$\frac{\partial U(x)}{\partial x} + R_l I(x) + \underbrace{R_l \frac{\partial I(x)}{\partial x}\Delta x}_{\xrightarrow{\Delta x \to 0} 0} + L_l \frac{\partial I(x)}{\partial t} + \underbrace{L_l \frac{\partial^2 I(x)}{\partial t \partial x}\Delta x}_{\xrightarrow{\Delta x \to 0} 0} = 0 \tag{A.3}$$

$$\boxed{\frac{\partial U(x)}{\partial x} + R_l I(x) + L_l \frac{\partial I(x)}{\partial t} = 0} \tag{A.4}$$

Similarly, we can use Kirchhoff's first rule to find the second telegrapher's equation.

$$\boxed{\frac{\partial I(x)}{\partial x} = -G_l U(x) - C_l \frac{\partial U(x)}{\partial t}} \tag{A.5}$$

A.1.1 Differential equations for OFETs

If the insulation between the upper and lower line (that is, between the channel and the gate) is made by an electrically tight dielectric, the leak between the two lines is zero and therefore $G = 0$; moreover, since we are working with low-frequency signals, the impedance given by the inductance vanishes, so we assume that $L = 0$. The telegrapher's equations become then:

$$\frac{\partial U(x)}{\partial x} = -R_l I \tag{A.6}$$

$$\frac{\partial I(x)}{\partial x} = -C_l \frac{\partial U(x)}{\partial t} \tag{A.7}$$

Until now, we have considered the lower line as grounded, but, since it corresponds to the OFET gate, in general it will have a potential V_g. Therefore, we set $U = V(x) - V_g$.

$$\frac{\partial}{\partial x}(V(x) - V_g) = \frac{\partial V(x)}{\partial x} = -R_l I$$
$$\frac{\partial I(x)}{\partial x} = -C_l \frac{\partial}{\partial t}(V(x) - V_g) = -C_l \frac{\partial V(x)}{\partial t}$$

In order to eliminate the dependence on R_l, let's consider the conductivity given by the Drude model.

$$R_l^{-1} = e \cdot n\mu \tag{A.8}$$

where μ is the *mobility of charge carriers* along the line, or inside the channel, whose dimensions are $\frac{m^2}{V \cdot s}$. The term $e \cdot n$ is the linear charge density, which can be rewritten as:

$$e \cdot n = \frac{Q}{L} = C_l \ (V_g - V(x)) \tag{A.9}$$

Using equations (A.8) and (A.9), the first telegrapher's equation can be rewritten as:

$$\frac{\partial V(x)}{\partial x} = -\frac{1}{C_l \ \mu(V_g - V(x))} I \qquad \Rightarrow \qquad I = C_l \ \mu(V_g - V(x)) \frac{\partial V(x)}{\partial x}$$

Let us now abandon the transmission line analogy. We can define the surface potential of the OFET as $\psi = -U(x) = -(V(x) - V_g)$.

$$I = C_l \ \mu\psi \frac{\partial \psi(x)}{\partial x} = \frac{C_l \ \mu}{2} \frac{\partial \left(\psi(x)^2\right)}{\partial x} \tag{A.10}$$

Taking the derivative with respect of x of the whole equation (A.10) and using equation (A.7), we have

$$\frac{\partial I(x)}{\partial x} = \frac{\mu C_l}{2} \frac{\partial^2 \psi^2}{\partial x^2} = C_l \ \frac{\partial \psi}{\partial t}$$
$$\Rightarrow \boxed{\frac{\partial \psi}{\partial t} = \frac{\mu}{2} \frac{\partial^2 \psi^2}{\partial x^2}} \tag{A.11}$$

This is the differential equation that characterises the surface potential of the device, which depends *only* on the charge carrier mobility.

A.2 Response of an OFET to an External Bias

From the description of an OFET through a transmission line, we reached the result (A.11) using the telegrapher's equations. Let us consider an OFET with

channel length L channel width W and let's imagine to apply a bias made of an oscillating AC bias $f(t)$ of frequency ω and amplitude V_0 and a DC offset V_1, with $V_0 = V_1$. We can assume that in the steady-state the surface potential will also be given by an oscillating and a constant contribution. The coordinate x is the linear distance from the drain and it can assume values between 0 and L.

$$\psi(t,x) = \underbrace{\phi_0}_{\text{DC}} + \underbrace{v(t,x)}_{\text{AC}} \tag{A.12}$$

The DC contribution is, of course, constant in time and, since we are talking about a steady state, it must also be constant in the whole channel, therefore

$$\frac{\partial \phi_0}{\partial x} = \frac{\partial \phi_0}{\partial t} = 0 \tag{A.13}$$

If the AC contribution is zeroed, eq. (A.11) gives in the steady state:

$$\frac{\partial^2 \phi_0^2}{\partial x^2} = 0 \tag{A.14}$$

We can use this to explicitly calculate eq. (A.11) with the expression of the surface potential (A.12).

$$\frac{\partial \phi_0}{\partial t} + \frac{\partial v(t,x)}{\partial t} = \frac{\mu}{2}\left(\frac{\partial^2 \phi_0^2}{\partial x^2} + 2v(t,x)\frac{\partial^2 \phi_0}{\partial x^2} + 4\frac{\partial \phi_0}{\partial x}\frac{\partial v(t,x)}{\partial x} + 2\phi_0\frac{\partial^2 v(t,x)}{\partial x^2} + \frac{\partial^2 v(t,x)^2}{\partial x^2}\right)$$

If we cancel all the contributions which we know to be zero, we are left with:

$$\frac{\partial v(t,x)}{\partial t} = \mu\phi_0\frac{\partial^2 v(t,x)}{\partial x^2} + \frac{\mu}{2}\frac{\partial^2 v(t,x)^2}{\partial x^2} \tag{A.15}$$

Since we are considering low frequency stimuli, the last term can be neglected and we are left with

$$\frac{\partial v(t,x)}{\partial t} = \mu\phi_0\frac{\partial^2 v(t,x)}{\partial x^2} \tag{A.16}$$

We can solve it in the frequency domain, by replacing $v(t,x)$ with its inverse Fourier transform:

$$v(t,x) = \frac{1}{2\pi}\int_{-\infty}^{+\infty} \tilde{v}(\omega,x)e^{i\omega t}d\omega \tag{A.17}$$

Thus we have

$$\frac{\partial}{\partial t}\frac{1}{2\pi}\int_{-\infty}^{+\infty} \tilde{v}(\omega,x)e^{i\omega t}d\omega = \mu\phi_0\frac{\partial^2}{\partial x^2}\frac{1}{2\pi}\int_{-\infty}^{+\infty} \tilde{v}(\omega,x)e^{i\omega t}d\omega \tag{A.18}$$

We can exchange the derivative with respect to t and the integral in $d\omega$, and, since $\tilde{v}(\omega,x)$ is not dependent on t, we have:

$$\frac{1}{2\pi}\int_{-\infty}^{+\infty} \tilde{v}(\omega,x)(i\omega)e^{i\omega t}d\omega = \mu\phi_0\frac{1}{2\pi}\int_{-\infty}^{+\infty} \frac{\partial^2 \tilde{v}(\omega,x)}{\partial x^2}e^{i\omega t}d\omega \tag{A.19}$$

Because exponentials with different exponents are orthogonal, we arrive to the following equality.

$$i\omega \cdot \tilde{v}(\omega, x) = \mu\phi_0 \frac{\partial^2 \tilde{v}(\omega, x)}{\partial x^2} \tag{A.20}$$

If we replace x with $\hat{x} = \frac{x}{L}$, which runs from 0 to 1, we can define a time constant, a *transient time* characteristic to the device,

$$\tau = \frac{L^2}{\mu \cdot \phi_0} \tag{A.21}$$

which means that:

$$\boxed{i\omega\tau \cdot \tilde{v}(\omega, x) = \frac{\partial^2 \tilde{v}(\omega, x)}{\partial x^2}} \tag{A.22}$$

Finally, we have obtain the desired result, that is a linear differential equation which is much more easily solvable than eq. (A.16), and we can use this to find the response function of the device $\chi(\omega, x)$, defined by:

$$\tilde{v}(\omega, \hat{x}) = \chi(\omega, \hat{x}) f(\omega) \tag{A.23}$$

A.2.1 Contributions of Doping Charges

When we consider the contributions to the surface potential of doping charges inside the channel, we need to add a term to the current to take their presence into account. We do this by adding the term qN_l to eq. (A.9)

$$I = \mu(C_l\ V + qN_l)\frac{\partial V}{\partial x} = \frac{\mu C_l}{2}\frac{\partial (V^2)}{\partial x} + q\mu N_l \frac{\partial V}{\partial x} \tag{A.24}$$

This new term is linear in $\frac{\partial V}{\partial x}$ and thus creates no problem in the following calculations. By following the same procedure as before, one arrives to the new expression for eq. (A.11).

$$\boxed{\frac{\partial \psi}{\partial t} = \frac{\mu}{2}\frac{\partial^2 \psi^2}{\partial x^2} + \frac{qN_l\mu}{C_l}\frac{\partial^2 \psi}{\partial x^2}} \tag{A.25}$$

Again considering the surface potential defined in eq. (A.12), we arrive to the new expression for eq (A.20).

$$i\omega \cdot \tilde{v}(\omega, x) = \left(\frac{\mu\phi_0}{L^2} + \frac{qN_l\mu}{C_l\ L^2}\right)\frac{\partial^2 \tilde{v}(\omega, x)}{\partial \hat{x}^2} \tag{A.26}$$

As we did before, we can define as τ_m^{-1} the factor of $\frac{\partial^2}{\partial \hat{x}^2}\tilde{v}(\omega, x)$, where the subscript m refers to the fact that this is the quantity that we can directly measure.

$$\frac{1}{\tau_m} = \frac{\mu\phi_0}{L^2} + \frac{qN_l\mu}{C_l\ L^2} = \frac{1}{\tau_{\text{tr}}} + \frac{q\hat{N}\mu}{\hat{C}\ L^2} \tag{A.27}$$

where $\hat{N}$ and $\hat{C}$ are, respectively, the charge carrier density per unit area and the capacitance per unit area, and τ_{tr} is the actual transient time characteristic to the device defined in eq. (A.21).

We observe that eq. (A.26) is equivalent to eq. (A.22), the only difference between the two is the definition of the time constant.

In order to extract the charge carrier mobility μ, we manipulate eq. (A.27) to give the following expression corrected for the presence of doping charges.

$$\frac{L^2}{\phi_0 \cdot \tau_m} = \frac{L^2}{\phi_0 \tau_{\text{tr}}} \left(1 + \frac{q\hat{N}}{\hat{C}\phi_0}\right) = \mu \left(1 + \frac{q\hat{N}}{\hat{C}\phi_0}\right) \tag{A.28}$$

A.2.2 Response Function of the device

In order to find the response function of the device, we need to solve eq. (A.22). First of all, we need to explicit the response function. Eq. (A.23) tells us that eq. (A.22) can be rewritten as:

$$\begin{aligned} i\omega\tau \cdot \chi(\omega, \hat{x}) f(\omega) &= \frac{\partial^2(\chi(\omega, \hat{x}) f(\omega))}{\partial \hat{x}^2} = \\ &= f(\omega)\frac{\partial^2 \chi(\omega, \hat{x})}{\partial x^2} + 2\frac{\partial f(\omega)}{\partial x}\frac{\partial \chi(\omega, \hat{x})}{\partial x} + \chi(\omega, \hat{x})\frac{\partial^2 f(\omega)}{\partial x^2} \end{aligned} \tag{A.29}$$

All the terms on the right side are zero except for the first, because $f(\omega)$ doesn't depend on x. The equation reduces to:

$$i\omega\tau \cdot \chi(\omega, \hat{x}) = \frac{\partial^2 \chi(\omega, \hat{x})}{\partial \hat{x}^2} \tag{A.30}$$

The equation is a linear second-order differential equation, to solve which we assume[1] that $\chi(\hat{x}) \sim e^{\lambda \hat{x}}$. This implies that eq. (A.22) can be written as:

$$\lambda^2 \cdot \chi(\hat{x}) = (i\omega\tau) \cdot \chi(\hat{x}) \tag{A.31}$$

This, in turn, implies that λ must be

$$\lambda = \pm\sqrt{i\omega\tau} \tag{A.32}$$

Since $\sqrt{i}$ is a complex number, we can write it in the form $z \cdot e^{i\theta}$:

$$\sqrt{i} = \sqrt{e^{\frac{\pi}{2}i}} = e^{\frac{\pi}{4}i} = \cos\left(\frac{\pi}{4}\right) + i\sin\left(\frac{\pi}{4}\right) = \frac{1}{\sqrt{2}} + \frac{i}{\sqrt{2}}$$

Thus we have:

$$\lambda = \pm(i+1)\sqrt{\frac{\omega\tau}{2}} \tag{A.33}$$

[1]In order to simplify the writing, for the rest of the paragraph we will express $\chi(\omega, \hat{x})$ as $\chi(\hat{x})$, which can be done since ω is treated as a constant in this calculation.

The general solution to eq. (A.30) is:

$$\chi(\hat{x}) = A \cdot e^{\lambda \hat{x}} + B \cdot e^{-\lambda \hat{x}} \tag{A.34}$$

The boundary conditions that we need to consider are given by physical considerations on the semiconducting layer.

1. Dirichlet boundary condition: the surface potential at the contact point with the electrode must be equal to the applied bias, therefore the response function in $\hat{x} = 0$ must be 1. This is expressed by the condition:

$$v(\omega, 0) = f(\omega) \tag{A.35}$$

2. Neumann boundary condition: no current can flow out of the furthest edge of the layer, so no electric field should exist, and thus

$$\left.\frac{\partial v(\omega, x)}{\partial x}\right|_{x=+\infty} = 0 \tag{A.36}$$

By applying these boundary conditions, we find that the two constants are:

$$A = \frac{e^{\left(-(i+1)\sqrt{\frac{\omega\tau}{2}}\right)}}{2\cos\left((i+1)\sqrt{\frac{\omega\tau}{2}}\right)}$$
$$B = \frac{e^{\left(+(i+1)\sqrt{\frac{\omega\tau}{2}}\right)}}{2\cos\left((i+1)\sqrt{\frac{\omega\tau}{2}}\right)}$$

Finally, the expression for the response function is:

$$\chi(\omega, \hat{x}) = \frac{\cos\left(\frac{1-i}{\sqrt{2}}\sqrt{\omega\tau}(1-\hat{x})\right)}{\cos\left(\frac{1-i}{\sqrt{2}}\sqrt{\omega\tau}\right)} \tag{A.37}$$

When $\omega\tau \gg 1$, it is possible to approximate eq. (A.37) to the following expression.

$$\chi(\omega, \hat{x}) \simeq \exp\left(-(1+i)\sqrt{\frac{\omega\tau}{2}}\ \hat{x}\right) \tag{A.38}$$

Appendix B

Explicit Calculations of the Surface Potential Response to External Biases

The calculation of the samples' surface potential response to an external bias $v(t, x)$ is fundamental for the data analysis. In this chapter, it will be extracted by using the definition of the response function.

$$\tilde{v}(\omega, \hat{x}) = \chi(\omega, \hat{x})\tilde{f}(\omega) \tag{B.1}$$

Since this equation is defined in the frequency domain, the calculations will involve Fourier series and Fourier transforms. For the latter ones, we will adopt the convention:

$$f(t) = \int_{-\infty}^{+\infty} \tilde{f}(\nu)e^{2\pi i\nu t}d\nu$$
$$\tilde{f}(\nu) = \int_{-\infty}^{+\infty} f(t)e^{-2\pi i\nu t}dt$$

or, if we consider the frequency instead of the wave number:

$$f(t) = \frac{1}{2\pi}\int_{-\infty}^{+\infty} \tilde{f}(\omega)e^{i\omega t}d\omega$$
$$\tilde{f}(\omega) = \int_{-\infty}^{+\infty} f(t))e^{-i\omega t}dt$$

B.1 Harmonic bias

Let us consider a harmonic bias in the form

$$f(t) = V_0 \cos(\omega_0 t) \tag{B.2}$$

In order to find $\tilde{f}(\omega)$, we need to execute a Fourier transform on $f(t)$.

$$\tilde{f}(\omega) = \int_{-\infty}^{+\infty} V_0 \cos(\omega_0 t) e^{-i\omega t} dt =$$
$$= \frac{V_0}{2} \int_{-\infty}^{+\infty} (e^{-i(\omega_0 t)} + e^{i(\omega_0 t)}) e^{-i\omega t} dt = \frac{V_0}{2} \int_{-\infty}^{+\infty} \left(e^{-i(\omega-\omega_0)t} + e^{-i(\omega+\omega_0)t}\right) dt =$$
$$= \frac{V_0}{2} (\delta(\omega - \omega_0) + \delta(\omega + \omega_0)) \quad \text{(B.3)}$$

Therefore, eq. (B.1) gives

$$\tilde{v}(\omega, \hat{x}) = \frac{V_0}{2} \cdot \frac{\cos\left(\frac{1-i}{\sqrt{2}}\sqrt{\omega\tau}(1-\hat{x})\right)}{\cos\left(\frac{1-i}{\sqrt{2}}\sqrt{\omega\tau}\right)} (\delta(\omega - \omega_0) + \delta(\omega + \omega_0)) \quad \text{(B.4)}$$

If we define $\hat{t} = \frac{\tau}{t}$ and $\Omega = \omega_0 \tau$, where τ is the time constant characteristic to the device, the inverse Fourier transform yields:

$$v(\hat{t}, \hat{x}) = \frac{V_0}{\cos\left(\sqrt{2\Omega}\right) + \cosh\left(\sqrt{2\Omega}\right)} \cdot$$
$$\cdot \left\{ \cos\left(\Omega \hat{t}\right) \left(\cos\left((\hat{x}-2)\sqrt{\frac{\Omega}{2}}\right) \cosh\left(\hat{x}\sqrt{\frac{\Omega}{2}}\right) + \cos\left(\hat{x}\sqrt{\frac{\Omega}{2}}\right) \cosh\left((\hat{x}-2)\sqrt{\frac{\Omega}{2}}\right) \right) + \right.$$
$$\left. - \sin\left(\Omega \hat{t}\right) \left(\sin\left((\hat{x}-2)\sqrt{\frac{\Omega}{2}}\right) \sinh\left(\hat{x}\sqrt{\frac{\Omega}{2}}\right) + \sin\left(\hat{x}\sqrt{\frac{\Omega}{2}}\right) \sinh\left((\hat{x}-2)\sqrt{\frac{\Omega}{2}}\right) \right) \right\} \quad \text{(B.5)}$$

B.2 Chainsaw Tooth Function, or Triangular Wave

Another bias that can be considered is the chainsaw tooth function, or triangular wave (fig. B.1). If we consider $2T$ as the period of the bias, the fundamental oscillation in $-1 \leqslant \frac{t}{T} \leqslant 1$ is given by:

$$f(t) = V_0 \cdot \left(1 - \frac{2t}{T} \operatorname{sgn}(t)\right) \quad \text{(B.6)}$$

Since this wave has points where it is not differentiable, it is not possible to find an exact Fourier transform for it. Any function, though, can be written using

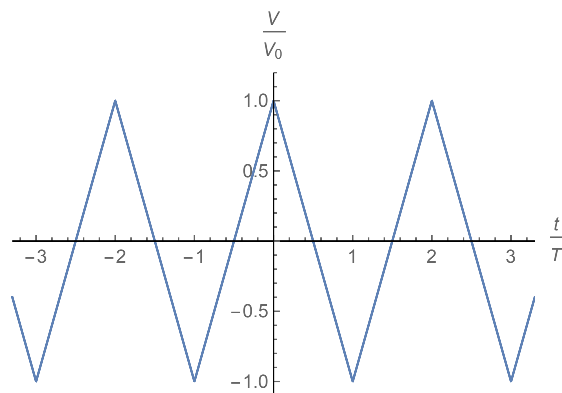

Figure B.1: Normalised chainsaw tooth, or triangular wave, function.

a Fourier series with Fourier coefficients:

$$f(t) = \sum_{n=-\infty}^{\infty} C_n e^{in\omega_0 t}$$
$$C_n = \frac{1}{2T}\int_{-T}^{+T} f(t)e^{-in\omega_0 t}dt$$

where $\omega_0 = \frac{2\pi}{2T} = \pi \cdot T^{-1}$.

In our case, the coefficients are:

$$\begin{aligned}
C_n &= \frac{1}{2T}\int_{-T}^{+T} f(t)(\cos(n\omega_0 t) - i\underbrace{\sin(n\omega_0 t))}_{0}dt = \\
&= \frac{V_0}{2T}\int_{-T}^{+T}\left(1 - \frac{2t}{T}\,\mathrm{sgn}(t)\right)\cos(n\omega_0 t)dt = \\
&= \frac{V_0}{2T}\underbrace{\left[\frac{\sin(n\omega_0 t)}{n\omega_0}\right|_{-T}^{T}}_{0} - \frac{2V_0}{2T}\cdot\frac{2}{T}\int_0^{+T} t\cos(n\omega_0 t)dt = \\
&= -\frac{2V_0}{T^2}\underbrace{\left[t\frac{\sin(n\omega_0 t)}{n\omega_0}\right|_0^{T}}_{0} + \frac{2V_0}{T^2}\int_0^{+T}\frac{\sin(n\omega_0 t)}{n\omega_0}dt = \\
&= \frac{2V_0}{T^2 n^2\omega_0^2}\left[-\cos(n\omega_0 t)\right|_{-T}^{T} = \frac{2V_0}{T^2 n^2\omega_0^2}\left[1 - (-1)^n\right] = \begin{cases} 0, & \text{if } n \text{ is even} \\ \dfrac{4V_0}{T^2 n^2\omega_0^2} & \text{if } n \text{ is odd}\end{cases}
\end{aligned}$$

Therefore, the summation over n is limited to the odd values of n, and the

expression for the bias is:

$$f(t) = \sum_{n=-\infty}^{\infty} \frac{4V_0}{\pi^2(2n-1)^2} e^{i(2n-1)\omega_0 t} \tag{B.7}$$

In order to find the surface potential, we need to find its Fourier series and combine it with eq. (B.1) and the expression for the response (A.37). Therefore, the surface potential oscillations are given by

$$\begin{aligned} v(t,\hat{x}) = \sum_{n=-\infty}^{\infty} \tilde{v}(\omega_n,\hat{x})\ e^{i\omega_n t} = \sum_{n=-\infty}^{\infty} \chi(\omega_n,x)\cdot C_n\ e^{i\omega_n t} = \\ = \sum_{\substack{n=-\infty \\ n \text{ odd}}}^{\infty} \frac{\cos\left(\frac{1-i}{\sqrt{2}}\sqrt{\omega_n\tau}(1-\hat{x})\right)}{\cos\left(\frac{1-i}{\sqrt{2}}\sqrt{\omega_n\tau}\right)} \frac{4V_0}{\pi^2 n^2}\ e^{i\omega_n t} \end{aligned} \tag{B.8}$$

where $\omega_n = n \cdot \omega_0$. By remembering the definition of ω_0, we can rewrite this so as to eliminate the dependence on ω_0.

$$v(t,\hat{x}) = \sum_{\substack{n=-\infty \\ n \text{ odd}}}^{\infty} \frac{4V_0}{\pi^2 n^2} \frac{\cos\left(\frac{1-i}{\sqrt{2}}\sqrt{\frac{n\pi\tau}{T}}(1-\hat{x})\right)}{\cos\left(\frac{1-i}{\sqrt{2}}\sqrt{\frac{n\pi\tau}{T}}\right)}\ e^{i\frac{n\pi}{T}t} \tag{B.9}$$

In order to make the notation easier to read, let's use the following:

$$b_n = \sqrt{\frac{n\pi\tau}{2T}} \tag{B.10}$$

We are now ready to find the response of the device.

$$\begin{aligned} v(t,\hat{x}) &= \sum_{\substack{n=1 \\ n \text{ odd}}}^{\infty} \frac{4V_0}{\pi^2 n^2} \left[e^{i\frac{n\pi}{T}t}\ \frac{\cos((i-1)b_n(1-\hat{x}))}{\cos((i-1)b_n)} + e^{-i\frac{n\pi}{T}t}\ \frac{\cos((1+i)b_n(1-\hat{x}))}{\cos((1+i)b_n)} \right] = \\ &= \sum_{\substack{n=1 \\ n \text{ odd}}}^{\infty} \frac{4V_0}{\pi^2 n^2} \left[e^{i\frac{n\pi}{T}t}\ \frac{e^{i(i-1)b_n(\hat{x}-1)} + e^{-i(i-1)b_n(\hat{x}-1)}}{e^{i(i-1)b_n} + e^{-i(i-1)b_n}} + \right. \\ &\qquad \left. + e^{-i\frac{n\pi}{T}t}\ \frac{e^{i(1+i)b_n(\hat{x}-1)} + e^{-i(1+i)b_n(\hat{x}-1)}}{e^{i(1+i)b_n} + e^{-i(1+i)b_n}} \right] = \end{aligned}$$

$$= \sum_{\substack{n=1 \\ n \text{ odd}}}^{\infty} \frac{4V_0}{\pi^2 n^2} \left(\left(e^{i(1+i)b_n} + e^{-i(1+i)b_n} \right) \left(e^{i(i-1)b_n} + e^{-i(i-1)b_n} \right) \right)^{-1} \cdot$$

$$\cdot \left\{ e^{i\frac{n\pi}{T}t} \left[e^{i(i-1)b_n(\hat{x}-1)} + e^{-i(i-1)b_n(\hat{x}-1)} \right] \left(e^{i(1+i)b_n} + e^{-i(1+i)b_n} \right) + \right.$$

$$\left. + e^{-i\frac{n\pi}{T}t} \left[e^{i(1+i)b_n(\hat{x}-1)} + e^{-i(1+i)b_n(\hat{x}-1)} \right] \left(e^{i(i-1)b_n} + e^{-i(i-1)b_n} \right) \right\} =$$

$$= \sum_{\substack{n=1 \\ n \text{ odd}}}^{\infty} \frac{V_0}{\pi^2 n^2} \frac{1}{\cosh(2b_n) + \cos(2b_n)} \cdot$$

$$\cdot \left\{ e^{i\frac{n\pi}{T}t} \left[e^{-(i+1)b_n\hat{x}+2ib} + e^{-(i+1)b_n\hat{x}+2b} + e^{(i+1)b_n\hat{x}-2b} + e^{(i+1)b_n\hat{x}-2ib} \right] + \right.$$

$$\left. + e^{-i\frac{n\pi}{T}t} \left[e^{(i-1)b_n\hat{x}-2ib} + e^{(i-1)b_n\hat{x}+2b} + e^{-(i-1)b_n\hat{x}-2b} + e^{-(i-1)b_n\hat{x}+2ib} \right] \right\} =$$

$$= \sum_{\substack{n=1 \\ n \text{ odd}}}^{\infty} \frac{V_0}{\pi^2 n^2} \frac{1}{\cosh(2b_n) + \cos(2b_n)} \cdot$$

$$\cdot \left\{ e^{-b_n\hat{x}} \left[e^{ib_n(\hat{x}-2)-i\frac{n\pi}{T}t} + e^{-ib_n(\hat{x}-2)+i\frac{n\pi}{T}t} \right] + e^{-b_n(\hat{x}-2)} \left[e^{ib_n\hat{x}-i\frac{n\pi}{T}t} + e^{-ib_n\hat{x}+i\frac{n\pi}{T}t} \right] + \right.$$

$$\left. + e^{b_n(\hat{x}-2)} \left[e^{-ib_n\hat{x}-i\frac{n\pi}{T}t} + e^{ib_n\hat{x}+i\frac{n\pi}{T}t} \right] + e^{b_n\hat{x}} \left[e^{-ib_n(\hat{x}-2)-i\frac{n\pi}{T}t} + e^{ib_n(\hat{x}-2)+i\frac{n\pi}{T}t} \right] \right\} =$$

$$= \sum_{\substack{n=1 \\ n \text{ odd}}}^{\infty} \frac{2V_0}{\pi^2 n^2} \frac{1}{\cosh(2b_n) + \cos(2b_n)} \cdot$$

$$\cdot \left\{ e^{-b_n\hat{x}} \cos\left(b_n(\hat{x}-2) - \frac{n\pi}{T}t \right) + e^{-b_n(\hat{x}-2)} \cos\left(b_n\hat{x} - \frac{n\pi}{T}t \right) + \right.$$

$$\left. + e^{b_n(\hat{x}-2)} \cos\left(b_n\hat{x} + \frac{n\pi}{T}t \right) + e^{b_n\hat{x}} \cos\left(b_n(\hat{x}-2) + \frac{n\pi}{T}t \right) \right\} =$$

$$= \sum_{\substack{n=1 \\ n \text{ odd}}}^{\infty} \frac{2V_0}{\pi^2 n^2} \frac{1}{\cosh(2b_n) + \cos(2b_n)} \cdot$$

$$\cdot \left\{ e^{-b_n\hat{x}} \cos(b_n(\hat{x}-2)) \cos\left(\frac{n\pi}{T}t \right) + e^{-b_n\hat{x}} \sin(b_n(\hat{x}-2)) \sin\left(\frac{n\pi}{T}t \right) + \right.$$

$$+ e^{-b_n(\hat{x}-2)} \cos(b_n\hat{x}) \cos\left(\frac{n\pi}{T}t \right) + e^{-b_n(\hat{x}-2)} \sin(b_n\hat{x}) \sin\left(\frac{n\pi}{T}t \right) +$$

$$+ e^{b_n(\hat{x}-2)} \cos(b_n\hat{x}) \cos\left(\frac{n\pi}{T}t \right) - e^{b_n(\hat{x}-2)} \sin(b_n\hat{x}) \sin\left(\frac{n\pi}{T}t \right) +$$

$$\left. + e^{b_n\hat{x}} \cos(b_n(\hat{x}-2)) \cos\left(\frac{n\pi}{T}t \right) - e^{b_n\hat{x}} \sin(b_n(\hat{x}-2)) \sin\left(\frac{n\pi}{T}t \right) \right\} =$$

$$= \sum_{\substack{n=1 \\ n \text{ odd}}}^{\infty} \frac{2V_0}{\pi^2 n^2} \frac{1}{\cosh(2b_n) + \cos(2b_n)} \cdot$$

$$\cdot \left\{ \cos\left(\frac{n\pi}{T}t \right) \left[\left(e^{-b_n\hat{x}} + e^{b_n\hat{x}} \right) \cos(b_n(\hat{x}-2)) + \left(e^{b_n(\hat{x}-2)} + e^{-b_n(\hat{x}-2)} \right) \cos(b_n\hat{x}) \right] + \right.$$

$$\left. - \sin\left(\frac{n\pi}{T}t \right) \left[\left(e^{-b_n\hat{x}} - e^{b_n\hat{x}} \right) \sin(b_n(\hat{x}-2)) + \left(e^{b_n(\hat{x}-2)} - e^{-b_n(\hat{x}-2)} \right) \sin(b_n\hat{x}) \right] \right\} =$$

$$= \sum_{\substack{n=1 \\ n \text{ odd}}}^{\infty} \frac{4V_0}{\pi^2 n^2} \frac{1}{\cosh(2b_n) + \cos(2b_n)} \cdot$$
$$\cdot \left\{ \cos\left(\frac{n\pi}{T}t\right) [\cosh(b_n\hat{x})\cos(b_n(\hat{x}-2)) + \cos(b_n\hat{x})\cosh(b_n(\hat{x}-2))] + \right.$$
$$\left. - \sin\left(\frac{n\pi}{T}t\right) [\sinh(b_n\hat{x})\sin(b_n(\hat{x}-2)) + \sin(b_n\hat{x})\sinh(b_n(\hat{x}-2))] \right\}$$

This is the response of the device in the time domain. Writing explicitely b_n and defining $t_0 = \frac{t}{T}$ and $\tau_0 = \frac{\tau}{T}$, this expression becomes:

$$v(t,x) = \sum_{\substack{n=1 \\ n \text{ odd}}}^{\infty} \frac{4V_0}{\pi^2 n^2} \frac{1}{\cosh(\sqrt{2n\pi\tau_0}) + \cos(\sqrt{2n\pi\tau_0})} \cdot$$
$$\cdot \left\{ \cos\left(\frac{n\pi}{T}t\right) \left[\cosh\left(\sqrt{\frac{n\pi\tau_0}{2}}\hat{x}\right) \cos\left(\sqrt{\frac{n\pi\tau_0}{2}}(\hat{x}-2)\right) + \right.\right.$$
$$\left. + \cos\left(\sqrt{\frac{n\pi\tau_0}{2}}\hat{x}\right) \cosh\left(\sqrt{\frac{n\pi\tau_0}{2}}(\hat{x}-2)\right) \right] +$$
$$- \sin\left(\frac{n\pi}{T}t\right) \left[\sinh\left(\sqrt{\frac{n\pi\tau_0}{2}}\hat{x}\right) \sin\left(\sqrt{\frac{n\pi\tau_0}{2}}(\hat{x}-2)\right) + \right.$$
$$\left.\left. + \sin\left(\sqrt{\frac{n\pi\tau_0}{2}}\hat{x}\right) \sinh\left(\sqrt{\frac{n\pi\tau_0}{2}}(\hat{x}-2)\right) \right] \right\} \quad \text{(B.11)}$$

Acknowledgements

In this final pages, I would like to thank some people without whom this thesis would never have been written.

I would like to thank my supervisors, prof. Marco Bazzan and prof. Christian Melzer, for their invaluable scientific advice, support and never-ending patience.

I would also like to thank Karl Philip Strunk and Silke Koser for introducing me to the chemistry lab and training me, helping me take confidence with organic chemistry and device construction.

Thanks go to prof. Uwe Bunz for allowing the use of his laboratory for sample building and of his FET probe station for transistor measurements.

Finally, I wish to thank Ms. Monica Pironi, who is indefatigable and always kind in giving assistance to all the students of the Physics department.

Bibliography

[1] T. Sekitani, U. Zschieschang, H. Klauk, and T. Someya, "Flexible organic transistors and circuits with extreme bending stability," *Nature materials*, vol. 9, no. 12, p. 1015, 2010.

[2] M. Irimia-Vladu, P. A. Troshin, M. Reisinger, L. Shmygleva, Y. Kanbur, G. Schwabegger, M. Bodea, R. Schwödiauer, A. Mumyatov, J. W. Fergus, *et al.*, "Biocompatible and biodegradable materials for organic field-effect transistors," *Advanced Functional Materials*, vol. 20, no. 23, pp. 4069–4076, 2010.

[3] M. Schwoerer and H. C. Wolf, *Organic molecular solids.* John Wiley & Sons, 2007.

[4] A. Köhler and H. Bässler, *Electronic Processes in Organic Semiconductors: An Introduction.* John Wiley & Sons, 2015.

[5] H. Sirringhaus, P. Brown, R. Friend, M. M. Nielsen, *et al.*, "Two-dimensional charge transport in self-organized, high-mobility conjugated polymers," *Nature*, vol. 401, no. 6754, p. 685, 1999.

[6] S. Hellstrom, "Basic models of spin coating," *Submitted as coursework for Physics*, vol. 210, 2007.

[7] A. Tracz, T. Pakula, and J. K. Jeszka, "Zone casting-a universal method of preparing oriented anisotropic layers of organic materials," *Materials Science-Poland*, vol. 22, no. 4, pp. 415–421, 2004.

[8] J. B. Benziger, "Organic vapor phase deposition for optoelectronic devices."

[9] H. Dong, X. Fu, J. Liu, Z. Wang, and W. Hu, "25th Anniversary Article: Key Points for High-Mobility Organic Field-Effect Transistors," *Advanced Materials*, vol. 25, no. 43, pp. 6158–6183, 2013.

[10] I. Kymissis, *Organic Field Effect Transistors: Theory, Fabrication and Characterization.* Springer Science & Business Media, 2008.

[11] C. Tanase, E. Meijer, P. Blom, and D. De Leeuw, "Unification of the hole transport in polymeric field-effect transistors and light-emitting diodes," *Physical Review Letters*, vol. 91, no. 21, p. 216601, 2003.

[12] A. Peled and L. Schein, "Hole mobilities that decrease with increasing electric fields in a molecularly doped polymer," *Chemical physics letters*, vol. 153, no. 5, pp. 422–424, 1988.

[13] V. Kažukauskas, M. Pranaitis, V. Čyras, L. Sicot, and F. Kajzar, "Negative mobility dependence on electric field in poly (3-alkylthiophenes) evidenced by the charge extraction by linearly increasing voltage method," *Thin Solid Films*, vol. 516, no. 24, pp. 8988–8992, 2008.

[14] A. J. Mozer and N. S. Sariciftci, "Negative electric field dependence of charge carrier drift mobility in conjugated, semiconducting polymers," *Chemical physics letters*, vol. 389, no. 4, pp. 438–442, 2004.

[15] M. Koželj and B. Cvikl, "The negative mobility: An outcome of the electric field at the hole-injecting metal/organic semiconductor interface that varies as a linear function of the applied bias," *Thin Solid Films*, vol. 616, pp. 786–792, 2016.

[16] M. Alt, C. Melzer, F. Mathies, K. Deing, G. Hernandez-Sosa, and U. Lemmer, "Adjustable passivation of SiO_2 trap states in OFETs by an ultrathin CVD deposited polymer coating," *Applied Physics A*, vol. 122, no. 3, pp. 1–7, 2016.

[17] O. Boughias, M.-S. Belkaid, F. Nemmar, and D. Hatem, "Organic transistors field effect performances," *International Journal of Research and Reviews in Applied Sciences*, vol. 12, no. 2, 2012.

[18] M. Irimia-Vladu, P. A. Troshin, M. Reisinger, L. Shmygleva, Y. Kanbur, G. Schwabegger, M. Bodea, R. Schwödiauer, A. Mumyatov, J. W. Fergus, *et al.*, "Biocompatible and biodegradable materials for organic field-effect transistors," *Advanced Functional Materials*, vol. 20, no. 23, pp. 4069–4076, 2010.

[19] L. Kelvin, "V. contact electricity of metals," *The London, Edinburgh, and Dublin Philosophical Magazine and Journal of Science*, vol. 46, no. 278, pp. 82–120, 1898.

[20] I. Jankov, I. Goldman, and R. Szente, "Principles of the kelvin probe force microscopy," *Revista Brasileira de Ensino de Física*, vol. 22, no. 4, p. 503, 2000.

[21] W. Melitz, J. Shen, A. C. Kummel, and S. Lee, "Kelvin probe force microscopy and its application," *Surface Science Reports*, vol. 66, no. 1, pp. 1–27, 2011.

[22] O. Tal, Y. Rosenwaks, Y. Preezant, N. Tessler, C. Chan, and A. Kahn, "Direct determination of the hole density of states in undoped and doped amorphous organic films with high lateral resolution," *Physical review letters*, vol. 95, no. 25, p. 256405, 2005.

[23] K. Celebi, P. Jadhav, K. Milaninia, M. Bora, and M. Baldo, "The density of states in thin film copper phthalocyanine measured by kelvin probe force microscopy," *Applied Physics Letters*, vol. 93, no. 8, p. 317, 2008.

[24] X. Li, A. Kadashchuk, I. I. Fishchuk, W. T. Smaal, G. Gelinck, D. J. Broer, J. Genoe, P. Heremans, and H. Bässler, "Electric field confinement effect on charge transport in organic field-effect transistors," *Physical review letters*, vol. 108, no. 6, p. 066601, 2012.

[25] T. Hallam, M. Lee, N. Zhao, I. Nandhakumar, M. Kemerink, M. Heeney, I. McCulloch, and H. Sirringhaus, "Local charge trapping in conjugated polymers resolved by scanning kelvin probe microscopy," *Physical review letters*, vol. 103, no. 25, p. 256803, 2009.

[26] C. Melzer, C. Siol, and H. von Seggern, "Transit phenomena in organic field-effect transistors through Kelvin-Probe Force Microscopy," *Advanced Materials*, vol. 25, no. 31, pp. 4315–4319, 2013.

[27] C. Siol, C. Melzer, and H. von Seggern, "Electron trapping in pentacene based p-and n-type organic field-effect transistors," *Applied Physics Letters*, vol. 93, no. 13, p. 133303, 2008.

[28] J. Burns, "Large-signal transit-time effects in the MOS transistor," *RCA REVIEW*, vol. 30, pp. 15–35, 1969.

[29] Z. Chiguvare, J. Parisi, and V. Dyakonov, "Influence of thermal annealing on the electrical properties of poly (3-hexylthiophene)-based thin film diodes," *Zeitschrift für Naturforschung A*, vol. 62, no. 10-11, pp. 609–619, 2007.

[30] L. A. Kehrer, S. Winter, R. Fischer, C. Melzer, and H. von Seggern, "Temporal and thermal properties of optically induced instabilities in P3HT field-effect transistors," *Synthetic Metals*, vol. 161, no. 23, pp. 2558–2561, 2012.

[31] ParaTech, "Parylene properties chart."

[32] M. Pietsch, "Bachelor thesis." University of Heidelberg, 2015.

[33] G. Metzger, *Transmission lines with pulse excitation.* Elsevier, 2012.